ENHANCED TARGET DISCRIMINATION AND DELAY-DOPPLER RESOLUTION IN CHIRP RADAR SYSTEMS

A Dissertation

Submitted to the Faculty

of

Purdue University

by

Chia-Jung Chang

In Partial Fulfillment of the

Requirements for the Degree

of

Doctor of Philosophy

August 2020

Purdue University

West Lafayette, Indiana

THE PURDUE UNIVERSITY GRADUATE SCHOOL
STATEMENT OF DISSERTATION APPROVAL

Prof. Mark R. Bell, Chair
School of Electrical and Computer Engineering

Prof. Michael D. Zoltowski
School of Electrical and Computer Engineering

Prof. James V. Krogmeier
School of Electrical and Computer Engineering

Prof. James S. Lehnert
School of Electrical and Computer Engineering

Approved by:

Prof. Dimitri Peroulis
Head of the School Graduate Program

ACKNOWLEDGMENTS

First of all, I would like to express my endless gratitude to Professor Bell, my major advisor, for supporting me to pursue the knowledge on my road toward the PhD degree. No matter what difficulties and problems I met, Professor Bell always accompanied with me and provided useful suggestions to help me get through these difficulties. I truly appreciate Professor Bell's assistance.

Second, I would like to thank to my committee members, Professor Krogmeier, Professor Zoltowski and Professor Lehnert, for their insightful suggestions and distinguished perspectives, which were quite helpful for me in my research work.

I also would like to show my appreciation to my good friends, Wei-Kang, David Zilz, I-Fan, Steve Rausch, Yu-Hsiang, Chin-Ning and Wan-Elh. They gave me a variety of assistance and encouragement in my daily life, making my life much more colorful and wonderful.

Finally, I am really thankful to my parents and my family. They always tell me not to think too much and focus on pursuing my goal and fulfilling my dream. Because of you, I can do my best and move forward to my goal without any worries. Thank you so much!

TABLE OF CONTENTS

Page

Page

LIST OF TABLES

LIST OF FIGURES

Figure Page

Figure Page

Figure Page

Figure Page

Figure Page

ABSTRACT

Chang, Chia-Jung Ph.D., Purdue University, August 2020. Enhanced Target Discrimination and Delay-Doppler Resolution in Chirp Radar Systems. Major Professor: Mark R. Bell.

Target detection, estimation, and discrimination have long been important research issues in the field of radar. Waveform design, analog signal processing, and digital signal processing are some techniques that can improve the detection, estimation, and discrimination ability. In this dissertation, we first address the sidelobe suppression from the waveform design point of view. We synthesize a non-constant modulus waveform for illumination of radar targets by applying a collection of constant modulus (linear frequency modulated (LFM) waveforms with different frequency offsets) waveforms from each transmitting array element in an antenna array, and we show from the ambiguity function that the non-constant modulus waveform has better performance with respect to the larger ambiguity function mainlobe-to-peak-sidelobe ratio than this ratio of a constant modulus (LFM-only) waveform. Furthermore, from the angular resolution point of view, the synthesized non-constant modulus waveform also has better performance than the angular resolution of a constant modulus waveform at the expense of the decrease in the signal energy on targets.

Secondly, we investigate radar delay-Doppler resolution enhancement from the digital signal processing viewpoint. We introduce the noise-target fringe analysis technique and combine it with the coherent CLEAN algorithm to provide accurate target parameter estimates in terms of delay, Doppler shift and intensity. Furthermore, the accuracy of target parameter estimates can be further improved by applying weighted non-linear least squares estimation.

Finally, we further aim for the improvement in radar delay-Doppler resolution. Instead of using the matched filter only, we propose a hybrid filter which combines a chirp matched filter and chirp mismatched filters. The hybrid filter output response shows much better performance in delay and Doppler resolution compared to the chirp matched filter output response. Thus, this hybrid filter design has better target identification capability than the original chirp matched filter. Furthermore, from a real implementation perspective, there is no need to significantly increase the hardware and software complexity of the radar, since we only need to mismatch the received waveform to another chirp waveform and perform some additional non-linear processing. Then a chirp radar system with high delay-Doppler resolution and accurate target discrimination ability can be easily achieved.

1. INTRODUCTION

Radar target discrimination—the ability to discern multiple target returns—has been one of the most important issues in radar research for a long time. It determines not only the ability of detecting multiple targets with close ranges and Doppler shifts, but also the estimation accuracy of targets' delays and Doppler shifts. Some performance metrics such as the mainlobe to the peak sidelobe ratio (PSLR) of a target's delay-Doppler response, the delay-Doppler resolutions, and mutual interference level among the reflected targets, are key performance indicators in radar systems. Hence, the peak sidelobe ratio (PSLR) enhancement, much finer delay-Doppler resolutions, and interference suppression are the main goals to achieve better target discrimination ability.

However, when pursuing these performance metrics, some practical constraints may limit the radar system designs, such as the size of the antenna, the permitted signal bandwidth, the maximum power of waveform transmission, the digital signal processing capability, and the radar system complexity. Because of these limits, the performance of the overall radar design can be significantly affected.

In traditional pulse radar systems, an unmodulated waveform is transmitted, and a matched filter is applied at the receiver to collect the scattered signal and extract the reflected targets' information such as the presence, positions, velocities and intensities. However, the matched filter output response in the delay domain, which is determined by the time-autocorrelation of the waveform, is a triangular shape in amplitude, which may cause problems in discriminating two spatially close targets, especially when one of the target returns has a much smaller amplitude than the amplitude of the other return. Also, unmodulated pulse radar systems are prone to jamming or interference from other radar systems, causing performance degradation in target detection and estimation.

To solve the poor range resolution and jamming problems in unmodulated pulse radar systems, modulated waveforms are often applied in radar systems. Modulated waveforms include amplitude modulations, frequency modulations, phase modulations, and the mixture of these modulation techniques. The main advantage of applying modulated waveforms is that these waveforms can be compressed and then possesses a much sharper matched filter delay output response. This property improves the radar's range resolution and discrimination ability.

However, even if finer range resolution can be achieved, for an amplitude modulated waveform, the amplitude of the transmitted pulse varies with time, which may cause power efficiency problems. The reason for this is that radar transmitters usually employ efficient, saturated, nonlinear power amplifiers for energy efficient operation, as the total power transmitted by most radar systems is large, so power efficiency is important. Because of this concern, constant modulus waveforms are commonly adopted for transmission in most of the modern radar systems.

Frequency modulated waveforms, phase modulated waveforms, and the mixture of frequency-phase modulated waveforms belong to the class of constant modulus waveforms, i.e., the pulse amplitude is constant in the whole duration of transmission [1–7]. The constant modulus property allows radar transmitters to have greater power efficiency. Linear "Chirp" radars, radars using a linear frequency modulated (LFM) waveform for transmission, are one of the most popular and widely used types of radar systems [1, 8–10]. Due to the both advantages of range compression and constant waveform modulus, finer range resolution and the better power efficiency can be achieved by using a linear chirp waveform. Thus, in this dissertation, we mainly focus on applying linear frequency modulated waveforms (LFM) to improve the peak sidelobe ratio (PSLR) of a target's delay-Doppler response, improve the delay-Doppler resolution, and suppress interference among all targets.

To improve the peak sidelobe ratio (PSLR) of a target's matched filter delay-Doppler response, we apply some waveform design techniques. Waveform diversity (WD), one of the novel waveform design techniques, is a popular research topic in

recent years [11–16], and the specific explanation of waveform diversity can be found from the IEEE Standard 686-2008 definition [17]. In general, waveform diversity is used to optimize the overall radar system performance in terms of some performance metrics in certain specific scenarios. Recently, diversity waveform research for phased array radars and MIMO radars is popular [18–21]. Furthermore, for chirp radars, chirp diversity has also been extensively discussed [22–24]. By optimizing the chirp waveforms, the performance in terms of the delay-Doppler resolution, the angular resolution or the sidelobe suppression can be further improved.

However, the optimized radar waveform, which achieves some of the best performance metrics, sometimes may not be easily synthesized. From the ambiguity function point of view, we know that a thumbtack shape in the ambiguity function for a waveform can achieve the best delay-Doppler resolution, but so far, the waveform having this ambiguity function can not be easily generated. Such a near optimal waveform cannot be easily implemented in real radar systems because of limitations and constraints in these radar systems.

Therefore, to meet the requirement of easy and practical implementations, we select chirp radars as our system structure. We apply a linear array of transmit elements as the transmitters, and all elements transmit constant modulus waveforms, but with different frequency offsets. We then design a non-constant modulus synthesized waveform by summing these different constant-modulus waveforms, and then apply matched filtering to the synthesized non-constant modulus waveform to improve the delay-Doppler resolution. Note that Maxwell's equations, being linear, result in the waveform illuminating the target being the sum of phase shifted versions of each of the constant modulus waveforms transmitted by each of the array elements. Also, the angular resolution analysis of the non-constant modulus synthesized waveform is provided, and it has a slight improvement in angular resolution compared to the constant-modulus waveform.

Furthermore, concerning of the delay-Doppler resolutions enhancement issue, it is known that the matched filter output response of a linear chirp pulse has a triangular

envelope along the α-rotated axis ($\nu = \alpha\tau$) in the delay-Doppler plane, where α is the chirp rate of the chirp pulse. When any pair of targets are close enough in delay and Doppler shift, and they have a Doppler shift difference which equals to their delay difference multiplied by the chirp rate of the transmitted chirp waveform α, the traditional chirp matched filter output response will have a mixed envelope made up of two partially overlapping triangular envelopes. Furthermore, when one of the two target returns is smaller than the other, the smaller triangular envelope may be masked in the mixed envelope, causing a missed detection of the smaller target.

To solve the poor ridge resolution problem in chirp radars, we introduce a new image processing technique, *noise-target fringe analysis*, that can effectively estimate targets' delay information. We also combine the concept of the coherent CLEAN algorithm [25–28] with the noise-target fringe analysis to further estimate the Doppler shifts and amplitudes of the targets. This target parameter estimation method has high accuracy in target parameter estimation and then improves the ability of target differentiation along the chirp ridges. To achieve more precise estimates, we can further apply the Gauss-Newton optimization method to find a weighted nonlinear least squares estimate of the target parameters, which can further improve the radar's target discrimination ability.

Likewise, interference suppression is also a significant radar issue. Based on the chirp transmitter-receiver structure, we design a hybrid filter, which is combined with the original chirp matched filter and a chirp mismatched filter, to effectively suppress the triangular amplitude along the chirp ridge in the chirp matched filter output response. This is quite useful for resolving two close targets which lie the line with the slope α, the chirp rate of the transmitted chirp waveform, in the delay-Doppler response. Therefore, by applying this hybrid filter, the resolution along the chirp ridge as well as the range resolution can be greatly improved.

1.1 Review of the Matched Filter and Radar Ambiguity Function

In this section, we give a brief introduction to the matched filter and the ambiguity function. In the followings of the dissertation, we will take advantage of these concepts to discuss the output response of the matched filter and the mismatched filter. Also, the relationship between the ambiguity function and the delay-Doppler response will be presented.

1.1.1 The Matched Filter

To measure the delay of a target return in a radar system, we usually apply the matched filter. Due to the property that the maximum signal-to-noise ratio (SNR) is achieved when the received waveform and the delayed version of the transmitted waveform are perfectly matched, we can then extract the return signal's delay information under the condition of the maximum SNR. Therefore, the matched filter design is widely used in the radar receivers [8, 9, 29, 30].

When the received waveform is fed into the matched filter, a delayed, conjugated and time-reversed version of the matching template waveform is convolved with the received waveform to generate the filter output response. When the two waveforms are perfectly matched, the peak of the output response occurs, which also means the maximum energy output is achieved. We can then use the time difference between the instant of the beginning of waveform transmission and instant of the occurrence of the peak amplitude in the output response, as well as the pulse width of the transmitted waveform to calculate the target's range.

We know from the matched filter that the peak amplitude of the output response happens when the received waveform and matching template waveform are perfectly matched. We can then use the time difference between the transmission time and the peak matched filter output time to determine the distance between the transmitter and the target. However, when the amplitude of the signal output response which is close to the peak drops off too slowly, it may cause the accuracy problems in measuring

the target's distance due to the contribution of noise in the output response. The total matched filter output response is constituted of the signal output response and the noise output response. When the signal output response does not fall of quickly around the peak, because of the randomness of the amplitude of the noise output response, it may change the time of the occurrence of the peak of the total output response, causing an error in the measurement of the target's distance.

Furthermore, when the received waveform contains two targets which lie close together in range but with a great difference in the amplitude, then the output response of the target with the larger amplitude has almost the same amplitude around the peak, which is much larger than the peak of the output response of the target with the smaller amplitude. Therefore, the peak of the target with the smaller amplitude is concealed in the output response of the target with the larger amplitude, causing a single peak only which is shown at the total output response; then the smaller target may not be detected. This will cause a problem in resolving the two targets.

Therefore, how to design a transmitted waveform as well as a matching template waveform to make delay response of the filter approach the thumbtack shape and improve the accuracy and the delay-Doppler resolution problem has long been an interesting research issue.

From the concept of the matched filter we know that the maximum attainable signal energy is achieved when the filter impulse response is perfectly match to the reflected signal in time. However, when the reflected signal is from a moving target, the reflected signal is Doppler affected, causing a shift in the carrier frequency [10]. In addition, the receiver does not have any knowledge about the Doppler shift when receiving the reflected signal, so a mismatch in Doppler happens when performing the above mentioned matched filtering process. Such kind of mismatch in delay and Doppler of the matched filter output is related to the *Ambiguity Function* of the transmitted waveform. In the following, we briefly introduce the definition and some important properties of the ambiguity function, as the ambiguity function will be widely used throughout this dissertation.

1.1.2 The Radar Ambiguity Function

The ambiguity function is the time response of a mismatched filter to the transmitted signal when there is a delay mismatch of τ and a Doppler shift mismatch of ν [10, 31–34]. In this subsection, we first provide the definition of the narrowband radar ambiguity function (AF), and then we present some important properties of the ambiguity function [10,35]. The ambiguity function fully shows the targets' delay and Doppler characteristics, and it is helpful in the design of high-resolution waveforms in matched-filter radar systems.

Definition

Let $s(t)$ be a finite energy, baseband transmitted waveform with the complex envelope, where

$$\int_{-\infty}^{\infty} |s(t)|^2 dt = E_s,$$

then the (symmetric) ambiguity function of $s(t)$ is defined as

$$\Gamma(\tau, \nu) = \int_{-\infty}^{\infty} s(t + \tau/2) s^*(t - \tau/2) e^{-i2\pi\nu t} dt. \tag{1.1}$$

Alternatively, the (asymmetric) ambiguity function of $s(t)$ is defined as

$$\chi(\tau, \nu) = \int_{-\infty}^{\infty} s(t) s^*(t - \tau) e^{-i2\pi\nu t} dt. \tag{1.2}$$

In this dissertation, we primarily use the asymmetric ambiguity function $\chi(\tau, \nu)$ and regard it as the main function for delay-Doppler analysis.

Now, with the definition of the ambiguity function, there are four important properties of the ambiguity function [32, 33],

Property 1:

$$|\chi(\tau, \nu)| \leq |\chi(0, 0)| = E_s. \tag{1.3}$$

Property 2:

$$\int_{-\infty}^{\infty} \int_{-\infty}^{\infty} |\chi(\tau, \nu)|^2 d\tau d\nu = E_s^2. \tag{1.4}$$

Property 3:

$$|\chi(-\tau,-\nu)| = |\chi(\tau,\nu)|. \tag{1.5}$$

Property 4:

If a given complex envelope transmitted signal $s(t)$ has an ambiguity function $\chi(\tau,\nu)$, then $s(t)\cdot e^{i\pi kt^2}$ has the ambiguity function $e^{-i\pi k\tau^2}\cdot\chi(\tau,\nu-k\tau)$.

With these four important properties of the ambiguity function, we will provide two examples which show the ambiguity functions of the unmodulated rectangular pulse and the linear frequency modulated (LFM) pulse. In the rest of the dissertation, we sometimes use name "linear chirp pulse" interchangeably with "LFM pulse".

Ambiguity Function of an Unmodulated Rectangular Pulse

Let $s_{\text{rect}}(t)$ be an unmodulated constant-modulus pulse of length T as follows:

$$s_{\text{rect}}(t) = 1_{[0,T]}(t). \tag{1.6}$$

Then, from (1.2) we know that the ambiguity function of $s_{\text{rect}}(t)$ is

$$\begin{aligned}\chi_{\text{rect}}(\tau,\nu) &= \int_{-\infty}^{\infty} s_{\text{rect}}(t)s_{\text{rect}}^*(t-\tau)e^{-i2\pi\nu t}dt \\ &= \int_{-\infty}^{\infty} 1_{[0,T]}(t)\cdot 1_{[0,T]}(t-\tau)e^{-i2\pi\nu t}dt \\ &= e^{-i\pi\nu(T+\tau)}(T-|\tau|)\,\text{sinc}\left(\nu(T-|\tau|)\right),\ 0\le|\tau|\le T. \end{aligned}\tag{1.7}$$

The ambiguity surface $|\chi_{\text{rect}}(\tau,\nu)|$, the zero-delay cut $|\chi_{\text{rect}}(0,\nu)|$, and the zero-Doppler cut $|\chi_{\text{rect}}(\tau,0)|$ are shown in Figures 1.1, 1.2 and 1.3.

Ambiguity Function of a Linear Frequency Modulated Pulse

Let $s_{\text{chirp}}(t)$ be a linear frequency modulated constant-modulus pulse of length T as follows:

$$s_{\text{chirp}}(t) = e^{i\pi\alpha t^2}1_{[0,T]}(t), \tag{1.8}$$

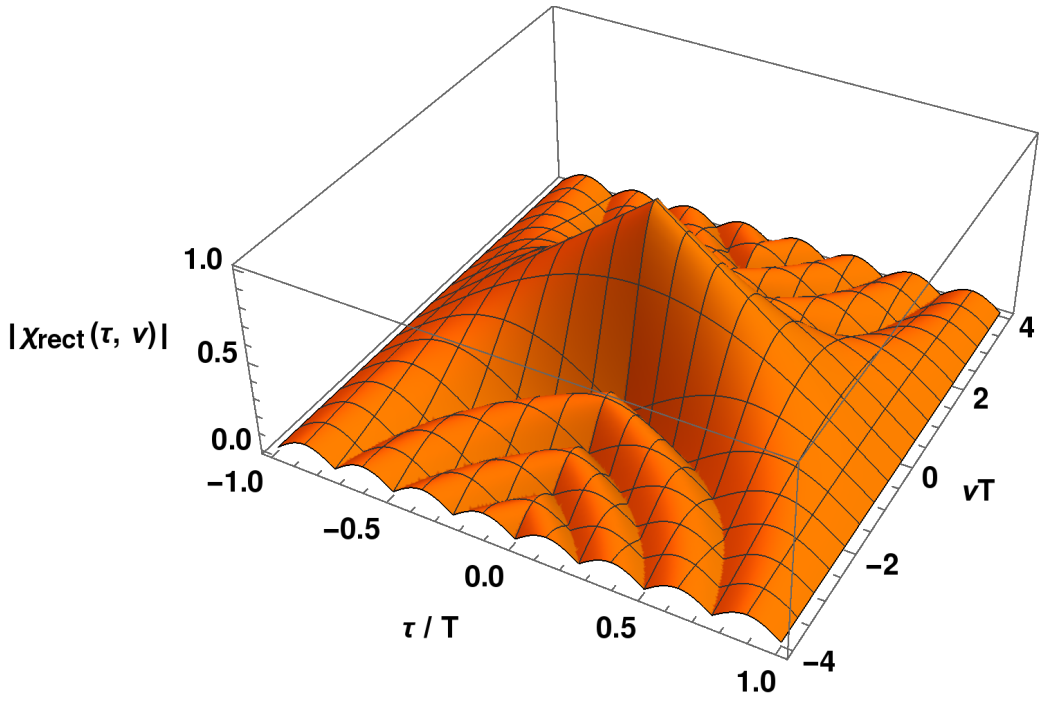

Fig. 1.1. Ambiguity function of an unmodulated rectangular pulse of length T.

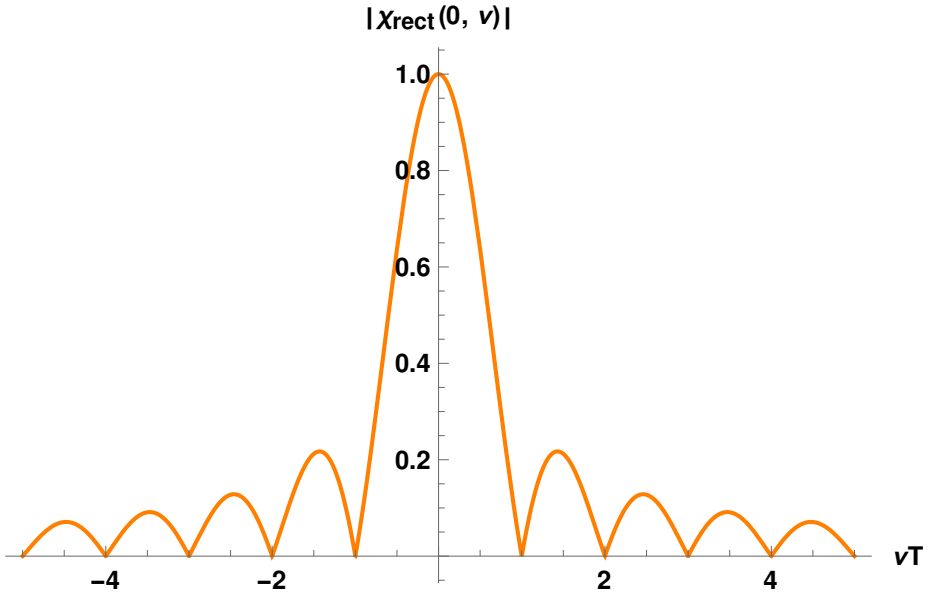

Fig. 1.2. Zero-delay cut of an unmodulated rectangular pulse of length T.

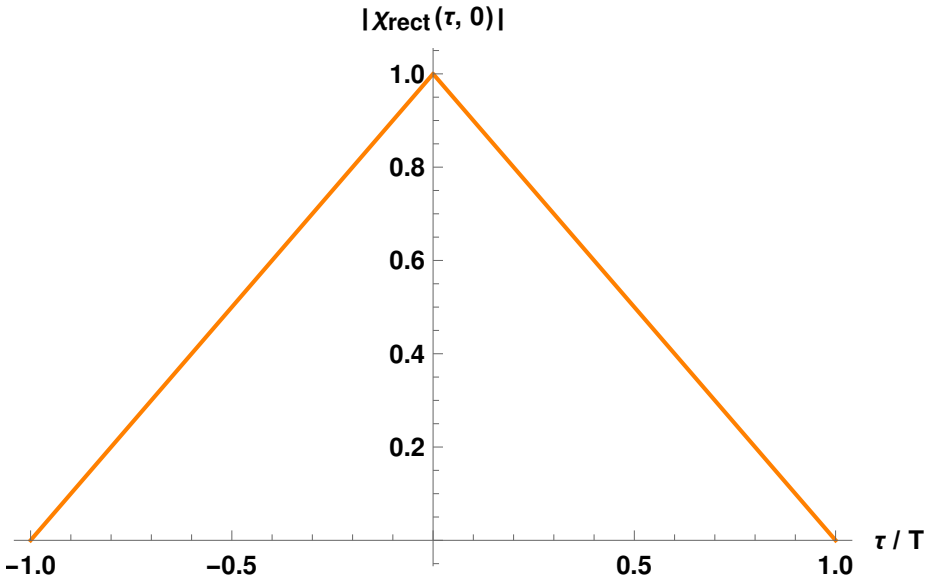

Fig. 1.3. Zero-Doppler cut of an unmodulated rectangular pulse of length T.

where αt is the instantaneous frequency of the signal $s_{\text{chirp}}(t)$. So we know that when α is fixed, the instantaneous frequency of $s_{\text{chirp}}(t)$ linearly changes with time. As a result, the pulse $s_{\text{chirp}}(t)$ is also called a linear "chirp" pulse. Here, α is the rate of linear increase (decrease) in frequency of the signal, and it is also called "chirp rate".

When using the above $s_{\text{chirp}}(t)$ as the transmitted waveform, from (1.2) we know that the ambiguity function of $s_{\text{chirp}}(t)$ becomes

$$\begin{aligned}\chi_{\text{chirp}}(\tau,\nu) &= \int_{-\infty}^{\infty} s_{\text{chirp}}(t)s^*_{\text{chirp}}(t-\tau)e^{-i2\pi\nu t}dt \\ &= \int_{-\infty}^{\infty} e^{i\pi\alpha t^2}1_{[0,T]}(t)\cdot e^{-i\pi\alpha(t-\tau)^2}1_{[0,T]}(t-\tau)e^{-i2\pi\nu t}dt \\ &= e^{-i\pi\tau\nu}e^{-i\pi(\nu-\alpha\tau)T}(T-|\tau|)\,\text{sinc}((\nu-\alpha\tau)(T-|\tau|)),\ 0\le|\tau|\le T. \quad (1.9)\end{aligned}$$

The ambiguity surface $|\chi_{\text{chirp}}(\tau,\nu)|$, the zero-delay cut $|\chi_{\text{chirp}}(0,\nu)|$, and the zero-Doppler cut $|\chi_{\text{chirp}}(\tau,0)|$ are shown in Figures 1.4, 1.5 and 1.6.

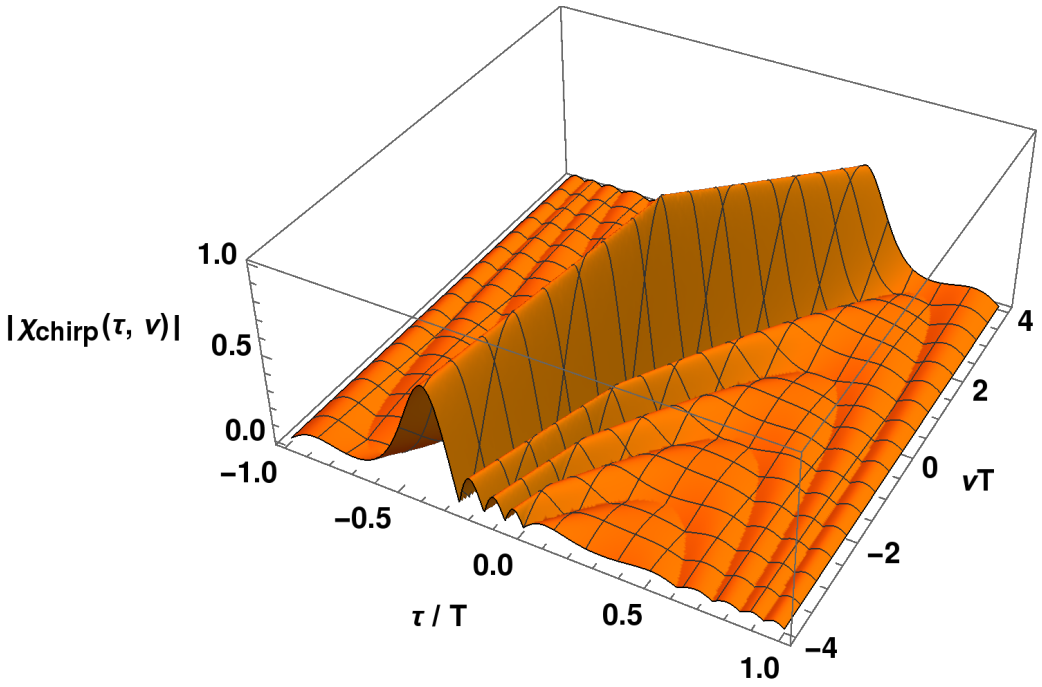

Fig. 1.4. Ambiguity function of a chirp pulse of length T.

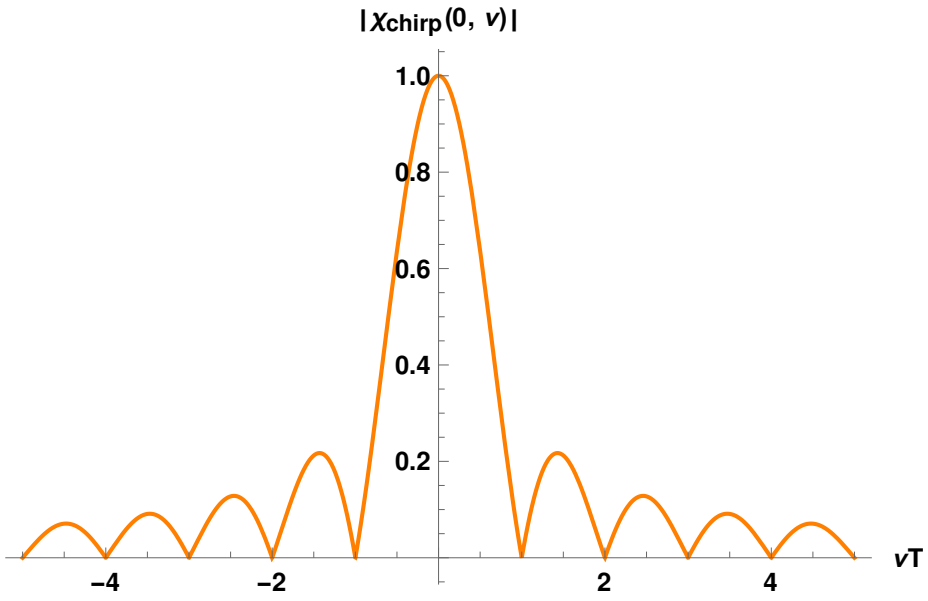

Fig. 1.5. Zero-delay cut of a chirp pulse of length T.

1.2 Dissertation Outline

In this dissertation, we deal with the target discrimination issue from three different aspects: the sidelobe suppression by the chirp diversity, the delay-Doppler

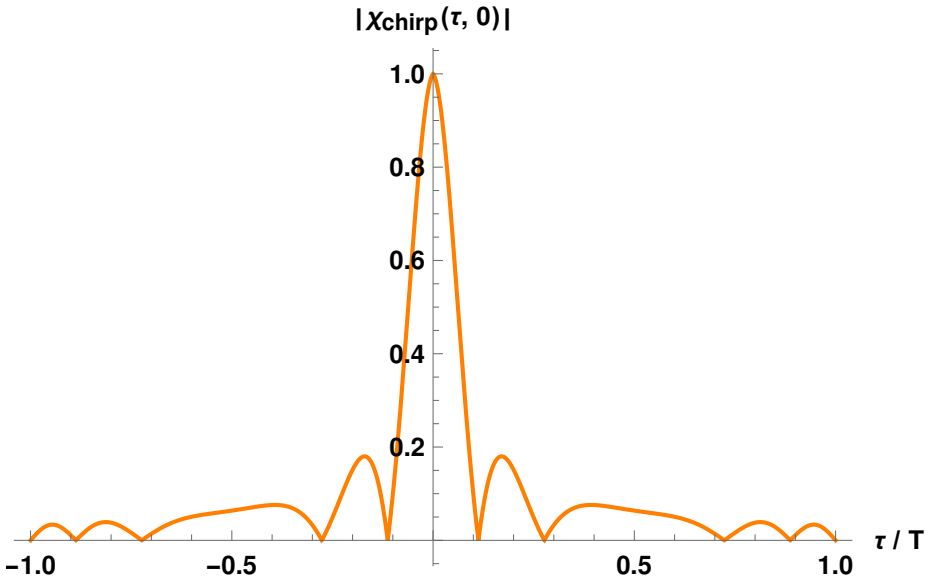

Fig. 1.6. Zero-Doppler cut of a chirp pulse of length T.

resolution (especially the ridge resolution) enhancement by the noise-target fringe analysis approach, and the interference suppression by the chirp hybrid filter system. The following is an outline of the dissertation:

In Chapter 2, we use the line array structure for waveform transmission, and we design the frequency modulated constant modulus waveform in each transmitted element to synthesize a non-constant modulus waveform at the target which is then reflected back to the receiver. Therefore, the receiver can receive a "non-constant modulus equivalent" waveform constituted by the sum of the constant-modulus waveform from all the transmitted elements. After processing with the matched filter, better delay-Doppler resolution and the better angular resolution can be achieved.

In Chapter 3, we deal with the chirp waveform by analyzing the phase response (along the chirp rate-rotated axis) of the matched filter output. By applying the noise-target fringe analysis combined with the CLEAN algorithm, target parameters in terms of delays, Doppler shifts and amplitudes can be effectively estimated. Furthermore, to achieve more accurate target parameter estimations, we can fur-

ther apply the weighted non-linear least squares estimates, then the ability of target discrimination can be further enhanced.

In Chapter 4, we apply the chirp waveform as the transmitted waveform, and in the receiver, we design a hybrid filter which is composed of a matched filter and a mismatched filter to suppress the ridge effect in the chirp delay-Doppler response and then to enhance the delay-Doppler resolution. This is quite useful when any two close targets lying in the line with slope α, the chirp rate of the transmitted chirp waveform, in the delay-Doppler plane, and the target discrimination ability can be significantly improved. In addition, the mismatched filter can be easily implemented without further hardware deployments. Therefore, this chirp hybrid filter design may be quite useful in enhancing the delay-Doppler resolution.

Finally, in Chapter 5, we summarize our research results and provide the conclusions.

2. DELAY-DOPPLER RESOLUTION CHARACTERISTICS OF CONSTANT MODULUS WAVEFORM MIMO RADAR

2.1 Introduction

Most modern radar systems transmit constant modulus (amplitude) waveforms. The reason for this is that radar transmitters usually employ efficient saturated nonlinear power amplifiers for energy efficient operation, as the total power transmitted by most radar systems is large, so power efficiency is important. One implication of this is that the resulting waveforms illuminating radar targets are constant modulus waveforms. This is true both for standard radar antennas and phased array radar systems where identical (or phase shifted) versions of the same waveform are transmitted out of each antenna element [36, 37]. Because of this fact, most matched-filter radar systems have delay-Doppler resolution dictated by the ambiguity function of constant modulus waveforms.

One consequence of this is that in selecting a waveform with prescribed delay-Doppler resolution characteristics, we are limited to considering only the ambiguity functions of constant modulus waveforms in our search for a radar signal. So the following question immediately arises: *if we could transmit a non-constant modulus waveform, would it be possible to find a waveform with a superior ambiguity function characteristic if we did not limit ourselves to constant modulus waveforms?* The answer to this question is probably "yes", since we would be searching over a larger set of waveforms. However, how much better a waveform we can find in this larger class is not clear, so answering this question would allow us to determine if there is even any significant value in illuminating targets with a non-constant modulus waveform as compared to a constant modulus waveform.

Even if there is an advantage to illuminating targets with a non-constant modulus waveform, it may appear that there is little reason to consider these advantages if we are forced to use constant-modulus waveforms because of power amplifier constraints. However, if we transmit *different* constant-modulus waveforms from the elements of a transmit antenna array, the resulting waveforms illuminating a target in space will in general be non-constant modulus and hence could in principle have a superior ambiguity function compared to those corresponding to a constant modulus waveform [11, 12, 16, 24, 38].

Because Maxwell's equations are linear, the illuminating waveform at a point in space will be a linear combination of phase-shifted version of the constant modulus waveforms transmitted by each of the antenna elements. So in order to answer the question of whether we can get more useful delay-Doppler responses from a collection of different constant-modulus waveforms transmitted from different elements of a transmitter array, we must determine whether or not it is possible to find a sum of constant modulus waveforms that has a better ambiguity function—in some sense—than any single constant modulus waveform. As we will see, this is in fact the case.

Given that we can find a set of constant modulus waveforms whose sum has a better ambiguity function than any single constant modulus waveform, the next question of interest is, how does the synthesized illumination on target change with respect to changes in the angle of interest with respect to the array [39]. For example, if we design a set of constant modulus waveforms so that the sum of these waveforms yields a particular waveform in the far field off boresight (at an angle of 0 degrees), at other angles, the resulting waveforms will be different than at boresight. In fact, each direction in the far field will have a different waveform because of the change in phase shifts in the constant modulus component from each array element as the direction changes. This phenomena, which has been called *space-time landscaping*, provides directional information about received returns [40]. In light of this, three important questions come to mind: First, does this change in illumination wave-

form with direction yield additional angular resolution over a standard phased array radar? Second, if a good illuminating waveform is achieved in a particular direction (e.g., boresight), will the resulting waveforms in other directions have good ambiguity functions? Third, how significant is the mutual interference of returns from directions having different synthesized waveforms than that for the intended design direction? Answers to these questions are important if we are to exploit this waveform synthesis approach in an actual radar system.

2.2 Mathematical Model for The Synthesis of Non-Constant Modulus Waveforms

In an antenna array system, a waveform on target in the far field synthesized by $2K+1$ waveforms out of each transmitted array element is shown in Figure 2.1, and the waveform can be expressed in the following general form:

$$s(t) = \sum_{m=-K}^{K} s_m(t). \tag{2.1}$$

Then the ambiguity function of a synthesized narrowband waveform $s(t)$ is

$$\chi_s(\tau, \nu) = \int_{\mathbb{R}} s(t)s^*(t-\tau)e^{-i2\pi\nu t}dt. \tag{2.2}$$

In the following we will apply two cases to show the difference in terms of the amplitude of synthesized waveforms. In addition, we will also use the same two cases to show the differences in delay-Doppler characteristics between constant modulus waveforms and non-constant modulus waveforms.

2.2.1 Case 1: Waveform Synthesized by Identical Rectangular Pulses vs. Waveform Synthesized by Rectangular Pulses with Different Frequency Offsets

In this case, we consider about the difference between a constant modulus waveform synthesized by $2K+1$ identical rectangular pulses and a non-constant modulus

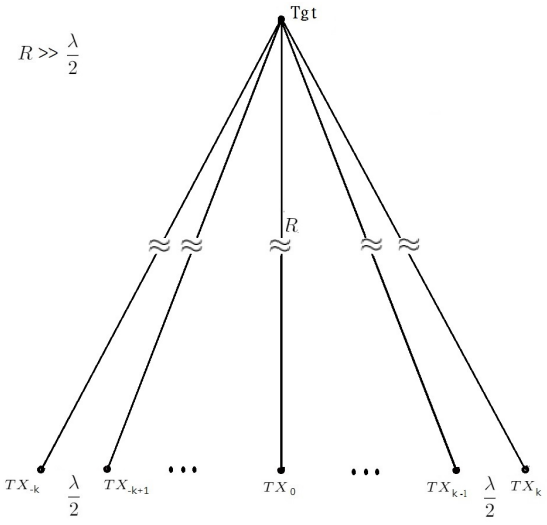

Fig. 2.1. Transmitted antenna array structure.

waveform synthesized by $2K+1$ rectangular pulses with $2K+1$ different frequency offsets. For the constant modulus synthesized waveform, each transmitted waveform is

$$s_m(t) = 1_{[0,T]}(t), \tag{2.3}$$

where T is the pulse duration. So $s_m(t) = 0,\ \forall t \notin [0,T]$. The amplitude of the synthesized waveform is shown in Figure 2.2. Then for the non-constant modulus synthesized waveform, the m-th transmitted waveform is

$$s_m(t) = e^{i2\pi C(m) f_0 (t - \frac{1}{2K+1} T_0)} 1_{[0,T]}(t), \tag{2.4}$$

where $f_0 = 1/T_0$ is the pulse repetition frequency (PRF), and $C(m)f_0$ is the frequency offset of the m-th rectangular pulse. In fact, $C(m) \in [-K, K]$, $C(m)$ is integer, and $C(m) \neq C(n)$ when $m \neq n$. As a result, each transmitted waveform has unique frequency offset, and the offset is different from those in other transmitted waveforms. In the following part of this chapter, we define $q = T_0/(2K+1)$ for brevity.

Figure 2.2 and Figure 2.3 clearly show the difference in the amplitude variation of two synthesized waveforms, where the synthesized waveform in Figure 2.2 is constant amplitude within the whole signal duration T; on the other hand, the amplitude of

the synthesized waveform in Figure 2.3 varies with time, resulting in a signal with non-constant modulus.

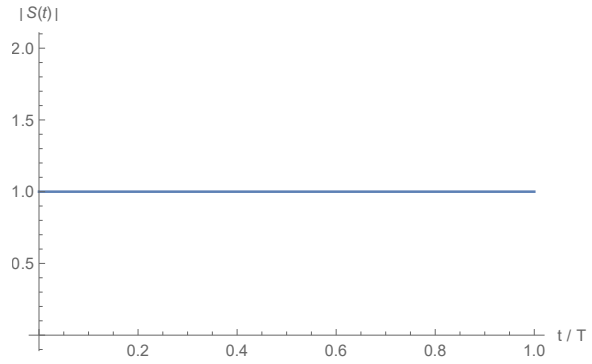

Fig. 2.2. Envelope of waveform synthesized by identical rectangular pulses.

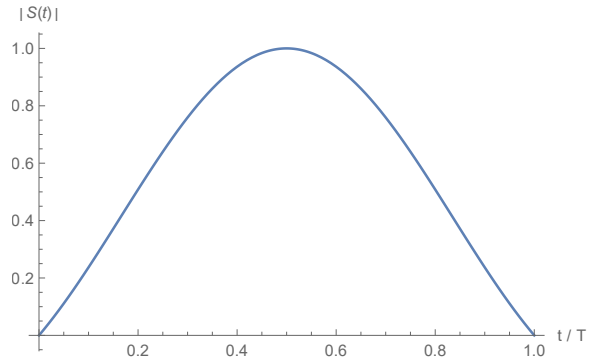

Fig. 2.3. Envelope of waveform synthesized by rectangular pulses with different frequency offsets.

2.2.2 Case 2: Waveform Synthesized by Identical Chirp Pulses vs. Waveform Synthesized by Chirp Pulses with Different Frequency Offsets

Similar to the previous case, we compare the differences between a constant modulus synthesized waveform and a non-constant modulus synthesized waveform, but

now we change from rectangular pulses to chirp pulses in each transmitted waveform. So, for the constant modulus synthesized waveform, each transmitted waveform is

$$s_m(t) = e^{i\pi\alpha t^2} 1_{[0,T]}(t), \tag{2.5}$$

where α is chirp rate. As for the non-constant modulus synthesized waveform, the m-th transmitted waveform is

$$s_m(t) = e^{i2\pi C(m) f_0 (t-q)} e^{i\pi\alpha t^2} 1_{[0,T]}(t). \tag{2.6}$$

Then the amplitude variations of two synthesized waveforms are the same as the former case, i.e., Figure 2.2 and 2.3. Therefore, from the above results, we showed that a waveform with non-constant modulus characteristic can be easily made by just adding constant modulus waveforms together.

2.3 Ambiguity Function Analysis of Non-Constant Modulus Waveform

In this section, we use the ambiguity function analysis to the same cases above to compare the delay-Doppler characteristics between constant modulus waveforms and non-constant modulus waveforms.

2.3.1 Case 1: Waveform Synthesized by Identical Rectangular Pulses vs. Waveform Synthesized by Rectangular Pulses with Different Frequency Offsets

a) Ambiguity Function Comparison

Here we investigate the ambiguity function of the above non-constant modulus synthesized waveform on target in the far field. The ambiguity function of $s(t)$ is

$$\begin{aligned}
\chi(\tau,\nu) &= \int_{\mathbb{R}} s(t)s^*(t-\tau)e^{-i2\pi\nu t}dt \\
&= \int_{\mathbb{R}} \left(\sum_{m=-K}^{K} e^{i2\pi C(m)f_0(t-q)}1_{[0,T]}(t)\right)\cdot\left(\sum_{m=-K}^{K} e^{-i2\pi C(m)f_0(t-\tau-q)}1_{[0,T]}(t-\tau)\right)e^{-i2\pi\nu t}dt \\
&= e^{-i\pi\nu(T+\tau)}\sum_{m=-K}^{K} e^{i2\pi C(m)f_0\tau}\cdot(T-|\tau|)\,\mathrm{sinc}(\nu(T-|\tau|))\cdot 1_{[0,T]}(|\tau|) \\
&\quad + e^{-i\pi[(C(n)-C(m))f_0+\nu](T+\tau)}\cdot\sum_{m=-K}^{K}\sum_{n=-K,n\neq m}^{K}\Big\{e^{i2\pi C(n)f_0\tau}e^{i2\pi(C(n)-C(m))f_0 q} \\
&\quad \cdot(T-|\tau|)\,\mathrm{sinc}\left(p(m,n)\cdot(T-|\tau|)\right)\cdot 1_{[0,T]}(|\tau|)\Big\}, \qquad (2.7)
\end{aligned}$$

where $p(m,n)=[C(n)-C(m)]f_0+\nu$. The first term is the auto ambiguity function of the component pulses in the combined waveform, and the second term is the cross ambiguity of component pulses in the combined waveform.

Figure 2.4 and Figure 2.5 are the ambiguity functions of the waveforms synthesized by identical rectangular pulses and synthesized by rectangular pulses with different frequency offsets. Figure 2.6 is the overlapped plot of the above two ambiguity functions. We can easily see from the figures that when (τ,ν) nears to $(0,0)$, $|\chi(\tau,\nu)|$ is greater in non-constant modulus synthesized waveform case than in constant modulus synthesized waveform case. The phenomenon indicates that in this case, the non-constant modulus waveform has slightly wider mainlobe width than the constant modulus waveform when we focus on small $|\tau|,|\nu|$. To compare the delay and Doppler characteristics of constant modulus and non-constant modulus wave-

forms more clearly, we use zero-delay cut and zero-Doppler cut by cutting through the ambiguity function at $\tau = 0$ and at $\nu = 0$.

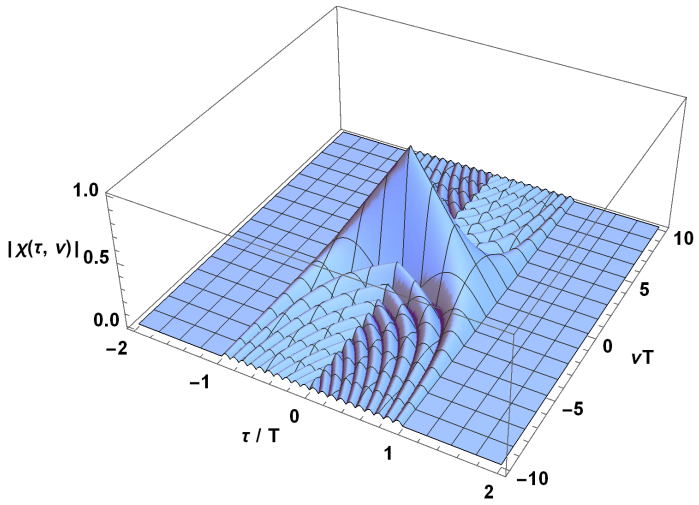

Fig. 2.4. Ambiguity function of the waveform synthesized by identical rectangular pulses.

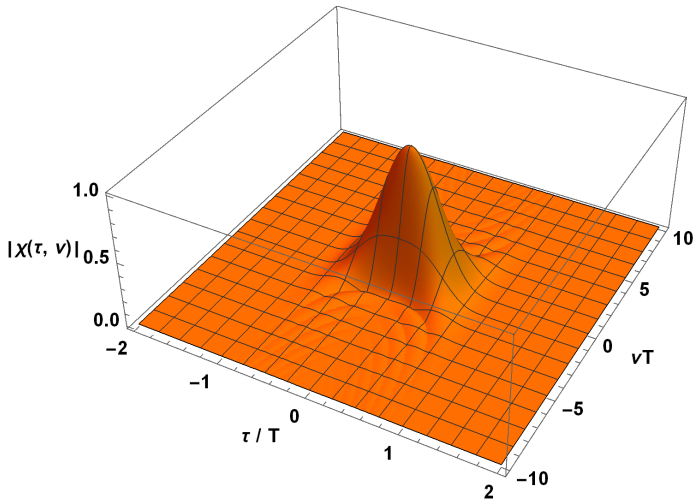

Fig. 2.5. Ambiguity function of the waveform synthesized by rectangular pulses with different frequency offsets.

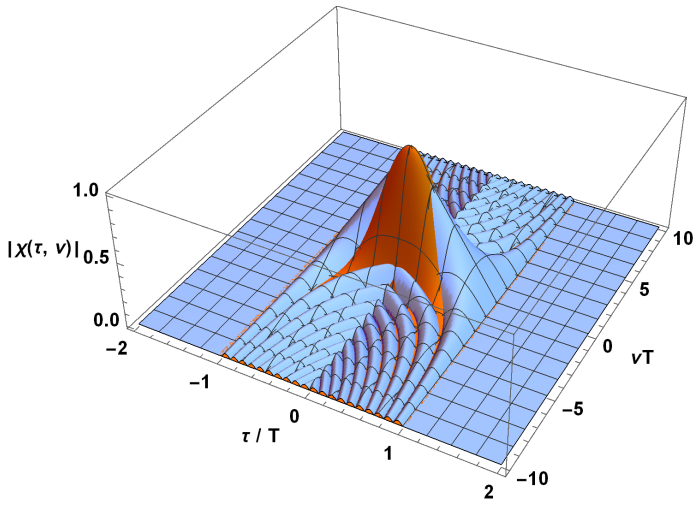

Fig. 2.6. Ambiguity functions overlapped by Figure 2.4 and Figure 2.5.

b) Zero-Delay Cut Comparison

Figure 2.7 is the plot of zero-delay cut of the constant modulus synthesized waveform (marked in blue dash line) and the non-constant modulus synthesized waveform (marked in orange line). The plot shows that for the non-constant modulus waveform, the mainlobe to peak sidelobe ratio is 39.11 dB, which is much higher than the mainlobe to peak sidelobe ratio of constant modulus waveform, 13.26 dB. However, in terms of the mainlobe width, the non-constant modulus waveform has slightly wider mainlobe width than the mainlobe width of constant modulus waveform. The mainlobe broadening effect is due to the fact that non-constant modulus waveform can be regarded as a rectangular pulse (constant modulus) multiplied by a weighting window, and the matched filter response in Doppler domain is the convolution of the rectangular pulse and the weight window in frequency domain.

c) Zero-Doppler Cut Comparison

Figure 2.8 is the plot of zero-Doppler cut of the constant modulus synthesized waveform (marked in blue dash line) and the non-constant modulus waveform syn-

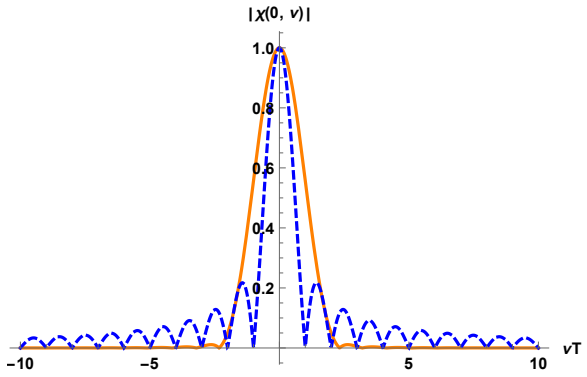

Fig. 2.7. Zero-delay cuts of the waveform synthesized by identical rectangular pulses (blue dashed line) and the waveform synthesized by rectangular pulses with different frequency offsets (orange line).

thesized (marked in orange line). The figure illustrates the results: 1) for small $|\tau|$, the non-constant modulus waveform has higher mainlobe height in delay response than the mainlobe height of the constant modulus waveform; 2) when $|\tau| \geq 0.23T$, the mainlobe height of the non-constant modulus waveform drops faster than the mainlobe height of the constant modulus waveform. The fast drop in mainlobe height comes from the fact that non-constant modulus waveform can be seen as a weighting window multiplied by the constant modulus pulse, then the mainlobe in delay response is compressed and can be more focused to improve the range resolution.

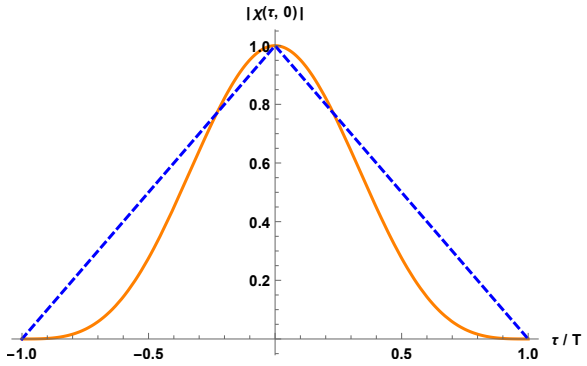

Fig. 2.8. Zero-Doppler cuts of the waveform synthesized by identical rectangular pulses (blue dashed line) and the waveform synthesized by rectangular pulses with different frequency offsets (orange line).

2.3.2 Case 2: Waveform Synthesized by Identical Chirp Pulses vs. Waveform Synthesized by Chirp Pulses with Different Frequency Offsets

a) Ambiguity Function Comparison

Here we investigate the ambiguity function of the above non-constant modulus synthesized waveform on target. The ambiguity function of $s(t)$ is

$$\begin{aligned}
&\chi(\tau,\nu) = \int_{\mathbb{R}} s(t)s^*(t-\tau)e^{-i2\pi\nu t}dt \\
&= \int_{\mathbb{R}} \left(\sum_{m=-K}^{K} e^{i2\pi C(m)f_0(t-q)} e^{i\pi\alpha t^2} 1_{[0,T]}(t) \right) \left(\sum_{m=-K}^{K} e^{-i2\pi C(m)f_0(t-\tau-q)} e^{-i\pi\alpha(t-\tau)^2} 1_{[0,T]}(t-\tau) \right) \\
&\quad \cdot e^{-i2\pi\nu t}dt \\
&= e^{-i\pi\alpha\tau^2} e^{-i\pi(\nu-\alpha\tau)(T+\tau)} \sum_{m=-K}^{K} e^{i2\pi C(m)f_0\tau} \cdot (T-|\tau|)\,\mathrm{sinc}((\nu-\alpha\tau)(T-|\tau|)) \cdot 1_{[0,T]}(|\tau|) \\
&\quad + e^{-i\pi\alpha\tau^2} e^{-i\pi[(C(n)-C(m))f_0+\nu-\alpha\tau](T+\tau)} \cdot \sum_{m=-K}^{K} \sum_{n=-K, n\neq m}^{K} \Big\{ e^{i2\pi C(n)f_0\tau} e^{i2\pi(C(n)-C(m))f_0 q} \\
&\quad \cdot (T-|\tau|)\,\mathrm{sinc}((p(m,n)-\alpha\tau)(T-|\tau|)) \cdot 1_{[0,T]}(|\tau|) \Big\}. \qquad (2.8)
\end{aligned}$$

The first term is the auto ambiguity function of the component pulses in the combined waveform, and the second term is the cross ambiguity of component pulses in the combined waveform.

Figure 2.9 and Figure 2.10 are the ambiguity functions of the waveforms synthesized by identical chirp pulses and synthesized by chirp pulses with different frequency offsets. Figure 2.11 is the overlapped plot of the above two ambiguity functions. We can easily see from the figures that when (τ,ν) nears to $(0,0)$, $|\chi(\tau,\nu)|$ is greater in non-constant modulus synthesized waveform than in constant modulus synthesized waveform. The phenomenon indicates that in this case, the non-constant modulus waveform has slightly wider mainlobe width than the constant modulus waveform when we focus on small $|\tau|, |\nu|$. To compare the delay and Doppler characteristics of constant modulus and non-constant modulus waveforms more clearly, we use zero-

delay cut and zero-Doppler cut by cutting through the ambiguity function at $\tau = 0$ and at $\nu = 0$.

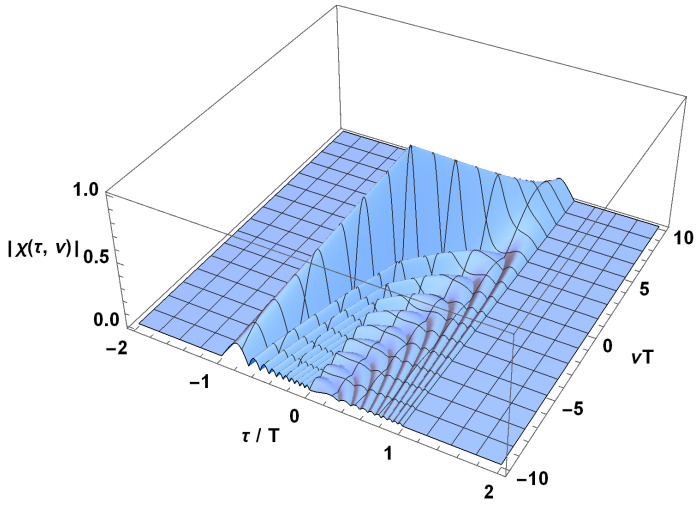

Fig. 2.9. Ambiguity function of the waveform synthesized by identical chirp pulses (constant modulus).

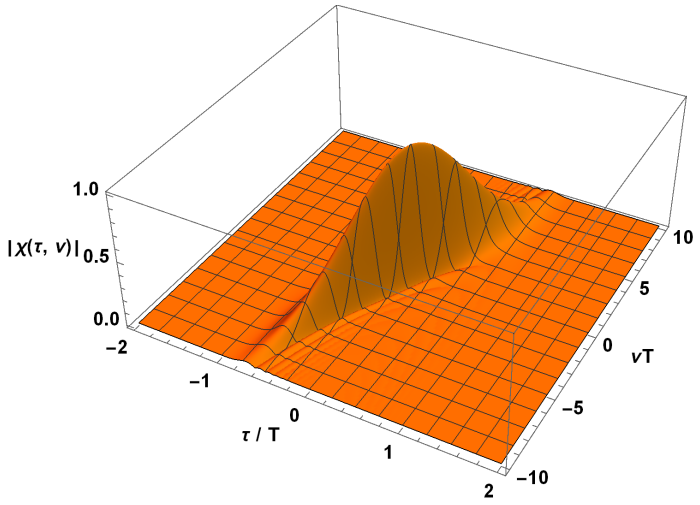

Fig. 2.10. Ambiguity function of the waveform synthesized by chirp pulses with different frequency offsets (non-constant modulus).

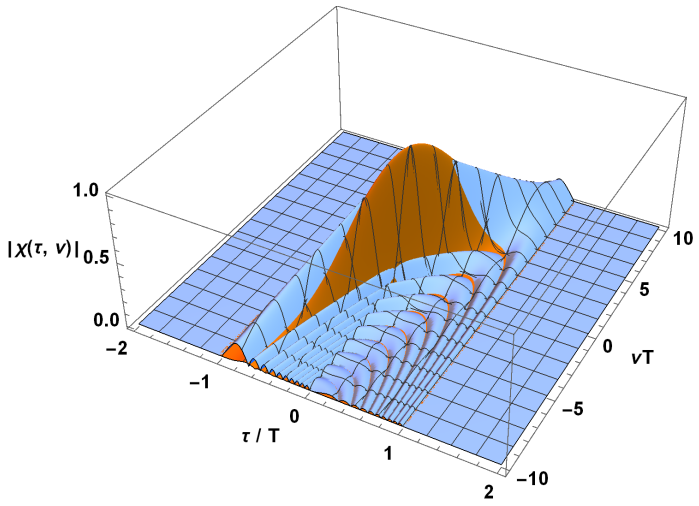

Fig. 2.11. Ambiguity function comparison of non-constant modulus synthesized waveform (chirps with different frequency offsets, shown in orange color) and constant modulus waveform (identical chirps, shown in blue color).

b) Zero-Delay Cut Comparison

Figure 2.12 is the plot of zero-delay cut of the constant modulus synthesized waveform (marked in blue dash line) and the non-constant modulus synthesized waveform (marked in orange line). The result shows that the mainlobe to peak sidelobe ratio of the non-constant modulus (chirp pulses with different frequency offsets) is 39.11 dB, which is the same as the previous case (rectangular pulses with different frequency offsets). In addition, it is also much larger than the mainlobe to peak sidelobe ratio of constant modulus waveform (identical chirp pluses), 13.26 dB. However, in terms of the mainlobe width, the non-constant modulus waveform has slightly wider mainlobe width than the mainlobe width of constant modulus waveform.

c) Zero-Doppler Cut Comparison

Figure 2.13 is the plot of zero-Doppler cut of the constant modulus synthesized waveform (marked with the blue dashed line) and the non-constant modulus waveform synthesized (marked with the orange line). The figure shows that the peak

range sidelobe of non-constant modulus synthesized waveform drops down to -32.92 dB, which is much lower than the peak range sidelobe level of constant modulus synthesized waveform, -14.89dB.

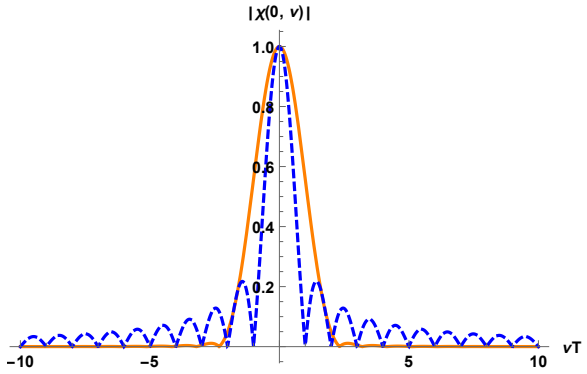

Fig. 2.12. Zero-delay cuts of the waveform synthesized by identical chirp pulses (blue dashed line) and the waveform synthesized by chirp pulses with different frequency offsets (orange line).

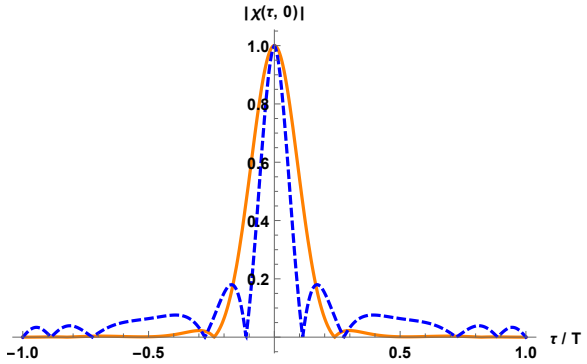

Fig. 2.13. Zero-Doppler cuts of the waveform synthesized by identical chirp pulses (blue dashed line) and the waveform synthesized by chirp pulses with different frequency offsets (orange line).

Furthermore, for the consideration of time-bandwidth product, we let the non-constant modulus waveform and the constant modulus waveform have same time-bandwidth product, then the equivalent chirp rate of identical chirp pulses is $\alpha_{eq} = K/(T_0T)+\alpha$. Figure 2.14 is the overlapped ambiguity functions of non-constant modulus waveform (chirp pluses with different frequency offsets) and constant modulus

waveform (identical chirp pulses). The chirp rate is α_{eq}. Figure 2.15 is the zero-delay cut comparison, and Figure 2.16 is the zero-Doppler cut comparison. Apparently, the mainlobe to peak sidelobe ratio of non-constant modulus waveform is still greater than the mainlobe to peak sidelobe ratio of constant modulus waveform at the expense of slightly wider mainlobe width.

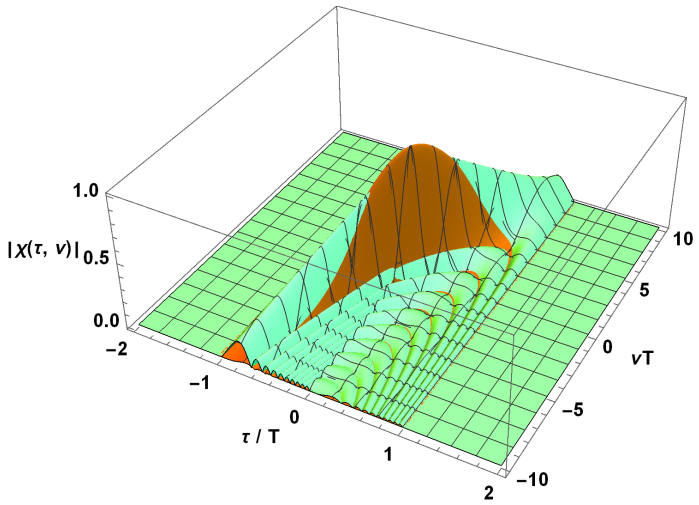

Fig. 2.14. Ambiguity function comparison of the non-constant modulus synthesized waveform (chirps with different frequency offsets, shown in orange color) and the constant modulus waveform (identical chirp with the equivalent chirp rate α_{eq}, shown in green color).

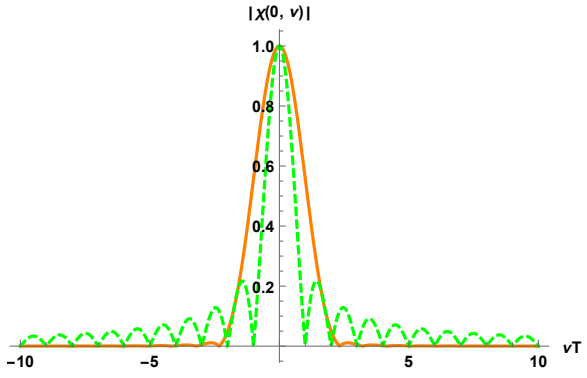

Fig. 2.15. Zero-delay cuts of the waveform synthesized by identical chirp pulses (with chirp rate α_{eq}, green dashed line) and the waveform synthesized by chirp pulses with different frequency offsets (orange line).

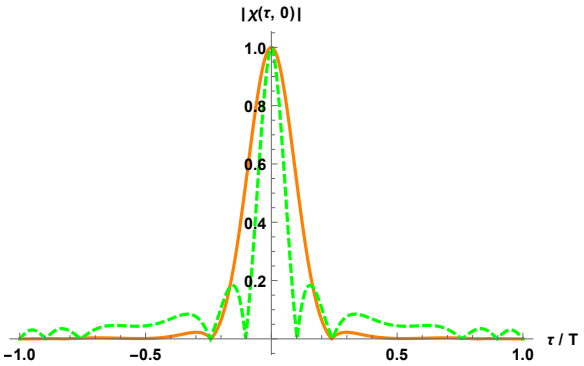

Fig. 2.16. Zero-Doppler cuts of the waveform synthesized by identical chirp pulses (with chirp rate α_{eq}, green dashed line) and the waveform synthesized by chirp pulses with different frequency offsets (orange line).

Although the non-constant modulus waveform has better performance in terms of the mainlobe to peak sidelobe ratio, there is a slight decrease in energy density on target compared to the energy density of waveform synthesized by identical chirps. This is a small disadvantage. This is due to the signal cancellation of cross ambiguity of component pulses, resulting the energy density on target that is not as large as when we apply the same constant modulus waveform in each transmitted element. However, if the signal to noise ratio (SNR) is large enough, then the non-constant modulus waveform will perform well.

2.4 Angular Resolution Analysis of Non-Constant Modulus Waveform

When the target is in a different direction, the synthesized signal at the target is the combination of the constant modulus waveforms with different phase shifts, causing constructive and destructive interference. Then the energy density at the target will vary, resulting in an angular resolution issue. To improve the angular resolution, we investigate the performance in terms of angular resolution of combined non-constant modulus waveforms. Figure 2.17 shows that when targets are in different directions, the transmitted signal from each transmitted antenna array element has

different phase shifts, and the combination of each phase-shifted waveform leads to the angular resolution issue.

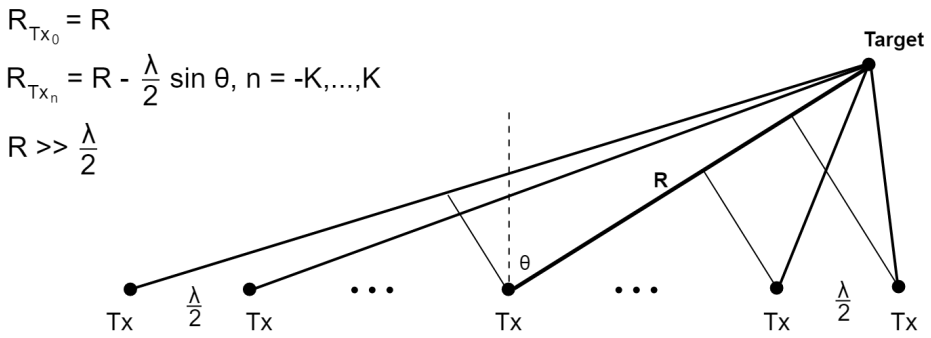

Fig. 2.17. The target is off boresight, causing different phase shifts in each transmitted waveform.

In Figure 2.17, we know that the synthesized waveform at the target with angle θ from each transmitted array element consisting of $2K+1$ transmitters can be expressed in the following general form:

$$\begin{aligned} s(t,\theta) =& s_{-K}(t)e^{-i\frac{2\pi}{\lambda}(R-(-K\frac{\lambda}{2}\sin\theta))} \\ &+ s_{-(K-1)}(t)e^{-i\frac{2\pi}{\lambda}(R-(-(K-1)\frac{\lambda}{2}\sin\theta))} \\ &+ \cdots \\ &+ s_0(t)e^{-i\frac{2\pi}{\lambda}R} \\ &+ \cdots \\ &+ s_{K-1}(t)e^{-i\frac{2\pi}{\lambda}(R-((K-1)\frac{\lambda}{2}\sin\theta))} \\ &+ s_K(t)e^{-i\frac{2\pi}{\lambda}(R-(K\frac{\lambda}{2}\sin\theta))} \\ =& e^{-i\frac{2\pi}{\lambda}R}\sum_{m=-K}^{K} s_m(t)e^{im\pi\sin\theta}. \end{aligned} \tag{2.9}$$

Now, assume $e^{-i\frac{2\pi}{\lambda}R} = 1$ (WLOG), then we have

$$\begin{aligned} s(t,\theta) &= \sum_{m=-K}^{K} s_m(t)e^{im\pi\sin\theta} \\ &= \sum_{m=-K}^{K} s_m(t,\theta). \end{aligned} \tag{2.10}$$

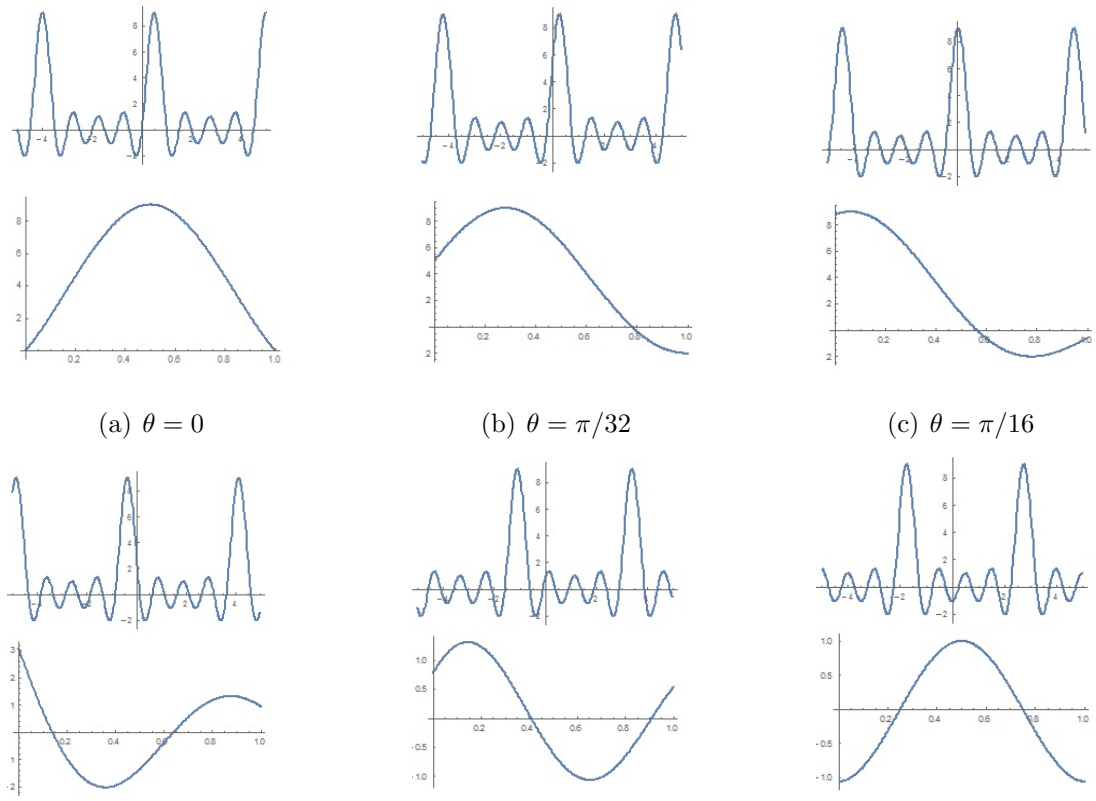

(a) $\theta = 0$ (b) $\theta = \pi/32$ (c) $\theta = \pi/16$

(d) $\theta = \pi/8$ (e) $\theta = \pi/4$ (f) $\theta = \pi/2$

Fig. 2.18. non-constant modulus synthesized waveform at different angles θ.

Just as with the previous non-constant modulus (chirp pulses with different frequency offsets) case, we let $s_m(t) = e^{i2\pi C(m) f_0 (t-q)} e^{i\pi\alpha t^2} 1_{[0,T]}(t)$; then the envelopes of the synthesized non-constant modulus waveform at different angles θ, i.e., $s(t,\theta)$, are shown in Figure 2.18. Then, based on the differences at different angles with respect to array boresight, angular resolution of $s(t,\theta)$ can be measured by finding $\max_{\tau,\nu} |\chi(\tau,\nu,0,\theta)|$ at every angle θ, where

$$\chi(\tau,\nu,0,\theta) = \int_{\mathbb{R}} s(t,0) s^*(t-\tau,\theta) e^{-i2\pi\nu t} dt.$$

For our non-constant modulus waveform case, we have:

$$
\begin{aligned}
&\chi(\tau,\nu,0,\theta)=\int_{\mathbb{R}} s(t,0)s^{*}(t-\tau,\theta)e^{-i2\pi\nu t}dt\\
&=\int_{\mathbb{R}}\left(\sum_{m=-K}^{K} s_m(t,0)\right)\left(\sum_{n=-K}^{K} s_n(t-\tau,\theta)\right)^{*} e^{-i2\pi\nu t}dt\\
&=\int_{\mathbb{R}}\left(\sum_{m=-K}^{K} e^{i2\pi C(m)f_0(t-q)}e^{i\pi\alpha t^2}e^{im\pi\sin 0}1_{[0,T]}(t)\right)\\
&\quad\cdot\left(\sum_{n=-K}^{K} e^{i2\pi C(n)f_0(t-\tau-q)}e^{i\pi\alpha(t-\tau)^2}e^{in\pi\sin\theta}1_{[0,T]}(t-\tau)\right)^{*} e^{-i2\pi\nu t}dt\\
&=e^{-i\pi\alpha\tau^2}\sum_{m=-K}^{K}\sum_{n=-K}^{K}\Big\{e^{-in\pi\sin\theta}e^{i2\pi f_0C(n)\tau}e^{i2\pi f_0(C(n)-C(m))q}e^{-i\pi[p(m,n)-\alpha\tau](T+\tau)}\\
&\quad\cdot(T-|\tau|)\,\mathrm{sinc}((p(m,n)-\alpha\tau)(T-|\tau|))\cdot 1_{[0,T]}(|\tau|)\Big\}.
\end{aligned}
$$

Now we observe the angular resolution by plotting $\max_{\tau,\nu}|\chi(\tau,\nu,0,\theta)|$ with θ, where $\theta\in[0,\pi/4]$. Three cases are compared: 1) constant modulus waveform (synthesized by identical chirp pulses, shown in gray color) 2) non-constant modulus waveform (synthesized by chirp pulses with the frequency offset indices order $\{C(m)\colon m=-K,-(K-1),\cdots,-1,0,1,\cdots,K-1,K\}=\{-1,2,-3,4,0,-4,3,-2,1\}$, shown in orange color) 3) non-constant modulus waveform (synthesized by chirp pulses with the frequency offset indices order $\{C(m)\colon m=-K,-(K-1),\cdots,-1,0,1,\cdots,K-1,K\}=\{-1,2,-3,4,-4,3,-2,1,0\}$, shown in blue color).

From the above result we know that the frequency offset indices order arrangement will influence the performance in terms of the angular resolution [6]. In Figure 2.19, when the frequency offset order $C(m)$ is properly arranged, a non-constant modulus synthesized waveform can have slightly narrower mainlobe width than the mainlobe width of a constant modulus waveform, then the non-constant modulus synthesized waveform can have better angular resolution than the angular resolution of transmitting identical constant modulus signal at each antenna array element.

In addition, Figure 2.19 shows the difference about the mainlobe to peak sidelobe ratio of the three cases. For the constant modulus waveform case (gray), the

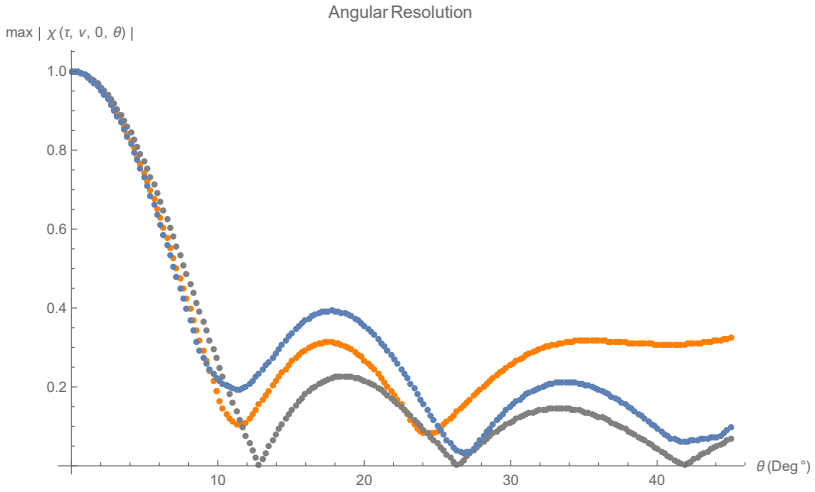

Fig. 2.19. Angular resolution comparison: 1) constant modulus waveform (gray dotted line) 2) non-constant modulus waveform (chirp pulses with the frequency offset indices order $\{C(m)\colon m = -K, -(K-1), \cdots, -1, 0, 1, \cdots, K-1, K\} = \{-1, 2, -3, 4, 0, -4, 3, -2, 1\}$, orange dotted line) 3) non-constant modulus waveform (chirp pulses with the frequency offset indices order $\{C(m)\colon m = -K, -(K-1), \cdots, -1, 0, 1, \cdots, K-1, K\} = \{-1, 2, -3, 4, -4, 3, -2, 1, 0\}$, blue dotted line).

mainlobe to peak sidelobe ratio is 12.90 dB; for the non-constant modulus waveform (chirp pulses with the frequency offset indices order $\{C(m)\colon m = -K, -(K-1), \cdots, -1, 0, 1, \cdots, K-1, K\} = \{-1, 2, -3, 4, 0, -4, 3, -2, 1\}$, orange), the mainlobe to peak sidelobe ratio is 9.80 dB; for the non-constant modulus waveform (chirp pulses with the frequency offset indices order $\{C(m)\colon m = -K, -(K-1), \cdots, -1, 0, 1, \cdots, K-1, K\} = \{-1, 2, -3, 4, -4, 3, -2, 1, 0\}$, blue), the mainlobe to peak sidelobe ratio is 8.12 dB.

From the above results, we know that when the frequency offset order $C(m)$ is properly arranged, a non-constant modulus synthesized waveform can have slightly better angular resolution than the angular resolution of a constant modulus waveform. However, slightly lower mainlobe to peak sidelobe ratio is a penalty for using the above non-constant modulus synthesized waveform.

2.5 Energy Density Analysis of Non-Constant Modulus Waveform

When the reflection of the waveforms by targets in directions other than the intended direction, because the synthesized signal at the target is combined by waveforms with different phase shifts, it will cause some part of signal cancellations, and some interference appears. As a result, the energy density at targets will decrease.

To investigate the energy density of the above mentioned non-constant modulus waveform, we can find: $\max\limits_{\tau,\nu}|\chi(\tau, \nu, \theta, \theta)|$ at any angle θ, where

$$\chi(\tau, \nu, \theta, \theta) = \int_{\mathbb{R}} s(t, \theta) s^*(t - \tau, \theta) e^{-i2\pi\nu t} dt.$$

For the non-constant modulus synthesized waveform,

$$s_m(t) = e^{j2\pi C(m) f_0 (t-q)} e^{i\pi\alpha t^2} 1_{[0,T]}(t),$$

and then

$$
\begin{aligned}
&\chi(\tau,\nu,\theta,\theta)=\int_{\mathbb{R}} s(t,\theta)s^{*}(t-\tau,\theta)e^{-i2\pi\nu t}dt\\
&=\int_{\mathbb{R}}\left(\sum_{m=-K}^{K} s_m(t,\theta)\right)\left(\sum_{n=-K}^{K} s_n(t-\tau,\theta)\right)^{*} e^{-i2\pi\nu t}dt\\
&=\int_{\mathbb{R}}\left(\sum_{m=-K}^{K} e^{i2\pi C(m)f_0(t-q)}e^{i\pi\alpha t^2}e^{im\pi\sin\theta}1_{[0,T]}(t)\right)\\
&\quad\cdot\left(\sum_{n=-K}^{K} e^{i2\pi f_0 C(n)(t-\tau-q)}e^{i\pi\alpha(t-\tau)^2}e^{in\pi\sin\theta}1_{[0,T]}(t-\tau)\right)^{*} e^{-i2\pi\nu t}dt\\
&=e^{-i\pi\alpha\tau^2}\sum_{m=-K}^{K}\sum_{n=-K}^{K}\Big\{e^{i(m-n)\pi\sin\theta}e^{i2\pi C(n)f_0\tau}e^{i2\pi(C(n)-C(m))f_0 q}e^{-i\pi[p(m,n)-\alpha\tau](T+\tau)}\\
&\quad\cdot(T-|\tau|)\,\mathrm{sinc}((p(m,n)-\alpha\tau)\cdot(T-|\tau|))\cdot 1_{[0,T]}(|\tau|)\Big\}.
\end{aligned}
$$

Just as in the previous discussions, here we compare the difference in terms of energy density at targets of 1) constant modulus waveform (synthesized by identical chirp pulses, shown in gray color), 2) non-constant modulus waveform (synthesized by chirp pulses with the frequency offset indices order $\{C(m)\colon m=-K,-(K-1),\cdots,-1,0,1,\cdots,K-1,K\}=\{-1,2,-3,4,0,-4,3,-2,1\}$, shown in orange color), and 3) non-constant modulus waveform (synthesized by chirp pulses with the frequency offset indices order $\{C(m)\colon m=-K,-(K-1),\cdots,-1,0,1,\cdots,K-1,K\}=\{-1,2,-3,4,-4,3,-2,1,0\}$, shown in blue color). Each transmitted signal duration is T, and $T=2T_0/(2K+1)$, where T_0 is pulse repetition interval.

From Figure 2.20 we observe that the energy density at targets in different angles is distributed more evenly in the non-constant modulus waveform case than in the constant modulus waveform case. However, due to the signal cancellations in the non-constant modulus synthesized waveform, the signal energy at targets is much smaller in the non-constant modulus waveform than in the constant modulus waveform under the consideration of same total transmitted energy.

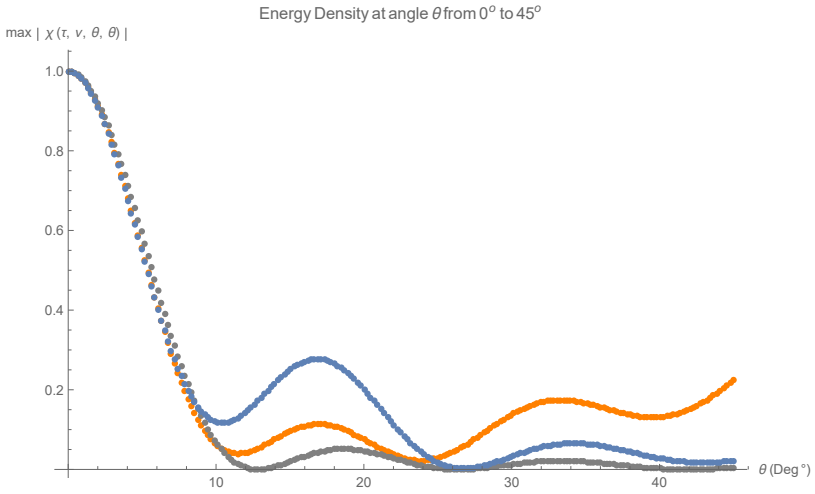

Fig. 2.20. Energy density comparison: 1) constant modulus waveform (gray dotted line) 2) non-constant modulus waveform (chirp pulses with the frequency offset indices order $\{C(m)\colon m = -K, -(K-1), \cdots, -1, 0, 1, \cdots, K-1, K\} = \{-1, 2, -3, 4, 0, -4, 3, -2, 1\}$, orange dotted line) 3) non-constant modulus waveform (chirp pulses with the frequency offset indices order $\{C(m)\colon m = -K, -(K-1), \cdots, -1, 0, 1, \cdots, K-1, K\} = \{-1, 2, -3, 4, -4, 3, -2, 1, 0\}$, blue dotted line).

2.6 Conclusion

We have proposed an easy way to generate non-constant modulus waveforms by summing constant modulus waveforms from each transmitted array element, and we have shown from the ambiguity function that the performance in terms of mainlobe to peak sidelobe ratio in zero-delay and zero-Doppler greatly increased comparing to the delay-Doppler response of constant modulus waveform. Moreover, non-constant modulus waveforms can be easily generated by just gating on and off each transmitter in-sync, and the combined signal at targets is a non-constant modulus signal. In this way, we can get rid of the mismatch loss problem, which is caused by applying the amplitude weighting in the receiver only.

Furthermore, we proposed that non-constant modulus waveforms can have better angular resolution than constant modulus waveforms by analyzing the ambiguity function. When the target's direction changes, the synthesized non-constant modulus waveform at the target will cause the ambiguity mainlobe peak to drop down more quickly than using the constant modulus waveform, resulting the better angular resolution. However, the decrease of mainlobe to peak sidelobe ratio in spatial domain is a drawback of this non-constant modulus waveforms.

Moreover, when we synthesize the non-constant modulus waveform, if the reflection of the waveform by targets in directions other than the intended direction, interference occurs. In addition, these phase-shifted waveforms are not added in-phase, resulting in partial signal cancellation in the cross ambiguity functions, and then the signal energy on target drops. Instead, if we let the transmitted waveforms keep in one whole period, i.e., $T = T_0$ (full duty), then the signal energy remains constant at any angle θ. Figure 2.21 shows the energy density comparison of the non-constant modulus synthesized waveform (blue dotted line) and the constant modulus synthesized waveform (gray dotted line) when the one whole period of transmitted waveform at each transmitter is considered. Here we can clearly observe that this family of non-constant modulus synthesized waveforms own the "omni-directional"

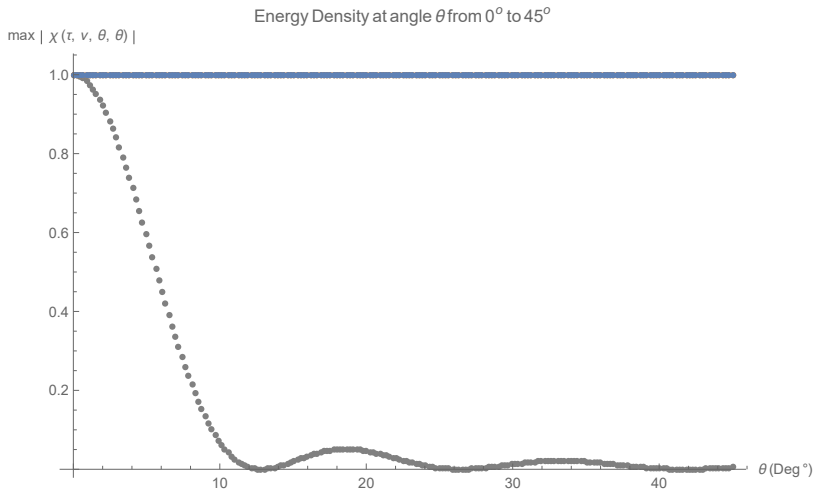

Fig. 2.21. Energy density comparison: 1) constant modulus waveform(gray dotted line) 2) non-constant modulus waveform (blue dotted line). The pulse duration in each transmitted waveform is one whole period.

transmission ability, i.e., equal signal energy at any angle θ with equal distance. This is an advantage of applying this kind of non-constant modulus waveform syntheses.

However, delay-Doppler resolution and angular resolution may be affected when one whole period of signal transmission is considered. Figure 2.22 is the angular resolution comparison of the non-constant modulus synthesized waveform (blue dotted line) and the constant modulus synthesized waveform (gray dotted line) when the one whole period of transmitted waveform at each transmitter is considered. The mainlobe widths are almost the same in the constant modulus waveform and the non-constant modulus waveform, meaning that they have almost the same angular resolution; however, the mainlobe to peak sidelobe ratio is much worse in the non-constant modulus waveform. Therefore, how to nicely pick the family of constant modulus waveforms to synthesize a non-constant modulus waveform—which has better performance in terms of delay-Doppler resolution, angular resolution, and "omni-directional" property—is then an important issue.

In summary, in this chapter we proposed a non-constant modulus waveform generation method by simply combining different constant modulus waveform. Compared

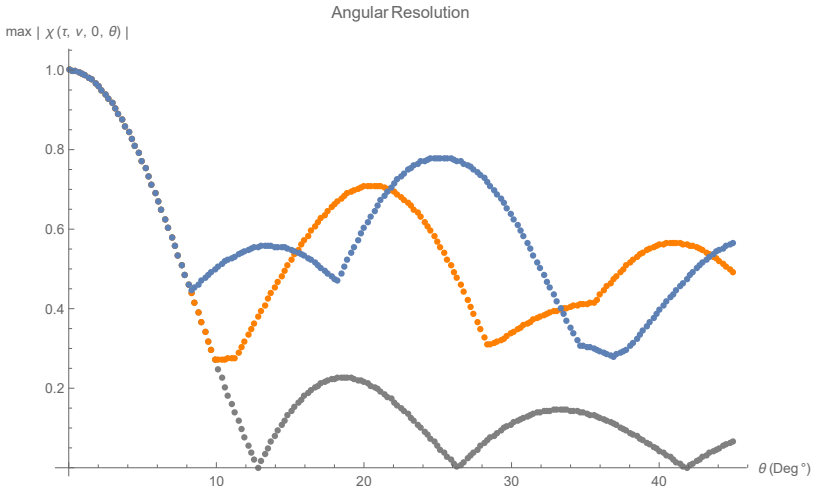

Fig. 2.22. Angular resolution comparison: 1) constant modulus waveform (gray dotted line) 2) non-constant modulus waveform (chirp pulses with the frequency offset indices order $\{C(m)\colon m = -K, -(K-1), \cdots, -1, 0, 1, \cdots, K-1, K\} = \{-1, 2, -3, 4, 0, -4, 3, -2, 1\}$, orange dotted line) 3) non-constant modulus waveform (chirp pulses with the frequency offset indices order $\{C(m)\colon m = -K, -(K-1), \cdots, -1, 0, 1, \cdots, K-1, K\} = \{-1, 2, -3, 4, -4, 3, -2, 1, 0\}$, blue dotted line). The pulse duration in each transmitted waveform is one whole period.

to the constant modulus waveform, the non-constant modulus waveform possesses the advantages such as the better delay-Doppler resolutions and the better angular resolution. However, in terms of the mainlobe to peak sidelobe ratio in spatial domain and the total signal energy at target, non-constant modulus waveform may have slightly inferior performance. Therefore, these analyses and the trade-offs are helpful in the performance assessment and the design of a radar system.

3. IMPROVED TARGET RESOLUTION AND PARAMETER ESTIMATION IN CHIRP RADAR SYSTEMS

3.1 Introduction

Target discrimination—the ability to discern multiple target returns—is an important function of radar systems. It determines not only the ability of detecting multiple targets with close ranges and Doppler shifts, but also the estimation accuracy of targets' delays and Doppler shifts. The linear frequency-modulated (LFM) waveform, one kind of chirp waveform, is the most widely used radar waveform because of its good range and Doppler resolution [8–10, 29, 35]. Because of these properties, it can easily discriminate targets either with the same speed but different distances or with the same distance but different speeds.

Even though the chirp waveform has good range and Doppler resolution properties separately, in some situations, the chirp waveform still has poor resolution and cannot easily resolve targets. It is known that the matched filter output response of a linear chirp pulse has a triangular envelope along the α-rotated axis ($\nu = \alpha\tau$) in the delay-Doppler plane, where α is the chirp rate of the chirp pulse. When any pair of targets are close enough in delay and Doppler shift, and they have a Doppler shift difference which equals to their delay difference multiplied by the chirp rate of the transmitted chirp waveform α, the traditional chirp matched filter output response will have a mixed envelope made up of two partially overlapping triangular envelopes. Furthermore, when one of the two target returns is smaller than the other, the smaller triangular envelope may be concealed in the mixed envelope, causing a missed detection of the smaller target. In this situation, the chirp matched filtering process may not work well in detecting and resolving the two targets.

To solve this problem, we introduce a new technique, *noise-target fringe analysis*, that can effectively estimate the targets' delay information. Moreover, we apply the CLEAN algorithm [41] along with the above-mentioned target-delay estimate technique to further estimate the Doppler shifts and amplitudes of the targets. This target parameter estimation method has high accuracy in target parameter estimate and improves the ability of target differentiation along the slope α chirp response ridge.

Furthermore, to acquire much more accurate target parameter estimates, we apply a Gauss-Newton algorithm [42, 43], one of the weighted non-linear least squares optimization methods, to further improve the estimate performance. Simulation results show that by applying this method, we can improve the successful target parameter estimate probability by up to 90%, which can significantly improve target discrimination.

Also, in terms of system complexity issues, the noise-target fringe analysis method only needs to know the instantaneous phase difference of the delay-Doppler output samples, which is the difference between the instantaneous phase of two neighboring delay-Doppler output samples. Moreover, for the case of multiple targets lying along a ridge line with slope α, we apply the CLEAN algorithm to pick the delay-Doppler point with the largest amplitude response from the "whole delay-Doppler matched filter output response-only" rather than iteratively pick the point with the largest amplitude from the residual responses. We only need to calculate the phase difference of the delay-Doppler output samples on the line segment through the previous CLEAN-selected point and with slope α from the residual delay-Doppler output responses. We eliminate the iterative CLEAN-picking process and only pick one delay-Doppler point in the beginning. Therefore, this target parameter estimate method is practically implementable with minimal complexity. As for the Gauss-Newton optimization, it contains matrix inversions and matrix multiplications, which may need more computational power. But in some non-real time (time-tolerable) radar systems, it is

still valuable to implement this optimization method to pursue more accurate target parameter estimates.

In Section 3.2 of this chapter, we formulate a mathematical model of the matched filter output response. We then apply the chirp waveform to this model to formulate the chirp matched filter output response used in the rest of this chapter. In Section 3.3, we demonstrate the noise-target fringe analysis method to effectively estimate targets' delays. In Section 3.4, we apply the weighted non-linear least squares optimization method to the chirp matched filter output and provide a more detailed analysis of acquiring the least squares estimates of the target parameters. In Section 3.5, we provide the noise and signal-to-noise ratio (SNR) analyses throughout the whole radar system. In Section 3.6, we demonstrate the target parameter estimate system and its processing algorithm. Then in Section 3.7, we provide the performance analysis of the target parameter estimate accuracy. Finally, we summarize the estimator performance and conclude by presenting the feasibility of the target parameter estimate approach in the non-LFM radar systems.

3.2 Mathematical Model for Matched Filter

Consider a radar system in which a waveform $s_{Tx}(t)$ with finite duration T and with finite energy is generated and transmitted by the radar. At the receiver, the received waveform is the sum of all targets' reflected waveforms (here we assume that for target k, the delay and Doppler shift are (τ_k, ν_k), $k = 1, 2, \cdots, K$, where K is the total number of target returns). This can be represented as

$$s_{Recv}(t) = \sum_{k=1}^{K} a_k s_{Tx}(t - \tau_k) e^{i2\pi\nu_k t}, \tag{3.1}$$

where the a_k is the amplitude of the k-th target's reflected waveform, τ_k is the delay (two-way) of the k-th target's reflected waveform, and ν_k is the Doppler shift of the k-th target's reflected waveform. Note that any two different targets, which are at (τ_m, ν_m) and $(\tau_n, \nu_n), m \neq n$, can only have the same delay $(\tau_m = \tau_n)$ or the same

Doppler shift ($\nu_m = \nu_n$) because we regard two targets with the same delay and same Doppler shift ($\tau_m = \tau_n$ and $\nu_m = \nu_n$) as the same target.

As for the matched filter, the matching template waveform matched to τ-delayed, ν-Doppler shifted is

$$g_{\tau\nu}(t) = s_{Tx}(t-\tau)e^{i2\pi\nu t}. \tag{3.2}$$

Then, the matched filter impulse response $\tilde{h}_{\tau\nu}(t)$ will be of the form

$$\begin{aligned}\tilde{h}_{\tau\nu}(t) &= g^*_{\tau\nu}(T+\tau-t)\\ &= s^*_{Tx}(T+\tau-t-\tau)e^{-i2\pi\nu(T+\tau-t)}\\ &= s^*_{Tx}(T-t)e^{-i2\pi\nu(T+\tau-t)},\end{aligned} \tag{3.3}$$

and the matched filter output at time $t = T+\tau$ will be

$$\begin{aligned}\tilde{O}_{\mathrm{MF}}(\tau,\nu) &= s_{Recv}(t) * \tilde{h}_{\tau\nu}(t)|_{t=T+\tau}\\ &= \int_{-\infty}^{\infty} s_{Recv}(p)\tilde{h}_{\tau\nu}(t-p)dp|_{t=T+\tau}\\ &= \int_{-\infty}^{\infty} s_{Recv}(p)\tilde{h}_{\tau\nu}(T+\tau-p)dp\\ &= \int_{-\infty}^{\infty} \sum_k a_k s_{Tx}(p-\tau_k)e^{i2\pi\nu_k p}\cdot s^*_{Tx}(p-\tau)e^{-i2\pi\nu p}dp\\ &= \sum_k a_k \left(\int_{-\infty}^{\infty} s_{Tx}(p-\tau_k)s^*_{Tx}(p-\tau)e^{-i2\pi(\nu-\nu_k)p}dp\right)\\ &\quad (\text{let } p-\tau_k = m_k,\ p = m_k+\tau_k, \text{ and } dp = dm_k)\\ &= \sum_k a_k e^{-i2\pi(\nu-\nu_k)\tau_k}\int_{-\infty}^{\infty} s_{Tx}(m_k)s^*_{Tx}(m_k-(\tau-\tau_k))e^{-i2\pi(\nu-\nu_k)m_k}dm_k\\ &= \sum_k a_k e^{-i2\pi(\nu-\nu_k)\tau_k}\chi_s(\tau-\tau_k,\nu-\nu_k),\end{aligned} \tag{3.4}$$

where

$$\chi_s(\tau,\nu) = \int_{-\infty}^{\infty} s_{Tx}(t)s^*_{Tx}(t-\tau)e^{-i2\pi\nu t}dt$$

is the ambiguity function of the waveform $s_{Tx}(t)$. From the above equation we know that $\tilde{O}_{\mathrm{MF}}(\tau,\nu)$, the matched filter output response sampled at time $t = T+\tau$, is

the combination of weighted and phase-shifted version of (τ_k, ν_k)-shifted ambiguity functions, where $k = 1, \cdots, K$.

In reality, a received waveform consists of all target returns and the input noise, i.e.,

$$s_{Recv}(t) = \sum_{k=1}^{K} a_k s_{Tx}(t - \tau_k) e^{i2\pi\nu_k t} + w(t), \tag{3.5}$$

where $w(t)$ is the noise at the receiver input. In this paper, we assume that $w(t)$ is additive white Gaussian noise with zero-mean and the two-sided power spectral density (PSD) $N_0/2$. Then the matched filter output is the combination of all targets' output responses plus the noise response at the matched filter output. Hence, we can write the whole delay-Doppler response observed at the matched filter output as

$$\begin{aligned} \tilde{O}(\tau, \nu) &= \tilde{O}_{\mathrm{MF}}(\tau, \nu) + N(\tau, \nu) \\ &= \sum_{k=1}^{K} a_k e^{-i2\pi(\nu-\nu_k)\tau_k} \chi_s(\tau - \tau_k, \nu - \nu_k) + N(\tau, \nu), \end{aligned} \tag{3.6}$$

where

$$\begin{aligned} N(\tau, \nu) &= w(t) * \tilde{h}_{\tau\nu}(t) \,|_{t=T+\tau} \\ &= \int_{-\infty}^{\infty} w(p) s_{Tx}^{*}(p - \tau) e^{-i2\pi\nu p} dp \end{aligned}$$

is the cross ambiguity function of the noise and the transmitted waveform.

From the above we know that because all information about the target returns are unknown, and we only have the combination of noise and all targets' matched filter outputs, it is very hard to differentiate all targets and effectively estimate the distances, moving speeds and intensities of all target returns. Hence, radar target parameter estimate has become an interesting and important research issue [44–46], and researchers were devoted to not only finding waveforms with good delay and Doppler resolution properties but coming up with simple and efficient algorithms to improve target discrimination ability.

From the viewpoint of waveform design, chirp radar is one of the most prevalent radar systems used nowadays because of its good delay-Doppler resolution and easy-

implementation. However, chirp radars have poor resolution along the ridge with slope α in the delay-Doppler plane, where α is the chirp rate of the chirp waveform. This is due to the fact that the chirp ambiguity function is a rotated and sheered version (with slope α) of the ambiguity function of an unmodulated pulse. Therefore, when target returns are close and lying on a ridge line with slope α in the delay-Doppler plane, we can barely differentiate these targets from the chirp matched filter output response.

Also, an efficient algorithm to effectively provide the target estimates is also important. The CLEAN algorithm, one kind of image deconvolution method, was first proposed and published by Jan Högbom in radio astronomy [41]. After that, several different variations and improvements of the CLEAN algorithm were published [25–28, 47–49]. However, the rationale of the CLEAN algorithm is the same: we assume an image which is constituted by a number of point sources. Then the CLEAN algorithm iteratively picks the highest value in the residual image and subtract the weighted response of this point source. The weighted response is the convolution of the weighted gain and the point spread function (PSF) of the observation. The algorithm proceeds until the highest value of the image is smaller than some assigned threshold.

In radar systems, we can regard the observed matched filter output response as a complex image in delay and Doppler, and we apply the CLEAN algorithm to iteratively select the highest amplitude (the position with the highest energy intensity) in the residual matched filter output response and subtract a weighted response, which is the delay-Doppler response centered on the CLEAN-estimated target position, as shown in Equation (3.4). In this way, we can sequentially identify individual targets until the noise-only response remains. In the following we use an example to show how the CLEAN algorithm be applied in radar systems.

Figures 3.1, 3.2 and 3.3 show the residual responses $\tilde{O}^{(0)}_{Res}(\tau,\nu)$, $\tilde{O}^{(1)}_{Res}(\tau,\nu)$ and $\tilde{O}^{(2)}_{Res}(\tau,\nu)$ by applying the CLEAN algorithm. Here we let the initial residual response be the matched filter delay-Doppler output responses, i.e., $\tilde{O}^{(0)}_{Res}(\tau,\nu) = \tilde{O}_{MF}(\tau,\nu)$.

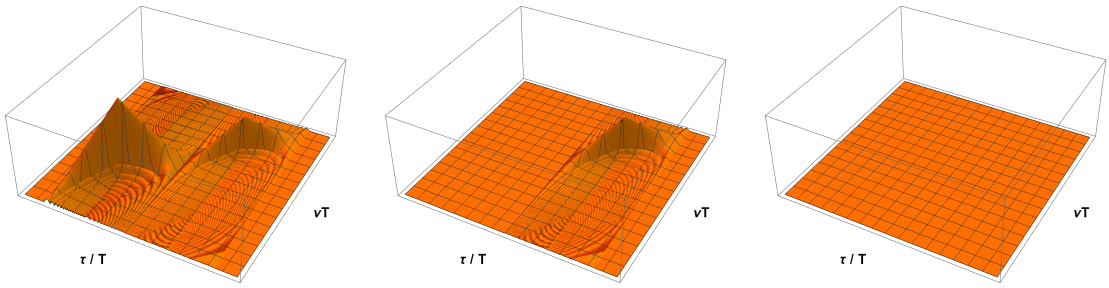

(a) $\tilde{O}^{(0)}_{Res}(\tau,\nu)$ (b) $\tilde{O}^{(1)}_{Res}(\tau,\nu)$ (c) $\tilde{O}^{(2)}_{Res}(\tau,\nu)$

Fig. 3.1. CLEAN Algorithm Residual Responses: No interference case.

Three different degree of interference (no interference, low interference and high interference) are compared. Here we apply a two-target case and without noise for simplicity. We know that when there is no interference (Figure 3.1), the CLEAN algorithm can perfectly estimate each target's delay, Doppler shift and amplitude, and the resulting residual delay-Doppler response is zero everywhere. Then in low interference case (Figure 3.2), the delay-Doppler position of the peak amplitude in the matched filter output response and the residual responses may shift slightly, which will cause the CLEAN algorithm to have small error in each target's delay, Doppler shift and amplitude estimates. In high interference case (Figure 3.3), the interference seriously changes the shape of the delay-Doppler matched filter output response, which will cause an obvious shift in delay and Doppler position of the peak amplitude in the residual responses. Therefore, the CLEAN algorithm may not perform well in this situation.

From the above example, we can see that the CLEAN algorithm may not be a reliable method for target parameter estimate under high interference, especially when the radar illumination environment has multiple targets which are close in delay and Doppler. To achieve more accurate target parameter estimate, we introduce a new approach which can effectively estimate targets' delays (ranges). We call this technique *noise-target fringe analysis*. Also, we combine the CLEAN algorithm with the noise-target fringe analysis approach to further acquire targets' Doppler shifts

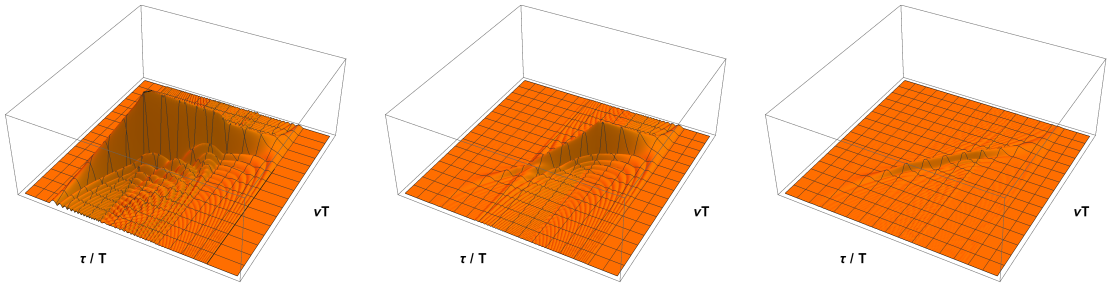

(a) $\tilde{O}^{(0)}_{Res}(\tau,\nu)$ (b) $\tilde{O}^{(1)}_{Res}(\tau,\nu)$ (c) $\tilde{O}^{(2)}_{Res}(\tau,\nu)$

Fig. 3.2. CLEAN Algorithm Residual Responses: Low interference case.

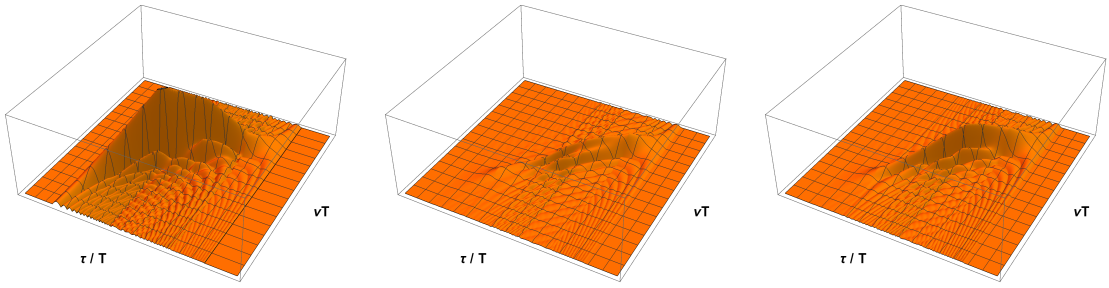

(a) $\tilde{O}^{(0)}_{Res}(\tau,\nu)$ (b) $\tilde{O}^{(1)}_{Res}(\tau,\nu)$ (c) $\tilde{O}^{(2)}_{Res}(\tau,\nu)$

Fig. 3.3. CLEAN Algorithm Residual Responses: High interference case.

(speeds) and intensities (amplitudes) estimates. The complete process is described as follows:

First of all, we initialize the residual response to be the matched filter delay-Doppler output response, i.e., $\tilde{O}^{(0)}_{Res}(\tau,\nu) = \tilde{O}_{MF}(\tau,\nu)$, and we apply the CLEAN algorithm to pick the delay-Doppler position with the largest amplitude from $\tilde{O}^{(0)}_{Res}(\tau,\nu)$, i.e., $(\hat{\tau}_{CLEAN}, \hat{\nu}_{CLEAN}) = \arg\max_{\tau,\nu} \tilde{O}^{(0)}_{Res}(\tau,\nu)$. Then, in the first iteration ($n = 1$), instead of directly subtracting the weighted response of the estimated target $(\hat{\tau}_{CLEAN}, \hat{\nu}_{CLEAN})$, we apply the noise-target fringe analysis to find the edges of the targets' response of the leftmost and the rightmost target. Then we estimate the delays of the leftmost and the rightmost target. After that, we extend the line segment through $(\hat{\tau}_{CLEAN}, \hat{\nu}_{CLEAN})$ and with slope α to intersect the two vertical lines at the estimated delay values from the noise-target fringe analysis respectively. Then the intersected points are the estimated delay-Doppler positions of the leftmost and the rightmost target. We then sequentially subtract the weighted responses of the two estimated target from $\tilde{O}^{(0)}_{Res}(\tau,\nu)$ by comparing their amplitudes in the residual response $\tilde{O}^{(0)}_{Res}(\tau,\nu)$ to get the 1-st residual delay-Doppler output response $\tilde{O}^{(1)}_{Res}(\tau,\nu)$.

Then, in n-th iteration ($n > 1$), we apply the noise-target fringe analysis to $\tilde{O}^{(n-1)}_{Res}(\tau,\nu)$ to find the edges of the targets' response of the leftmost and the rightmost target. Then, just as in the first iteration, we can estimate the delays of the leftmost and the rightmost target, and extend the line segment through $(\hat{\tau}_{CLEAN}, \hat{\nu}_{CLEAN})$ and with slope α to intersect the two vertical lines at the n-th estimated delay values from the noise-target fringe analysis respectively. Then the intersected points are the estimated delay-Doppler positions of the leftmost and the rightmost target in the n-th iteration. Then we sequentially subtract the weighted responses of the two estimated target by comparing their amplitudes in the $(n-1)$-th residual response $\tilde{O}^{(n-1)}_{Res}(\tau,\nu)$ to get the n-th residual delay-Doppler output response $\tilde{O}^{(n)}_{Res}(\tau,\nu)$. This technique considers the targets' amplitude response, the targets' phase response, and the noise response of the matched filter delay-Doppler output. Hence it can enhance the accuracy of targets' delay, Doppler shift and amplitude estimates.

Finally, to further increase the accuracy of target parameter estimates, we apply a weighted non-linear least squares optimization (Gauss-Newton algorithm). The performance results show that this approach can effectively estimate delays, Doppler shifts and intensities of all target returns, and it can easily differentiate close targets which are lying along a line with slope α. Hence, the ability of target discrimination can be further improved.

3.3 Noise-Target Fringe Analysis for Target Delay Estimates

In this section, we present the noise-target fringe analysis approach to effectively estimate targets' delays in chirp radar systems.

3.3.1 Derivation of Chirp Matched Filter Output Response (Phase Response) of Multiple Targets Lying along a Line of Slope α in Delay-Doppler Plane

In this subsection, we derive the chirp matched filter output response of multiple targets lying along the ridge with slope α in delay-Doppler plane.

We assume that there are K targets, specified by (τ_k, ν_k, a_k), where $k = 1, \cdots K$. Here, τ_k is target k's delay, ν_k is target k's Doppler and a_k is target k's amplitude. Then from Equation (3.4), the matched filter output response is

$$\tilde{O}_{\mathrm{MF}}(\tau, \nu) = \sum_{k=1}^{K} a_k e^{-i2\pi(\nu-\nu_k)\tau_k} \chi_s(\tau - \tau_k, \nu - \nu_k).$$

We now consider a chirp waveform

$$s_{Tx}(t) = e^{i\pi\alpha t^2} \cdot 1_{[0,T]}(t).$$

The chirp matched filter output response becomes

$$\begin{aligned}\tilde{O}_{\mathrm{MF}}(\tau, \nu) = \sum_{k=1}^{K} \Big\{ & a_k e^{-i\pi\{(\nu-\nu_k)(\tau+\tau_k)+[(\nu-\nu_k)-\alpha(\tau-\tau_k)]T\}} \cdot (T - |\tau - \tau_k|) \\ & \cdot \operatorname{sinc}\left([(\nu - \nu_k) - \alpha(\tau - \tau_k)]\,(T - |\tau - \tau_k|)\right) \cdot 1_{[0,T]}(|\tau - \tau_k|) \Big\}. \end{aligned} \quad (3.7)$$

Furthermore, we assume that the K true targets lie along the line with slope α in the delay-Doppler plane, i.e.,

$$(\tau_k, \nu_k) = (\tau_1 + \Delta\tau_k, \nu_1 + \alpha\Delta\tau_k), k = 2, \cdots, K, \tag{3.8}$$

so we have

$$(\nu - \nu_k) - \alpha(\tau - \tau_k) = (\nu - \nu_1) - \alpha(\tau - \tau_1), k = 2, \cdots, K. \tag{3.9}$$

With Equation (4.9) and Equation (4.10), we can further simplify Equation (4.8) to

$$\begin{aligned}\tilde{O}_{\mathrm{MF}}(\tau, \nu) =& \sum_{k=1}^{K} \Big\{ a_k \left(T - |\tau - \tau_k|\right) \cdot e^{-i\pi\{(\nu-(\nu_1+\alpha\Delta\tau_k))(\tau+(\tau_1+\Delta\tau_k))+[(\nu-\nu_1)-\alpha(\tau-\tau_1)]T\}} \\ & \cdot \mathrm{sinc}\left([(\nu - \nu_1) - \alpha(\tau - \tau_1)]\left(T - |\tau - \tau_k|\right)\right) \cdot 1_{[0,T]}(|\tau - \tau_k|) \Big\} \\ =& e^{-i\pi[(\nu-\nu_1)-\alpha(\tau-\tau_1)]T} \sum_{k=1}^{K} \Big\{ a_k \left(T - |\tau - \tau_k|\right) e^{-i\pi(\nu-\nu_1-\alpha\Delta\tau_k)(\tau+\tau_1+\Delta\tau_k)} \\ & \cdot \mathrm{sinc}\left([(\nu - \nu_1) - \alpha(\tau - \tau_1)]\left(T - |\tau - \tau_k|\right)\right) \cdot 1_{[0,T]}(|\tau - \tau_k|) \Big\}. \end{aligned} \tag{3.10}$$

Now we observe the delay-Doppler response along the line through a delay-Doppler point $(\hat{\tau}, \hat{\nu})$ and with slope α, i.e., $\tilde{O}_{\mathrm{MF}}(\tau, \alpha\tau + (\hat{\nu} - \alpha\hat{\tau}))$. We first simplify the term $[(\nu - \nu_1) - \alpha(\tau - \tau_1)]$ in Equation (4.12) to

$$[(\alpha\tau + (\hat{\nu} - \alpha\hat{\tau}) - \nu_1) - \alpha(\tau - \tau_1)] = (\hat{\nu} - \nu_1) - \alpha(\hat{\tau} - \tau_1).$$

We also simplify the term $(\nu - \nu_1 - \alpha\Delta\tau_k)(\tau + \tau_1 + \Delta\tau_k)$ in Equation (4.12) to

$$\begin{aligned}(\alpha\tau + (\hat{\nu} - \alpha\hat{\tau}) - \nu_1 - \alpha\Delta\tau_k)(\tau + \tau_1 + \Delta\tau_k) =& \alpha\tau^2 + [(\hat{\nu} - \nu_1) - \alpha(\hat{\tau} - \tau_1)]\tau \\ & + [(\hat{\nu} - \nu_1) - \alpha(\hat{\tau} + \Delta\tau_k)](\tau_1 + \Delta\tau_k).\end{aligned}$$

Then we have

$$
\begin{aligned}
&\tilde{O}_{\mathrm{MF}}(\tau, \alpha\tau + (\hat{\nu} - \alpha\hat{\tau})) \\
=&e^{-i\pi[(\hat{\nu}-\nu_1)-\alpha(\hat{\tau}-\tau_1)]T} \sum_{k=1}^{K} \Big\{ a_k \left(T - |\tau - \tau_k|\right) \cdot e^{-i\pi\left\{\alpha\tau^2 + [(\hat{\nu}-\nu_1)-\alpha(\hat{\tau}-\tau_1)]\tau + [(\hat{\nu}-\nu_1)-\alpha(\hat{\tau}+\Delta\tau_k)](\tau_1+\Delta\tau_k)\right\}} \\
&\cdot \operatorname{sinc}\Big(\left[(\hat{\nu} - \nu_1) - \alpha(\hat{\tau} - \tau_1)\right] \left(T - |\tau - \tau_k|\right)\Big) \cdot 1_{[0,T]}(|\tau - \tau_k|) \Big\} \\
=&e^{-i\pi[(\hat{\nu}-\nu_1)-\alpha(\hat{\tau}-\tau_1)]T} e^{-i\pi\alpha\tau^2} e^{-i\pi[(\hat{\nu}-\nu_1)-\alpha(\hat{\tau}-\tau_1)]\tau} \cdot \sum_{k=1}^{K} \Big\{ e^{-i\pi\{[(\hat{\nu}-\nu_1)-\alpha(\hat{\tau}+\Delta\tau_k)](\tau_1+\Delta\tau_k)\}} \\
&\cdot a_k \left(T - |\tau - \tau_k|\right) \operatorname{sinc}\Big(\left[(\hat{\nu} - \nu_1) - \alpha(\hat{\tau} - \tau_1)\right] \left(T - |\tau - \tau_k|\right)\Big) \cdot 1_{[0,T]}(|\tau - \tau_k|) \Big\} \\
=&e^{-i\pi\alpha\tau^2} e^{-i\pi[(\hat{\nu}-\nu_1)-\alpha(\hat{\tau}-\tau_1)](T+\tau)} \cdot \sum_{k=1}^{K} \Big\{ e^{-i\pi[(\hat{\nu}-\nu_1-\alpha\hat{\tau})\tau_1 + (\hat{\nu}-\nu_1-\alpha\hat{\tau}-\alpha\tau_1-\alpha\Delta\tau_k)\Delta\tau_k]} \\
&\cdot a_k \left(T - |\tau - \tau_k|\right) \operatorname{sinc}\Big(\left[(\hat{\nu} - \nu_1) - \alpha(\hat{\tau} - \tau_1)\right] \left(T - |\tau - \tau_k|\right)\Big) \cdot 1_{[0,T]}(|\tau - \tau_k|) \Big\} \\
=&e^{-i\pi\alpha\tau^2} e^{-i\pi[(\hat{\nu}-\nu_1)-\alpha(\hat{\tau}-\tau_1)](T+\tau)} e^{-i\pi(\hat{\nu}-\nu_1-\alpha\hat{\tau})\tau_1} \cdot \sum_{k=1}^{K} \Big\{ e^{-i\pi[(\hat{\nu}-\nu_1-\alpha\hat{\tau}-\alpha\tau_1-\alpha\Delta\tau_k)\Delta\tau_k]} \\
&\cdot a_k \left(T - |\tau - \tau_k|\right) \operatorname{sinc}\Big(\left[(\hat{\nu} - \nu_1) - \alpha(\hat{\tau} - \tau_1)\right] \left(T - |\tau - \tau_k|\right)\Big) \cdot 1_{[0,T]}(|\tau - \tau_k|) \Big\}.
\end{aligned}
\tag{3.11}
$$

We know that $\Delta\tau_1 = 0$, so for the two-target case, the above equation becomes

$$
\begin{aligned}
&\tilde{O}_{\mathrm{MF}}(\tau, \alpha\tau + (\hat{\nu} - \alpha\hat{\tau})) \\
=&e^{-i\pi\alpha\tau^2} e^{-i\pi[(\hat{\nu}-\nu_1)-\alpha(\hat{\tau}-\tau_1)](T+\tau)} e^{-i\pi(\hat{\nu}-\nu_1-\alpha\hat{\tau})\tau_1} \\
&\cdot \Big(a_1 \left(T - |\tau - \tau_1|\right) \operatorname{sinc}\left(\left[(\hat{\nu} - \nu_1) - \alpha(\hat{\tau} - \tau_1)\right] \left(T - |\tau - \tau_1|\right)\right) \\
&\cdot 1_{[0,T]}(|\tau - \tau_1|) \\
&+ a_2 \left(T - |\tau - \tau_2|\right) \operatorname{sinc}\left(\left[(\hat{\nu} - \nu_1) - \alpha(\hat{\tau} - \tau_1)\right] \left(T - |\tau - \tau_2|\right)\right) \\
&\cdot 1_{[0,T]}(|\tau - \tau_2|) e^{-i\pi[(\hat{\nu}-\nu_1-\alpha\hat{\tau}-\alpha\tau_1-\alpha\Delta\tau_2)\Delta\tau_2]} \Big).
\end{aligned}
\tag{3.12}
$$

In the following, we would like to divide Equation (3.12) into two parts and analyze the phase responses separately. In Figure 3.4, we have the phase variation of the first half of Equation (3.12), i.e.,

$$
e^{-i\pi\alpha\tau^2} e^{-i\pi[(\hat{\nu}-\nu_1)-\alpha(\hat{\tau}-\tau_1)](T+\tau)} e^{-i\pi(\hat{\nu}-\nu_1-\alpha\hat{\tau})\tau_1}, \tag{3.13}
$$

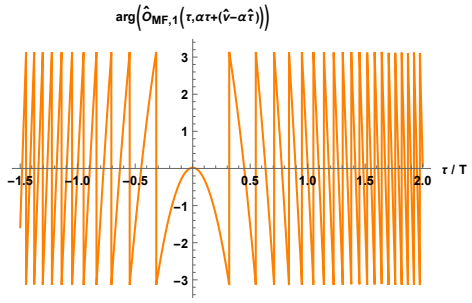

Fig. 3.4. Phase response of Equation (3.13).

which varies rapidly and with frequency $-2\pi\alpha\tau - \pi[(\hat{\nu} - \nu_1) - \alpha(\hat{\tau} - \tau_1)]$.

Also, in Figure 3.5, we have the phase variation of the second half of Equation (3.12), i.e.,

$$\begin{aligned}
&\Big(a_1 \left(T - |\tau - \tau_1|\right) \operatorname{sinc}\left([(\hat{\nu} - \nu_1) - \alpha(\hat{\tau} - \tau_1)]\left(T - |\tau - \tau_1|\right)\right) \\
&\cdot 1_{[0,T]}(|\tau - \tau_1|) \\
&+ a_2 \left(T - |\tau - \tau_2|\right) \operatorname{sinc}\left([(\hat{\nu} - \nu_1) - \alpha(\hat{\tau} - \tau_1)]\left(T - |\tau - \tau_2|\right)\right) \\
&\cdot 1_{[0,T]}(|\tau - \tau_2|) e^{-i\pi[(\hat{\nu} - \nu_1 - \alpha\hat{\tau} - \alpha\tau_1 - \alpha\Delta\tau_2)\Delta\tau_2]}\Big),
\end{aligned} \tag{3.14}$$

which varies very slowly relative to the phase variation of Equation (3.13). In Equation (3.14), we can see that the first term, which relates to the first target, i.e.,

$$\begin{aligned}
&a_1 \left(T - |\tau - \tau_1|\right) \operatorname{sinc}\left([(\hat{\nu} - \nu_1) - \alpha(\hat{\tau} - \tau_1)]\left(T - |\tau - \tau_1|\right)\right) \\
&\cdot 1_{[0,T]}(|\tau - \tau_1|),
\end{aligned}$$

has zero phase. And the second term,

$$\begin{aligned}
&a_2 \left(T - |\tau - \tau_2|\right) \operatorname{sinc}\left([(\hat{\nu} - \nu_1) - \alpha(\hat{\tau} - \tau_1)]\left(T - |\tau - \tau_2|\right)\right) \\
&\cdot 1_{[0,T]}(|\tau - \tau_2|) e^{-i\pi[(\hat{\nu} - \nu_1 - \alpha\hat{\tau} - \alpha\tau_1 - \alpha\Delta\tau_2)\Delta\tau_2]},
\end{aligned}$$

has phase $-\pi[(\hat{\nu} - \nu_1 - \alpha\hat{\tau} - \alpha\tau_1 - \alpha\Delta\tau_2)\Delta\tau_2]$.

Furthermore, it is worth noting that when the chosen observation point $(\hat{\tau}, \hat{\nu})$ is close to the ridge of these targets' responses, $(\hat{\nu} - \nu_1) - \alpha(\hat{\tau} - \tau_1)$ is then very small, which causes the sinc function to have a nearly-flat (slowly-varying) magnitude within

each target's response. Thus, when we apply the CLEAN algorithm to pick the first target's parameters $(\hat{\tau}, \hat{\nu})$, it has a high probability of choosing a point $(\hat{\tau}, \hat{\nu})$ that is close to or right on the ridge, so we have the near-flat (slowly-varying) magnitude for the sinc function.

Therefore, we know from Equation (3.14) that when τ varies, the phase varies between the phase values of the two terms, depending on their slowly-varied amplitudes. As a result, Equation (3.14) shows slow variation in phase with respect to Equation (3.13).

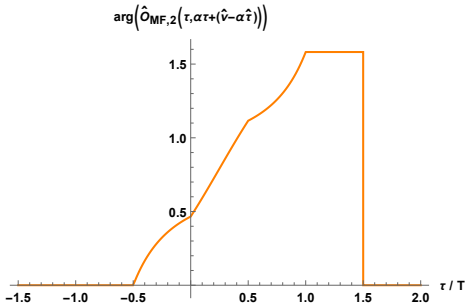

Fig. 3.5. Phase response of Equation (3.14).

Finally, in Figure 3.6, we have the phase variation of Equation (3.12). From

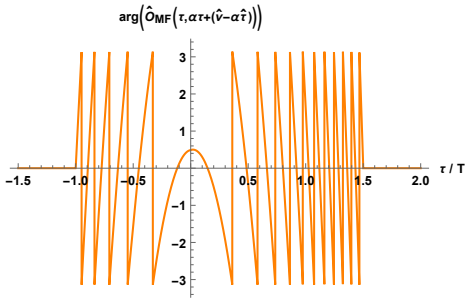

Fig. 3.6. Phase response of Equation (3.12).

these figures, we know that the phase of Equation (3.13), which varies quadratically in τ, dominates the whole phase response of Equation (3.12). Therefore, the phase difference of Equation (3.12) linearly varies in τ.

3.3.2 Correlation Between Two Delay-Doppler Matched Filter Outputs Driven by Noise-Only

In this subsection, we would like to determine how the amplitude and phase of the noise at the matched filter output vary along a line with slope α in the delay-Doppler plane. First of all, we know that the correlation between two delay-Doppler matched filter outputs (τ_1, ν_1), (τ_2, ν_2) driven by noise-only is

$$\begin{aligned} R_{\hat{n}}(\tau_1, \tau_2, \nu_1, \nu_2) &\triangleq E[N(\tau_1, \nu_1)N^*(\tau_2, \nu_2)] \\ &= N_0 e^{-i2\pi(\nu_1-\nu_2)\tau_2}\chi_s(\tau_1-\tau_2, \nu_1-\nu_2). \end{aligned} \tag{3.15}$$

Now, we observe two noise outputs which are along the line with slope α and through the first point (τ_1, ν_1), i.e., $(\tau_2, \nu_2) = (\tau_1 + \Delta\tau, \nu_1 + \alpha\Delta\tau)$, then we have

$$\begin{aligned} R_{\hat{n}}(\tau_1, \tau_1+\Delta\tau, \nu_1, \nu_1+\alpha\Delta\tau) =& N_0 e^{-i2\pi[\nu_1-(\nu_1+\alpha\Delta\tau)](\tau_1+\Delta\tau)} \\ & \cdot \chi_s(\tau_1-(\tau_1+\Delta\tau), \nu_1-(\nu_1+\alpha\Delta\tau)) \\ =& N_0 e^{-i2\pi(-\alpha\Delta\tau)(\tau_1+\Delta\tau)}\chi_s(-\Delta\tau, -\alpha\Delta\tau) \\ =& N_0 e^{i2\pi\alpha\Delta\tau(\tau_1+\Delta\tau)}\chi_s(-\Delta\tau, -\alpha\Delta\tau). \end{aligned}$$

Furthermore, for the chirp waveform, we have

$$\begin{aligned} \chi_s(-\Delta\tau, -\alpha\Delta\tau) =& e^{-i\pi\alpha(-\Delta\tau)^2} e^{-i\pi[-\alpha(\Delta\tau)-\alpha(-\Delta\tau)][T+(-\Delta\tau)]} \cdot (T-|-\Delta\tau|) \\ & \cdot \operatorname{sinc}\left([-\alpha(\Delta\tau)-\alpha(-\Delta\tau)]\,(T-|-\Delta\tau|)\right) \cdot 1_{[0,T]}(|-\Delta\tau|) \\ =& e^{-i\pi\alpha(\Delta\tau)^2}(T-|\Delta\tau|)\operatorname{sinc}(0) \cdot 1_{[0,T]}(|\Delta\tau|) \\ =& e^{-i\pi\alpha(\Delta\tau)^2}(T-|\Delta\tau|) \cdot 1_{[0,T]}(|\Delta\tau|). \end{aligned}$$

So we have the correlation between two noise outputs sampled along the line with slope α as follows:

$$\begin{aligned} R_{\hat{n}}(\tau_1, \tau_1+\Delta\tau, \nu_1, \nu_1+\alpha\Delta\tau) =& N_0 e^{i2\pi\alpha\Delta\tau(\tau_1+\Delta\tau)} e^{-i\pi\alpha(\Delta\tau)^2}(T-|\Delta\tau|) \cdot 1_{[0,T]}(|\Delta\tau|) \\ =& e^{i\pi\alpha(\Delta\tau)^2} e^{i2\pi\alpha\tau_1\Delta\tau} \cdot N_0(T-|\Delta\tau|) \cdot 1_{[0,T]}(|\Delta\tau|) \\ =& e^{i\pi\alpha(\Delta\tau+\tau_1)^2} e^{-i\pi\alpha\tau_1^2} \cdot N_0(T-|\Delta\tau|) \cdot 1_{[0,T]}(|\Delta\tau|). \end{aligned} \tag{3.16}$$

From Equation (3.16), we know that when the sampling interval $\Delta\tau$ is small enough, i.e., $\Delta\tau \approx 0$, then

$$\begin{aligned} R_{\hat{n}}(\tau_1, \tau_1 + \Delta\tau, \nu_1, \nu_1 + \alpha\Delta\tau) =& e^{i\pi\alpha(\Delta\tau+\tau_1)^2} e^{-i\pi\alpha\tau_1^2} \cdot N_0(T - |\Delta\tau|) \cdot 1_{[0,T]}(|\Delta\tau|) \\ \approx& e^{i\pi\alpha(\Delta\tau+\tau_1)^2} e^{-i\pi\alpha\tau_1^2} \cdot N_0 T. \end{aligned} \tag{3.17}$$

Therefore, for any two noise outputs sampled along a line with slope α and that are close enough in delay, the correlation approximately equals to $e^{i\pi\alpha(\Delta\tau+\tau_1)^2} e^{-i\pi\alpha\tau_1^2} \cdot N_0 T$.

Furthermore, from Equation (3.15), we know that the autocorrelation of every delay-Doppler matched filter output driven by noise-only is

$$\begin{aligned} R_{\hat{n}}(\tau_k, \tau_k, \nu_k, \nu_k) &\triangleq E[N(\tau_k, \nu_k) N^*(\tau_k, \nu_k)] \\ &= N_0 e^{-i2\pi(\nu_k - \nu_k)\tau_k} \chi_s(\tau_k - \tau_k, \nu_k - \nu_k) \\ &= N_0 \chi_s(0, 0) \\ &= N_0 T, \ \forall k. \end{aligned}$$

So the correlation coefficient is

$$\begin{aligned} &\rho_{\hat{n}}(\tau_1, \tau_2, \nu_1, \nu_2) = \frac{R_{\hat{n}}(\tau_1, \tau_2, \nu_1, \nu_2)}{\sqrt{R_{\hat{n}}(\tau_1, \tau_1, \nu_1, \nu_1)} \sqrt{R_{\hat{n}}(\tau_2, \tau_2, \nu_2, \nu_2)}} \\ &(\text{let } \tau_2 = \tau_1 + \Delta\tau, \nu_2 = \nu_1 + \alpha\Delta\tau) \\ &= \frac{e^{i\pi\alpha(\Delta\tau+\tau_1)^2} e^{-i\pi\alpha\tau_1^2} \cdot N_0(T - |\Delta\tau|)}{\sqrt{N_0 T} \sqrt{N_0 T}} \\ &\approx \frac{e^{i\pi\alpha(\Delta\tau+\tau_1)^2} e^{-i\pi\alpha\tau_1^2} \cdot N_0 T}{N_0 T} \\ &= e^{i\pi\alpha(\Delta\tau+\tau_1)^2} e^{-i\pi\alpha\tau_1^2}. \end{aligned} \tag{3.18}$$

Equation (3.18) tells us that two sampled noise outputs (along a line with slope α) which are close enough in delay are highly correlated. Furthermore, it also tells us that these noise outputs have approximately the same amplitudes and have a phase rotation angle of $\pi\alpha[(\Delta\tau+\tau_1)^2 - \tau_1^2]$ [50–52]. Hence, within a region of small variations in delay, the sampled noise outputs have close-to-constant amplitude and have phases which quadratically vary in delay τ.

3.3.3 Phase Dominance of Noise-Target Fringe

From Subsection 3.3.1 and 3.3.2, we know that when we observe near the center of a target's matched filter output ridge response, due to the much larger amplitude of the target compared to the amplitude of output noise, the total phase is dominated by the target's phase. On the other hand, when we observe the response which is close to the edge of a target's response, due to nearly the same order of a target's amplitude and the amplitude of output noise, the total phase variation is decided by both target's phase and noise's phase. Finally, when we observe the edge of a target's response, due to the absence of the target's response, the total phase variation is then decided by the output noise only. The above descriptions are shown in Figure 3.7, 3.8 and 3.9.

Furthermore, Figure 3.9 shows the amplitude and phase variations when τ goes toward the edge of a target's response (From Figure 3.9(a) to 3.9(d)). Obviously, we can see that the phase variation of the overall response transforms from target-only phase variation (target-phase dominated) to target-noise-combined phase variation (phase dominance transition) and then to noise-only phase variation (noise-phase dominated). Furthermore, both the phase of target-only and noise-only quadratically vary in delay τ. Therefore, the overall phase variation seems to gradually change from one quadratically-varying phase to another quadratically-varying phase. Thus, the overall phase difference seems like from one linearly-varying phase difference to another linearly-varying phase difference. As a result, an arc shape (non-linearity) occurs in the phase dominance transition region of the phase difference, which is at the edge of a target's response. This is the reason why the arc shape occurs at the edge of a target's response.

3.3.4 The Noise-Target Fringe Analysis Process

From subsection 3.3.3 we know that the phase difference along a ridge line with slope α is linear in τ, which comes from the quadratic phase variations (in delay)

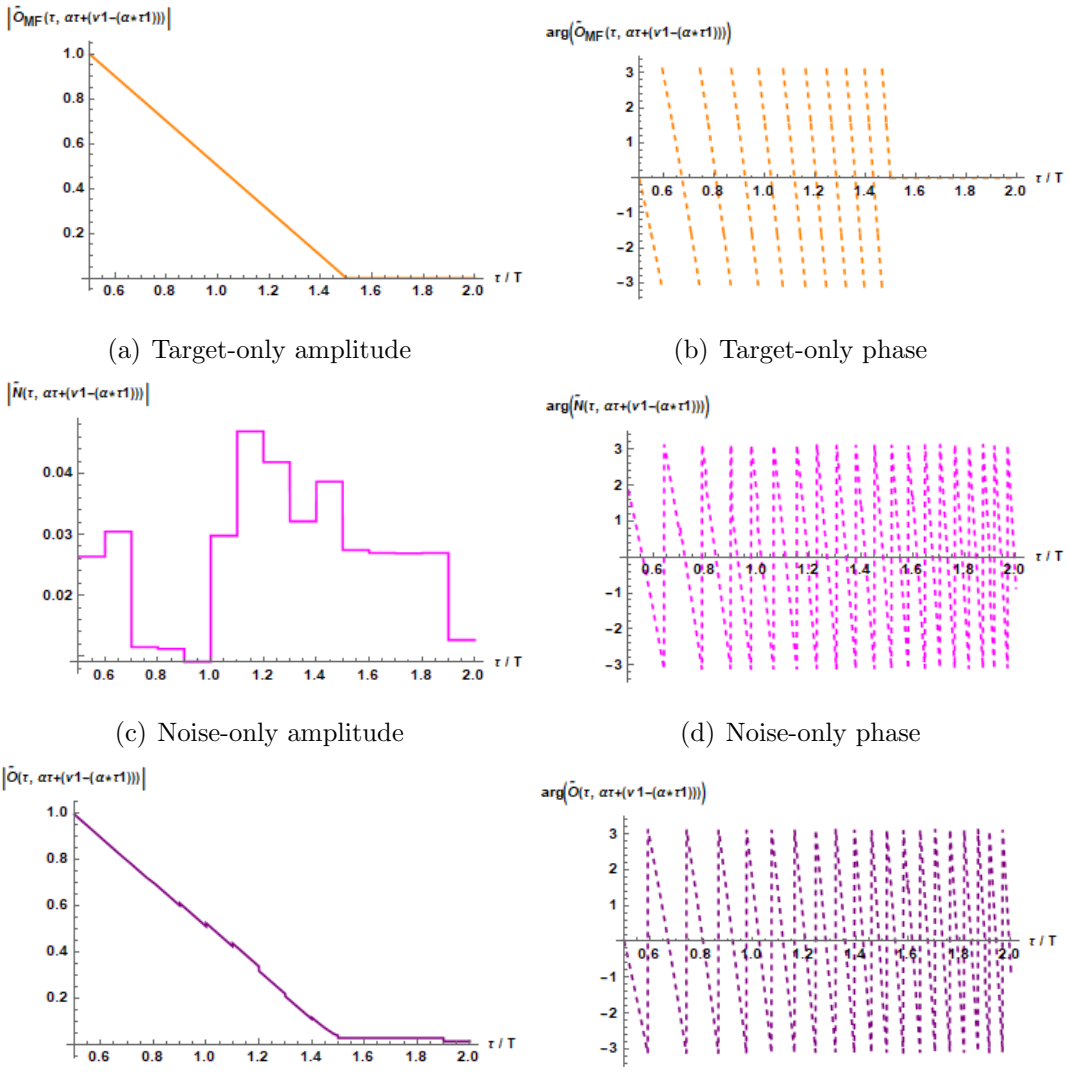

(a) Target-only amplitude

(b) Target-only phase

(c) Noise-only amplitude

(d) Noise-only phase

(e) Overall amplitude

(f) Overall phase

Fig. 3.7. Amplitude response and phase response along the ridge with slope α (30dB SNR).

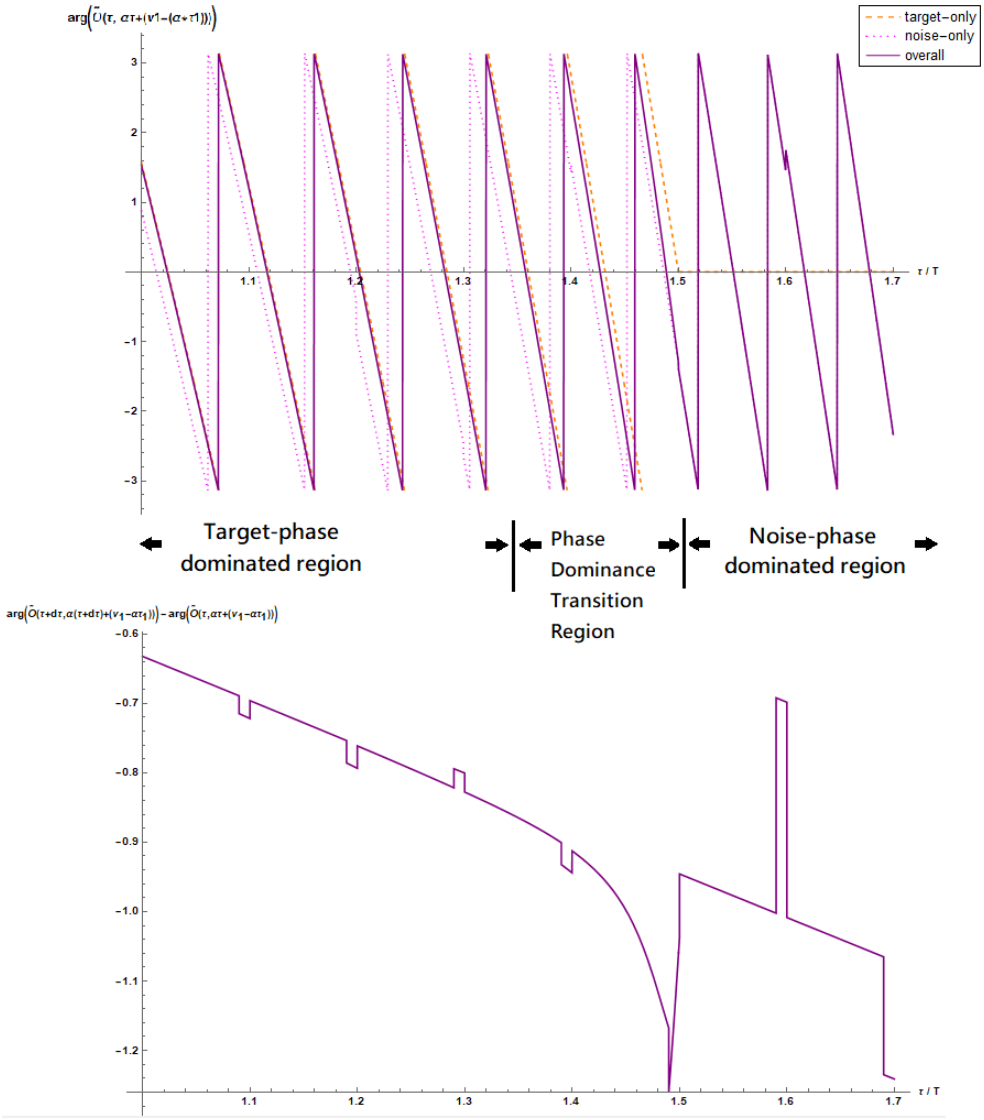

Fig. 3.8. The phase response (upper figure) and the phase difference (lower figure) of the line with slope α and through (τ_1, ν_1).

of the delay-Doppler response along the ridge. However, the phase difference shows a non-linear shape (arc-shape) rather than a linear shape when we are at the edge of a target's response. This is due to the fact that the total amplitude and phase dominance changes from the target to the output noise.

By experimental observation, we know that generally there are four types of arc-shapes which can possibly occur in the phase difference result (Figure 3.10). There-

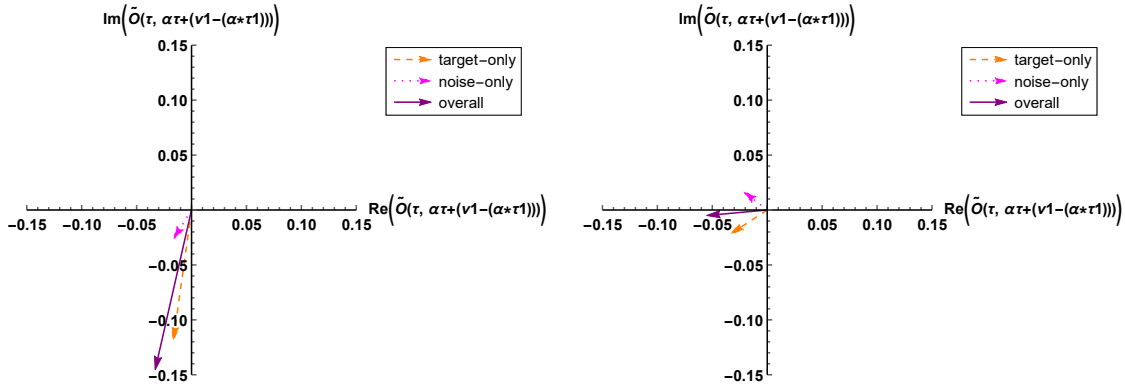

(a) (b)

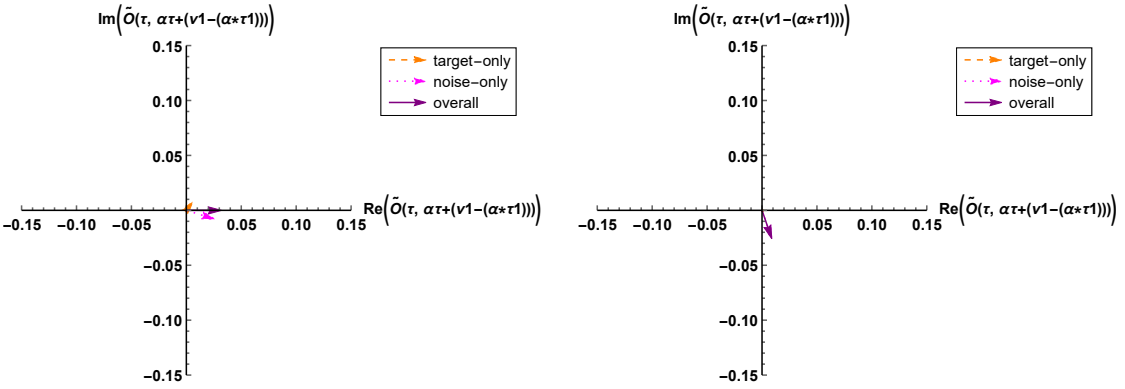

(c) (d)

Fig. 3.9. Amplitude and phase variations from the center to the edge of a target's response (from 3.9(a) to 3.9(d)).

(a) Type 1 (b) Type 2 (c) Type 3 (d) Type 4

Fig. 3.10. Four possible types of arc-shape in the phase difference along the ridge.

fore, to find these arcs in the phase difference results, we would like to sample the phase difference line and detect the consecutively increasing (and decreasing) in slope to recognize as the arc positions.

In the following, we illustrate how the noise-target fringe analysis proceeds, including the arc-shape detection. First of all, we apply the CLEAN algorithm to pick the delay-Doppler position with the largest magnitude from the matched filter output response, say $(\hat{\tau}_{CLEAN}, \hat{\nu}_{CLEAN}, \hat{a}_{CLEAN})$ (one target only). Then we sample the matched filter output response along the line through $(\hat{\tau}_{CLEAN}, \hat{\nu}_{CLEAN})$ and with slope α. For these observation samples, we can easily calculate their phase values, and then we compute the phase difference and check where the arc-shape occurs. The arc-shape detection method is quite simple: we just find the consecutively increasing or decreasing in slope of the phase difference result. In this way, we can find two delay positions with such arc-shape, say $\hat{\tau}_{edge1}$ and $\hat{\tau}_{edge2}$ ($\hat{\tau}_{edge1} < \hat{\tau}_{edge2}$, WLOG), which are situated in the edges of the leftmost and the rightmost of the targets' delay-Doppler response. Hence, we can estimate two targets' delays $\hat{\tau}_{p1} = \hat{\tau}_{edge1} + T$ and $\hat{\tau}_{p2} = \hat{\tau}_{edge2} - T$, where T is the duration of the chirp transmitted waveform.

Furthermore, we know that in moderate or high SNR situations (30dB or more), interference among the targets' responses dominates the whole matched filter delay-Doppler response. And, for chirp radars, a target's matched filter output response

shows the triangular drop in amplitude along the ridge with slope α, and the amplitude response drops quickly along other directions. Therefore, when the targets are lying along a line with slope α, the constructive/destructive interference affects the resulting matched filter output amplitude response, especially the amplitude response along the ridge, which is affected the most. Because of this phenomenon, when the CLEAN algorithm is applied for picking a peak from the chirp matched filter delay-Doppler output response, it usually picks the target parameter with good accuracy (not too far away from the true target parameter), or it picks the parameter (first target) which usually lies in the vicinity of the line connecting to two true targets' in the delay-Doppler plane. Then, with $(\hat{\tau}_{CLEAN}, \hat{\nu}_{CLEAN})$ from CLEAN, and with $\hat{\tau}_{p1}$, $\hat{\tau}_{p2}$ from the phase difference observation, we can estimate the targets' Doppler shifts $\hat{\nu}_{p1} = \hat{\nu}_{CLEAN} + \alpha(\hat{\tau}_{p1} - \hat{\tau}_{CLEAN})$, $\hat{\nu}_{p2} = \hat{\nu}_{CLEAN} + \alpha(\hat{\tau}_{p2} - \hat{\tau}_{CLEAN})$. As for the amplitude estimate of two targets, first we compare the amplitude at the two positions $(\hat{\tau}_{p1}, \hat{\nu}_{p1}, \hat{\tau}_{p2}, \hat{\nu}_{p2})$, say $|\tilde{O}(\hat{\tau}_{p1}, \hat{\nu}_{p1})|$ and $|\tilde{O}(\hat{\tau}_{p2}, \hat{\nu}_{p2})|$, and we pick the larger amplitude to be the first target's amplitude. For example, if $|\tilde{O}(\hat{\tau}_{p1}, \hat{\nu}_{p1})| > |\tilde{O}(\hat{\tau}_{p2}, \hat{\nu}_{p2})|$, then $\hat{a}_{p1} = \tilde{O}(\hat{\tau}_{p1}, \hat{\nu}_{p1})$, and vice versa. So here we have the estimated parameter of first target to be $(\hat{\tau}_{p1}, \hat{\nu}_{p1}, \hat{a}_{p1})$. Then we subtract the output response of the estimated first target from the matched filter delay-Doppler output response to get the residual output response $\tilde{O}^{(1)}_{Res}(\tau, \nu)$ (i.e., subtract the gain of this point source $\hat{a}_{p1}$ convolved with the point spread function of the observation $(\hat{\tau}_{p1}, \hat{\nu}_{p1})$). Finally, we let the amplitude at $(\hat{\tau}_{p2}, \hat{\nu}_{p2})$ of the residual output response be $\hat{a}_{p2}$. Likewise, we subtract the weighted output response of the second estimated target from the residual output response $\tilde{O}^{(1)}_{Res}(\tau, \nu)$ to get the new residual output response $\tilde{O}^{(2)}_{Res}(\tau, \nu)$. In this way, we have the overall estimated parameter $(\hat{\tau}_{p1}, \hat{\nu}_{p1}, \hat{a}_{p1}, \hat{\tau}_{p2}, \hat{\nu}_{p2}, \hat{a}_{p2})$. The above example can be generalized to multiple-target cases, and we can iteratively apply the above approach to sequentially estimate all targets parameters (from the two sides to the middle).

3.3.5 A Further Note on Noise-Target Fringe Analysis

In previous sections we observe the delay-Doppler response along the line which goes through $(\hat{\tau}_{CLEAN}, \hat{\nu}_{CLEAN})$ and is with slope α. Actually, we know that no matter which delay-Doppler point (τ_k, ν_k) is chosen, if (τ_k, ν_k) is close to one of the true targets or lies in the vicinity of the line connecting the two true targets, the triangular shape of the targets' amplitude responses still holds, so we still can find the arc-shape in the phase difference of the observations. Therefore, once we have $(\hat{\tau}_{CLEAN}, \hat{\nu}_{CLEAN})$, we can not only sample along the line through $(\hat{\tau}_{CLEAN}, \hat{\nu}_{CLEAN})$ but also sample along other lines through $(\hat{\tau}_{CLEAN} \pm \Delta\tau, \hat{\nu}_{CLEAN} \pm \Delta\nu)$ to generate different ridge samples, where $\pm\Delta\tau$ and $\pm\Delta\nu$ are small bias values (small random real numbers). In this way, we can find the arc-shape positions from the phase difference of these ridge lines to further confirm the two targets' delays.

3.4 Weighted Nonlinear Least Squares Optimization for Target Parameter Estimates

In this section, we treat the matched filter delay-Doppler output response as a two-dimensional equation, and we apply the Gauss-Newton optimizations to acquire the weighted nonlinear least squares estimate of the unknown target parameters. First, we sample at different delay-Doppler grid points from the matched filter output response $\tilde{O}(\tau, \nu)$ to get a sequence of N observations $\tilde{O}(\tau_{(1)}, \nu_{(1)}), \tilde{O}(\tau_{(2)}, \nu_{(2)}), \cdots, \tilde{O}(\tau_{(N)}, \nu_{(N)})$, where $(\tau_{(p)}, \nu_{(p)})$ is the delay-Doppler position of the p-th observed grid point, $p = 1, \cdots, N$. In the following we use $\mathbb{X} = [X_1, X_2, \cdots, X_N]^T$ to represent the

observations $[\tilde{O}(\tau_{(1)},\nu_{(1)}),\cdots,\ \tilde{O}(\tau_{(N)},\nu_{(N)})]^T$, for brevity. Then we have the mean of the observations

$$\begin{aligned}E[\mathbb{X}] =&[E[X_1],E[X_2],\cdots,E[X_N]]^T\\ =&\Bigg[\sum_{k=1}^{K}a_k e^{-i2\pi(\nu_{(1)}-\nu_k)\tau_k}\chi_s(\tau_{(1)}-\tau_k,\nu_{(1)}-\nu_k),\\ &\cdots,\\ &\sum_{k=1}^{K}a_k e^{-i2\pi(\nu_{(N)}-\nu_k)\tau_k}\chi_s(\tau_{(N)}-\tau_k,\nu_{(N)}-\nu_k)\Bigg]^T,\end{aligned}\tag{3.19}$$

which is due to the fact that $E[N(\tau_{(p)},\nu_{(p)})]=0,\ p=1,\cdots,N$. Furthermore, the covariance of any two observations X_p and X_q is

$$\begin{aligned}C_{X_pX_q}&=E[(X_p-E[X_p])(X_q-E[X_q])^*]\\ &=E[N(\tau_{(p)},\nu_{(p)})(N(\tau_{(q)},\nu_{(q)}))^*]\\ &=N_0e^{-i2\pi(\nu_{(p)}-\nu_{(q)})\tau_{(q)}}\chi_s(\tau_{(p)}-\tau_{(q)},\nu_{(p)}-\nu_{(q)}).\end{aligned}\tag{3.20}$$

It is worth noting that none of the elements of the covariance matrix $C_{\mathbb{XX}}$ depend on $\underline{\theta}$, the vector containing all unknown target parameter elements. Hence, the joint probability density function of the observations is

$$f(\mathbb{X};\underline{\theta})=\frac{1}{\sqrt{(2\pi)^N|C_{\mathbb{XX}}|}}e^{-\frac{1}{2}(\mathbb{X}-E[\mathbb{X}])^HC_{\mathbb{XX}}^{-1}(\mathbb{X}-E[\mathbb{X}])},$$

which has the same form as the likelihood function $L_{\mathbb{X}}(\underline{\theta})$.

Now, given these observations, we would like to find the maximum likelihood estimate $\hat{\underline{\theta}}_{ML}$, which maximizes the likelihood function $L_{\mathbb{X}}(\underline{\theta})$, i.e.,

$$\hat{\underline{\theta}}_{ML}=\arg\max_{\underline{\theta}}\frac{1}{\sqrt{(2\pi)^N|C_{\mathbb{XX}}|}}e^{-\frac{1}{2}(\mathbb{X}-f(\underline{\theta}))^HC_{\mathbb{XX}}^{-1}(\mathbb{X}-f(\underline{\theta}))},$$

where $\hat{\underline{\theta}}_{ML}=(\hat{\tau}_{ML1},\hat{\nu}_{ML1},\hat{a}_{ML1},\cdots,\hat{\tau}_{MLK},\hat{\nu}_{MLK},\hat{a}_{MLK})$ and $f(\underline{\theta})=E[\mathbb{X}]$. Now, because $C_{\mathbb{XX}}$ does not depend on the targets' delay-Doppler positions and amplitudes, i.e., $C_{\mathbb{XX}}$ is not a function of $\underline{\theta}$, and the log function is monotonically increasing, we can rewrite the above equation as the following

$$\hat{\underline{\theta}}_{ML}=\arg\min_{\underline{\theta}}\frac{1}{2}(\mathbb{X}-f(\underline{\theta}))^HC_{\mathbb{XX}}^{-1}(\mathbb{X}-f(\underline{\theta})).\tag{3.21}$$

3.4.1 Hermitian Property of Covariance Matrix $C_{\mathbb{XX}}$

From (3.20) we know that the covariance of two observations X_p and X_q is

$$C_{X_pX_q} = N_0 e^{-i2\pi(\nu_{(p)}-\nu_{(q)})\tau_{(q)}} \chi_s(\tau_{(p)} - \tau_{(q)}, \nu_{(p)} - \nu_{(q)}).$$

Also, the covariance of X_q and X_p is

$$\begin{aligned} C_{X_qX_p} &= E[(X_q - E[X_q])(X_p - E[X_p])^*] \\ &= E[N(\tau_{(q)}, \nu_{(q)})(N(\tau_{(p)}, \nu_{(p)}))^*] \\ &= N_0 e^{-i2\pi(\nu_{(q)}-\nu_{(p)})\tau_{(p)}} \chi_s(\tau_{(q)} - \tau_{(p)}, \nu_{(q)} - \nu_{(p)}). \end{aligned}$$

From the properties of the ambiguity function, we know that

$$\chi_s(\tau_{(q)} - \tau_{(p)}, \nu_{(q)} - \nu_{(p)}) = e^{-i2\pi(\nu_{(p)}-\nu_{(q)})(\tau_{(p)}-\tau_{(q)})} \chi_s^*(\tau_{(p)} - \tau_{(q)}, \nu_{(p)} - \nu_{(q)}),$$

then we can rewrite $C_{X_qX_p}$ as

$$\begin{aligned} C_{X_qX_p} =& N_0 e^{-i2\pi(\nu_{(q)}-\nu_{(p)})\tau_{(p)}} e^{-i2\pi(\nu_{(p)}-\nu_{(q)})(\tau_{(p)}-\tau_{(q)})} \chi_s^*(\tau_{(p)} - \tau_{(q)}, \nu_{(p)} - \nu_{(q)}) \\ =& N_0 e^{i2\pi(\nu_{(p)}-\nu_{(q)})\tau_{(q)}} \chi_s^*(\tau_{(p)} - \tau_{(q)}, \nu_{(p)} - \nu_{(q)}) \\ =& C_{X_pX_q}^*. \end{aligned}$$

As for the diagonal elements, where $p = q$,

$$\begin{aligned} C_{X_pX_p} &= E[(X_p - E[X_p])(X_p - E[X_p])^*] \\ &= N_0 e^{-i2\pi(\nu_{(p)}-\nu_{(p)})\tau_{(p)}} \chi_s(\tau_{(p)} - \tau_{(p)}, \nu_{(p)} - \nu_{(p)}) \\ &= N_0 \chi_s(0,0) \\ &= N_0 \int_{-\infty}^{\infty} s_{Tx}(t) s_{Tx}^*(t) dt \\ &= N_0 \int_{-\infty}^{\infty} |s_{Tx}(t)|^2 dt, \end{aligned}$$

which are real numbers when $s_{Tx}(t)$ is absolutely integrable. Therefore, the matrix $C_{\mathbb{XX}}$ is a Hermitian matrix.

3.4.2 Eigen-Decomposition of Hermitian Covariance Matrix $C_{\mathbb{X}\mathbb{X}}$

From Subsection 3.4.1 we know that $C_{\mathbb{X}\mathbb{X}}$ is a Hermitian matrix, so we can decompose $C_{\mathbb{X}\mathbb{X}}$ into

$$\begin{aligned} C_{\mathbb{X}\mathbb{X}} &= \underline{V}^H \underline{D} \underline{V} \\ &= \underline{V}^H \underline{D}^{\frac{1}{2}} \underline{D}^{\frac{1}{2}} \underline{V} \\ &= \underline{V}^H \underline{D}^{\frac{H}{2}} \underline{D}^{\frac{1}{2}} \underline{V} \\ &= (\underline{D}^{\frac{1}{2}} \underline{V})^H \underline{D}^{\frac{1}{2}} \underline{V}, \end{aligned} \tag{3.22}$$

where $\underline{D}$ is a diagonal matrix with real diagonal elements, and $\underline{V}$ is the matrix combined by the eigenvectors of $C_{\mathbb{X}\mathbb{X}}$ [53]. Note that $\underline{V}$ is a unitary matrix, i.e., $\underline{V}^H \underline{V} = I$, identity matrix. Then the maximum likelihood estimate becomes

$$\begin{aligned} \underline{\hat{\theta}}_{ML} &= \arg\min_{\underline{\theta}} \frac{1}{2} (\mathbb{X} - f(\underline{\theta}))^H C_{\mathbb{X}\mathbb{X}}^{-1} (\mathbb{X} - f(\underline{\theta})) \\ &= \arg\min_{\underline{\theta}} \frac{1}{2} (\mathbb{X} - f(\underline{\theta}))^H \left(\underline{V}^H \underline{D} \underline{V}\right)^{-1} (\mathbb{X} - f(\underline{\theta})) \\ &= \arg\min_{\underline{\theta}} \frac{1}{2} (\mathbb{X} - f(\underline{\theta}))^H \underline{V}^{-1} \underline{D}^{-1} \left(\underline{V}^H\right)^{-1} (\mathbb{X} - f(\underline{\theta})) \\ &= \arg\min_{\underline{\theta}} \frac{1}{2} (\mathbb{X} - f(\underline{\theta}))^H \underline{V}^H \left(\underline{D}^{-\frac{1}{2}}\right)^H \underline{D}^{-\frac{1}{2}} \underline{V} (\mathbb{X} - f(\underline{\theta})) \\ &= \arg\min_{\underline{\theta}} \frac{1}{2} \left(\underline{D}^{-\frac{1}{2}} \underline{V} (\mathbb{X} - f(\underline{\theta}))\right)^H \left(\underline{D}^{-\frac{1}{2}} \underline{V} (\mathbb{X} - f(\underline{\theta}))\right), \end{aligned} \tag{3.23}$$

which is a complex-valued nonlinear least squares problem [42]. Hence, now we can reformulate the above problem as

$$\underline{\hat{\theta}}_{ML} = \arg\min_{\underline{\theta}} \frac{1}{2} \underline{r}(\underline{\theta})^H \underline{r}(\underline{\theta}),$$

where

$$\underline{r}(\underline{\theta}) = \underline{D}^{-\frac{1}{2}} \underline{V} (\mathbb{X} - f(\underline{\theta})),$$

and $l(\underline{\theta}) = 1/2 \cdot \underline{r}(\underline{\theta})^H \underline{r}(\underline{\theta})$ is a real-valued cost function. In subsections 3.4.3 and 3.4.4, we will apply the Gauss-Newton optimization to solve this complex-valued nonlinear least squares problem and find the weighted nonlinear least squares parameter estimates.

3.4.3 Gradient of Cost Function $l(\underline{\theta})$

Now let $\underline{g}(\underline{\theta})$= gradient of $l(\underline{\theta})$, which is still real-valued. Then

$$
\begin{aligned}
\underline{g}(\underline{\theta}) &= \frac{\partial l(\underline{\theta})}{\partial \underline{\theta}} \\
&= \begin{bmatrix} \frac{\partial l(\underline{\theta})}{\partial \theta_1} \\ \frac{\partial l(\underline{\theta})}{\partial \theta_2} \\ \cdot \\ \cdot \\ \cdot \\ \frac{\partial l(\underline{\theta})}{\partial \theta_M} \end{bmatrix} \\
&= \begin{bmatrix} \frac{\partial \left(\underline{r}(\underline{\theta})^H \underline{r}(\underline{\theta})\right)}{\partial \theta_1} \\ \frac{\partial \left(\underline{r}(\underline{\theta})^H \underline{r}(\underline{\theta})\right)}{\partial \theta_2} \\ \cdot \\ \cdot \\ \cdot \\ \frac{\partial \left(\underline{r}(\underline{\theta})^H \underline{r}(\underline{\theta})\right)}{\partial \theta_M} \end{bmatrix} \\
&= \begin{bmatrix} \left(\frac{\partial}{\partial \theta_1}\underline{r}(\underline{\theta})^H\right)\underline{r}(\underline{\theta}) + \underline{r}(\underline{\theta})^H\left(\frac{\partial}{\partial \theta_1}\underline{r}(\underline{\theta})\right) \\ \left(\frac{\partial}{\partial \theta_2}\underline{r}(\underline{\theta})^H\right)\underline{r}(\underline{\theta}) + \underline{r}(\underline{\theta})^H\left(\frac{\partial}{\partial \theta_2}\underline{r}(\underline{\theta})\right) \\ \cdot \\ \cdot \\ \cdot \\ \left(\frac{\partial}{\partial \theta_M}\underline{r}(\underline{\theta})^H\right)\underline{r}(\underline{\theta}) + \underline{r}(\underline{\theta})^H\left(\frac{\partial}{\partial \theta_M}\underline{r}(\underline{\theta})\right) \end{bmatrix} \\
&= \begin{bmatrix} \left(\frac{\partial}{\partial \theta_1}\underline{r}(\underline{\theta})^H\right)\underline{r}(\underline{\theta}) + \left(\left(\frac{\partial}{\partial \theta_1}\underline{r}(\underline{\theta})^H\right)\underline{r}(\underline{\theta})\right)^* \\ \left(\frac{\partial}{\partial \theta_2}\underline{r}(\underline{\theta})^H\right)\underline{r}(\underline{\theta}) + \left(\left(\frac{\partial}{\partial \theta_2}\underline{r}(\underline{\theta})^H\right)\underline{r}(\underline{\theta})\right)^* \\ \cdot \\ \cdot \\ \cdot \\ \left(\frac{\partial}{\partial \theta_M}\underline{r}(\underline{\theta})^H\right)\underline{r}(\underline{\theta}) + \left(\left(\frac{\partial}{\partial \theta_M}\underline{r}(\underline{\theta})^H\right)\underline{r}(\underline{\theta})\right)^* \end{bmatrix}
\end{aligned}
$$

$$= \begin{bmatrix} 2\mathrm{Re}\left(\left(\frac{\partial}{\partial\theta_1}\underline{r}(\underline{\theta})^H\right)\underline{r}(\underline{\theta})\right) \\ 2\mathrm{Re}\left(\left(\frac{\partial}{\partial\theta_2}\underline{r}(\underline{\theta})^H\right)\underline{r}(\underline{\theta})\right) \\ \cdot \\ \cdot \\ \cdot \\ 2\mathrm{Re}\left(\left(\frac{\partial}{\partial\theta_M}\underline{r}(\underline{\theta})^H\right)\underline{r}(\underline{\theta})\right) \end{bmatrix}$$

$$= 2\mathrm{Re}\left\{\left(\frac{\partial}{\partial\underline{\theta}}\underline{r}(\underline{\theta})^H\right)\underline{r}(\underline{\theta})\right\}. \tag{3.24}$$

3.4.4 Hessian Matrix of Cost Function $l(\underline{\theta})$

Now let $H(\underline{\theta})$= Hessian of $l(\underline{\theta})$, which is a real-valued matrix. Then

$$\begin{aligned} H(\underline{\theta}) &= \frac{\partial^2 l(\underline{\theta})}{\partial\underline{\theta}\partial\underline{\theta}^T} \\ &= 2\mathrm{Re}\left(\underline{J}^H\underline{J}\right) + 2\left(\sum_{m=1}^{M} r_m^* \frac{\partial^2 r_m}{\partial\underline{\theta}\partial\underline{\theta}^T}\right) \\ &\cong 2\mathrm{Re}\left(\underline{J}^H\underline{J}\right), \end{aligned} \tag{3.25}$$

where

$$\underline{J} = \frac{\partial\underline{r}(\underline{\theta})}{\partial\underline{\theta}}.$$

(Since $\underline{r}$ is being minimized in the least squares sense, it is often the case that all components r_m are small). Then, by using the Gauss-Newton method, in the n-th iteration we have the following steps,

(a) Solve $H(\underline{\theta}^{(n)}) \cdot \underline{d}^{(n)} = -\underline{g}(\underline{\theta}^{(n)})$ to get $\underline{d}^{(n)}$.

(b) Update $\underline{\theta}^{(n+1)} = \underline{\theta}^{(n)} + \underline{d}^{(n)}$.

3.4.5 Maximum Likelihood Estimate of Unknown Target Parameters

From Subsection 3.4.2, we can view the maximum likelihood estimate of the targets' parameters as solving the complex-valued nonlinear least squares problem,

$$\hat{\underline{\theta}}_{ML} = \arg\min_{\underline{\theta}} \frac{1}{2}\underline{r}(\underline{\theta})^H \underline{r}(\underline{\theta}),$$

where

$$\underline{r}(\underline{\theta}) = \underline{D}^{-\frac{1}{2}}\underline{V}(\mathbb{X} - f(\underline{\theta})).$$

First, we have

$$\begin{aligned}
\underline{g}(\underline{\theta}) &= 2\mathrm{Re}\left\{\left(\frac{\partial}{\partial\underline{\theta}}\underline{r}(\underline{\theta})^H\right)\underline{r}(\underline{\theta})\right\} \\
&= 2\mathrm{Re}\left\{\left(\frac{\partial}{\partial\underline{\theta}}\left[\underline{D}^{-\frac{1}{2}}\underline{V}(\mathbb{X} - f(\underline{\theta}))\right]^H\right)\cdot\underline{D}^{-\frac{1}{2}}\underline{V}(\mathbb{X} - f(\underline{\theta}))\right\} \\
&= 2\mathrm{Re}\left\{\frac{\partial}{\partial\underline{\theta}}\left[(\mathbb{X} - f(\underline{\theta}))^H\underline{V}^H\underline{D}^{-\frac{H}{2}}\right]\cdot\underline{D}^{-\frac{1}{2}}\underline{V}(\mathbb{X} - f(\underline{\theta}))\right\} \\
&= 2\mathrm{Re}\left\{-\left(\frac{\partial}{\partial\underline{\theta}}f(\underline{\theta})^H\right)\underline{V}^H\underline{D}^{-\frac{1}{2}}\underline{D}^{-\frac{1}{2}}\underline{V}(\mathbb{X} - f(\underline{\theta}))\right\} \\
&= 2\mathrm{Re}\left\{-\left(\frac{\partial}{\partial\underline{\theta}}f(\underline{\theta})^H\right)\underline{V}^H\underline{D}^{-1}\underline{V}(\mathbb{X} - f(\underline{\theta}))\right\} \\
&= 2\mathrm{Re}\left\{-\left(\frac{\partial}{\partial\underline{\theta}}f(\underline{\theta})^H\right)C_{\mathbb{X}\mathbb{X}}^{-1}(\mathbb{X} - f(\underline{\theta}))\right\},
\end{aligned} \tag{3.26}$$

and

$$\begin{aligned}
H(\underline{\theta}) &\cong 2\mathrm{Re}\left\{\underline{J}^H\underline{J}\right\} \\
&= 2\mathrm{Re}\left\{\left(\frac{\partial}{\partial\underline{\theta}}\left[\underline{D}^{-\frac{1}{2}}\underline{V}(\mathbb{X} - f(\underline{\theta}))\right]^H\right)\cdot\left(\frac{\partial}{\partial\underline{\theta}}\left[\underline{D}^{-\frac{1}{2}}\underline{V}(\mathbb{X} - f(\underline{\theta}))\right]\right)\right\} \\
&= 2\mathrm{Re}\left\{\left(\frac{\partial}{\partial\underline{\theta}}\left[(\mathbb{X} - f(\underline{\theta}))^H\underline{V}^H\underline{D}^{-\frac{H}{2}}\right]\right)\cdot\underline{D}^{-\frac{1}{2}}\underline{V}\left(-\frac{\partial}{\partial\underline{\theta}}f(\underline{\theta})\right)\right\} \\
&= 2\mathrm{Re}\left\{\left(-\frac{\partial}{\partial\underline{\theta}}f(\underline{\theta})^H\right)\underline{V}^H\underline{D}^{-\frac{1}{2}}\underline{D}^{-\frac{1}{2}}\underline{V}\left(-\frac{\partial}{\partial\underline{\theta}}f(\underline{\theta})\right)\right\} \\
&= 2\mathrm{Re}\left\{\left(-\frac{\partial}{\partial\underline{\theta}}f(\underline{\theta})^H\right)\underline{V}^H\underline{D}^{-1}\underline{V}\left(-\frac{\partial}{\partial\underline{\theta}}f(\underline{\theta})\right)\right\} \\
&= 2\mathrm{Re}\left\{\left(\frac{\partial}{\partial\underline{\theta}}f(\underline{\theta})^H\right)C_{\mathbb{X}\mathbb{X}}^{-1}\left(\frac{\partial}{\partial\underline{\theta}}f(\underline{\theta})\right)\right\}
\end{aligned} \tag{3.27}$$

Hence, the procedure for finding $\hat{\underline{\theta}}_{ML}$ is

$$\begin{aligned}
&\text{(a) Solve } H(\underline{\theta}^{(n)}) \cdot \underline{d}^{(n)} = -\underline{g}(\underline{\theta}^{(n)}) \text{ to get } \underline{d}^{(n)}, \text{ i.e., solve} \\
&\quad 2\mathrm{Re}\left\{ \left(\frac{\partial}{\partial \underline{\theta}} f(\underline{\theta})^H \right) C_{\mathbb{X}\mathbb{X}}^{-1} \left(\frac{\partial}{\partial \underline{\theta}} f(\underline{\theta}) \right) \right\} \Big|_{\underline{\theta}=\underline{\theta}^{(n)}} \cdot \underline{d}^{(n)} \\
&\quad = -2\mathrm{Re}\left\{ - \left(\frac{\partial}{\partial \underline{\theta}} f(\underline{\theta})^H \right) C_{\mathbb{X}\mathbb{X}}^{-1} (\mathbb{X} - f(\underline{\theta})) \right\} \Big|_{\underline{\theta}=\underline{\theta}^{(n)}}. \\
&\text{(b) Update } \underline{\theta}^{(n+1)} = \underline{\theta}^{(n)} + \underline{d}^{(n)}.
\end{aligned} \tag{3.28}$$

The initial parameter vector $\underline{\theta}^{(0)}$ can be acquired from the result of the noise-target fringe analysis, which generally provides the close-to-the-truth target estimates.

3.4.6 Chirp Radar Systems

Now we apply the chirp waveforms in the radar system, i.e., $s_{Tx}(t) = e^{i\pi\alpha t^2} \cdot 1_{[0,T]}(t)$, and we would like to find the gradient vector $\underline{g}(\underline{\theta})$ and the Hessian matrix $H(\underline{\theta})$. By (3.28), once we know $\partial f(\underline{\theta})/\partial\underline{\theta}$, we can then solve the problem and find the weighted nonlinear least squares estimates of unknown target parameters. The followings are the partial derivatives of $f(\underline{\theta})$ with respect to unknown parameters τ_k, ν_k and a_k, where $k = 1, \cdots, K$.

$$\begin{aligned}\frac{\partial}{\partial\tau_k}f(\underline{\theta}) =&\frac{\partial}{\partial\tau_k}\left(\sum_{k=1}^{K}a_k e^{-i2\pi(\nu-\nu_k)\tau_k}\chi_s(\tau-\tau_k,\nu-\nu_k)\right)\\ =&a_k e^{-i\pi[(\nu-\nu_k)(T+\tau+\tau_k)-\alpha T(\tau-\tau_k)]}\cdot 1_{[0,T]}(|\tau-\tau_k|)\\ &\cdot\Bigg\{\left(-i\pi[\nu-\nu_k+\alpha T]\right)\left(T-|\tau-\tau_k|\right)\\ &\cdot\operatorname{sinc}\left(\left[(\nu-\nu_k)-\alpha(\tau-\tau_k)\right]\left[T-|\tau-\tau_k|\right]\right)\\ &+\Bigg\{\pm\operatorname{sinc}\left(\left[(\nu-\nu_k)-\alpha(\tau-\tau_k)\right]\left[T-|\tau-\tau_k|\right]\right)\\ &+\left(T-|\tau-\tau_k|\right)\cdot\Bigg[\frac{1}{\pi}\left[\alpha T\pm\left((\nu-\nu_k)-2\alpha(\tau-\tau_k)\right)\right]\\ &\cdot\Bigg[\frac{\pi\cos\left(\pi\left[(\nu-\nu_k)-\alpha(\tau-\tau_k)\right]\left[T-|\tau-\tau_k|\right]\right)}{\left[(\nu-\nu_k)-\alpha(\tau-\tau_k)\right]\left[T-|\tau-\tau_k|\right]}\\ &-\frac{\sin\left(\pi\left[(\nu-\nu_k)-\alpha(\tau-\tau_k)\right]\left[T-|\tau-\tau_k|\right]\right)}{\left(\left[(\nu-\nu_k)-\alpha(\tau-\tau_k)\right]\left[T-|\tau-\tau_k|\right]\right)^2}\Bigg]\Bigg]\Bigg\}\Bigg\},\end{aligned}$$

$$\begin{aligned}\frac{\partial}{\partial\nu_k}f(\underline{\theta}) =&\frac{\partial}{\partial\nu_k}\left(\sum_{k=1}^{K}a_k e^{-i2\pi(\nu-\nu_k)\tau_k}\chi_s(\tau-\tau_k,\nu-\nu_k)\right)\\ =&a_k\left(T-|\tau-\tau_k|\right)e^{-i\pi[(\nu-\nu_k)(T+\tau+\tau_k)-\alpha T(\tau-\tau_k)]}\\ &\cdot 1_{[0,T]}(|\tau-\tau_k|)\cdot\Bigg\{i\pi(T+\tau+\tau_k)\\ &\cdot\operatorname{sinc}\left(\left[(\nu-\nu_k)-\alpha(\tau-\tau_k)\right]\left[T-|\tau-\tau_k|\right]\right)\\ &+\frac{\left(|\tau-\tau_k|-T\right)}{\pi}\\ &\cdot\Bigg[\frac{\pi\cos\left(\pi\left[(\nu-\nu_k)-\alpha(\tau-\tau_k)\right]\left[T-|\tau-\tau_k|\right]\right)}{\left[(\nu-\nu_k)-\alpha(\tau-\tau_k)\right]\left[T-|\tau-\tau_k|\right]}\\ &-\frac{\sin\left(\pi\left[(\nu-\nu_k)-\alpha(\tau-\tau_k)\right]\left[T-|\tau-\tau_k|\right]\right)}{\left(\left[(\nu-\nu_k)-\alpha(\tau-\tau_k)\right]\left[T-|\tau-\tau_k|\right]\right)^2}\Bigg]\Bigg\},\end{aligned}$$

and

$$\begin{aligned}\frac{\partial}{\partial a_k} f(\underline{\theta}) =& \frac{\partial}{\partial a_k}\left(\sum_{k=1}^{K} a_k e^{-i2\pi(\nu-\nu_k)\tau_k}\chi_s(\tau-\tau_k,\nu-\nu_k)\right)\\ =& e^{-i\pi[(\nu-\nu_k)(T+\tau+\tau_k)-\alpha T(\tau-\tau_k)]}\cdot(T-|\tau-\tau_k|)\\ &\cdot \operatorname{sinc}\left([(\nu-\nu_k)-\alpha(\tau-\tau_k)]\,(T-|\tau-\tau_k|)\right)\\ &\cdot 1_{[0,T]}(|\tau-\tau_k|).\end{aligned}$$

3.5 Signal to Noise Ratio Analysis

In this section, we focus on digital radar systems, and we show the derivations of the first and second order statistics such as mean and variance of the delay-Doppler matched filter output driven by complex additive white Gaussian noise (AWGN).

First of all, we assume that a vector $\mathbb{W}$ consists of independent and identically distributed (i.i.d.) additive complex white Gaussian noise samples is as follows:

$$\begin{aligned}\mathbb{W} &= [W_1, W_2, \cdots, W_M], \text{ where}\\ W_k &= W_k^R + iW_k^I,\ k = 1, \cdots, M,\\ W_k^R &\sim N[0,\sigma^2],\ W_k^I \sim N[0,\sigma^2],\\ W_k^R &\perp\!\!\!\perp W_l^R,\ k \neq l,\\ W_k^I &\perp\!\!\!\perp W_l^I,\ k \neq l,\\ W_k^R &\perp\!\!\!\perp W_l^I,\ \forall k, l.\end{aligned}$$

From the above, we know that each complex AWGN sample W_k has the mean

$$\begin{aligned}E[W_k] &= E[W_k^R + iW_k^I]\\ &= E[W_k^R] + iE[W_k^I]\\ &= 0,\end{aligned}$$

and variance

$$\begin{aligned} Var[W_k] &= E[(W_k - E[W_k])^2] \\ &= E[W_k^2] \\ &= E[(W_k^R + iW_k^I)(W_k^R + iW_k^I)^*] \\ &= E[W_k^R W_k^R + W_k^I W_k^I] \\ &= 2\sigma^2. \end{aligned}$$

Furthermore, the digital filtering procedure can be viewed as the discrete convolution of noise samples and the digital filter samples. For a finite-energy transmitted waveform, its matching template waveform also has finite energy, so we have the output of the noise after the matched filtering process Y is,

$$Y = \sum_{k=1}^{N} a_k W_k \Delta t,$$

where the a_k are the sample values of the digital matched filter, Δt is the sampling interval, and $N\Delta t = T$ is the duration of the matching template waveform. Note that $M > N$, where N is the number of samples of the digital filter. Then the noise output Y has mean

$$\begin{aligned} E[Y] &= E\left[\sum_{k=1}^{N} a_k W_k \Delta t\right] \\ &= \Delta t \sum_{k=1}^{N} a_k E[W_k] \\ &= 0, \end{aligned}$$

and variance

$$\begin{aligned} Var[Y] &= E[(Y - E[Y])^2] \\ &= E[Y^2] \\ &= E\left[\left(\sum_{k=1}^{N} a_k W_k \Delta t\right)\left(\sum_{l=1}^{N} a_l W_l \Delta t\right)^*\right] \\ &= (\Delta t)^2 \sum_{k=1}^{N}\sum_{l=1}^{N} a_k a_l^* E[W_k W_l^*] \\ &= (\Delta t)^2 \sum_{k=1}^{N} a_k a_k^* \cdot 2\sigma^2 \\ &= (\Delta t)^2 \cdot 2\sigma^2 \sum_{k=1}^{N} |a_k|^2. \end{aligned}$$

Hence, $Y \sim CN\left[0, (\Delta t)^2 \cdot 2\sigma^2 \sum_{k=1}^{N} |a_k|^2\right]$. Also, we know that the additive white Gaussian noise samples are with two-sided power spectral density (PSD) $N_0/2$, so $\sigma^2 = N_0$, and

$$Var[Y] = (\Delta t)^2 \cdot 2N_0 \sum_{k=1}^{N} |a_k|^2.$$

Furthermore, when we sample the signal at the Nyquist sampling rate, the corresponding matched filter has the same sampling rate, so we have $\Delta t = T/N$. Then

$$Var[Y] = (\frac{T}{N})^2 \cdot 2N_0 \sum_{k=1}^{N} |a_k|^2.$$

By the Weak Law of Large Number [54], we know that

$$\frac{1}{N} \sum_{k=1}^{N} |Y_k|^2 \xrightarrow{p} E[|Y|^2],$$

where the Y_k, $k = 1, 2, \cdots, N$ are independent and identically distributed. Therefore, we know that for the uncorrelated Gaussian (hence independent) noise output samples Y_k (time domain samples), the average output noise power converges in probability to $E[|Y|^2]$, which is equal to $Var[Y]$.

Now, for the transmitted signal $s_{Tx}(t)$, we have the digital matched filter output as follows,

$$\begin{aligned} Z &= \sum_{k=1}^{N} s_{Tx}(k\Delta t) s_{Tx}^{*}(k\Delta t)\Delta t \\ &= \Delta t \sum_{k=1}^{N} a_k a_k^{*} \\ &= \frac{T}{N} \sum_{k=1}^{N} |a_k|^2 \end{aligned}$$

Note that $s(k\Delta t) = a_k, k = 1, \cdots, N$. Hence, the signal to noise ratio at the output of the digital matched filter becomes

$$\begin{aligned} SNR &= \frac{|Z|^2}{E[|Y|^2]} \\ &= \frac{\sum_{k=1}^{N} |a_k|^2}{2N_0}, \end{aligned}$$

which equals to $N/2N_0$ if $|a_k| = 1, k = 1, \cdots, N$.

3.6 Target Parameter Estimate System and Algorithm

In this section, we first show the whole target parameter estimate system in Figure 3.11.

Then, the complete algorithm of chirp radar target parameter estimate system is generalized and summarized as follows (we let a point source at $(\hat{\tau}, \hat{\nu})$ convolved with the point spread function be $\tilde{P}_{\hat{\tau},\hat{\nu}}(\tau, \nu)$):

Input: matched filter delay-Doppler output $\tilde{O}(\tau, \nu)$.

Output: $(\hat{\tau}_{LS1}^{(1)}, \hat{\nu}_{LS1}^{(1)}, \hat{a}_{LS1}^{(1)}, \hat{\tau}_{LS2}^{(1)}, \hat{\nu}_{LS2}^{(1)}, \hat{a}_{LS2}^{(1)}, \cdots)$.

Initialization $\tilde{O}_{Res}^{(0)}(\tau, \nu) = \tilde{O}(\tau, \nu)$, $n = 1$, threshold ϵ.

Step 1: Apply CLEAN to pick $(\hat{\tau}_{CLEAN}, \hat{\nu}_{CLEAN}, \hat{a}_{CLEAN})$ from $\tilde{O}_{Res}^{(0)}(\tau, \nu)$.

while $\max \left| \tilde{O}_{Res}^{(n-1)}(\tau, \nu) \right| \geq \epsilon$ **do**

Step 2: Sample along the line through $(\hat{\tau}_{CLEAN}, \hat{\nu}_{CLEAN})$ and with slope α from the response $\tilde{O}_{Res}^{(n-1)}(\tau, \nu)$.

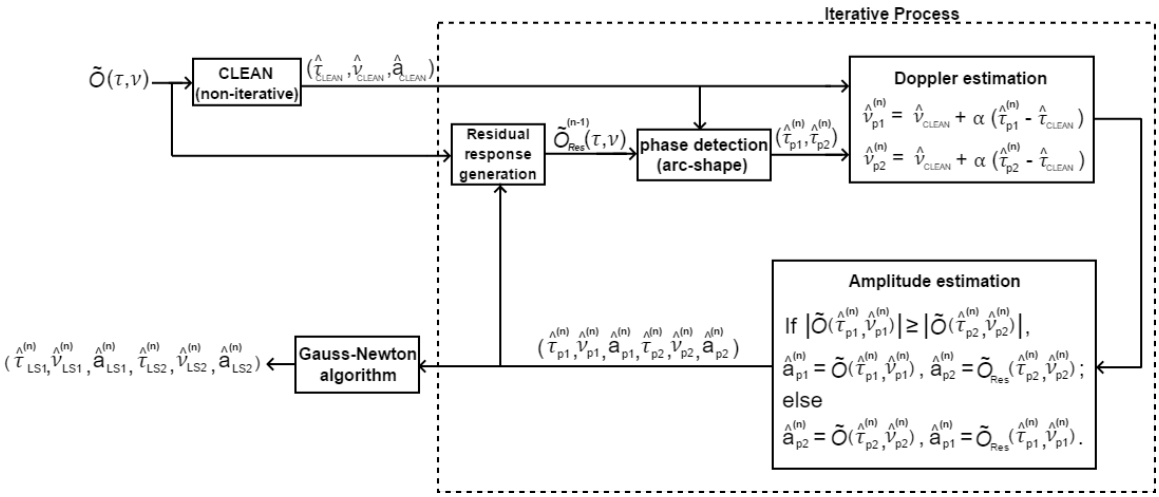

Fig. 3.11. Target parameter estimate system.

Step 3: Generate the phase of each sample from Step 2.

Step 4: Calculate the phase difference between every two neighboring samples from Step 3.

Step 5: Detect the positions with consecutively increasing (decreasing) in slope from the phase difference result. The qualified positions are the edges of targets' delay-Doppler response ($\hat{\tau}_{edge1}^{(n)}$ and $\hat{\tau}_{edge2}^{(n)}$, where $\hat{\tau}_{edge1}^{(n)} \leq \hat{\tau}_{edge2}^{(n)}$).

Step 6: Delay estimates: $\hat{\tau}_{p1}^{(n)} = \hat{\tau}_{edge1}^{(n)} + T$ and $\hat{\tau}_{p2}^{(n)} = \hat{\tau}_{edge2}^{(n)} - T$.

Step 7: Doppler shift estimates: $\hat{\nu}_{p1}^{(n)} = \hat{\nu}_{CLEAN} + \alpha(\hat{\tau}_{p1}^{(n)} - \hat{\tau}_{CLEAN})$ and $\hat{\nu}_{p2}^{(n)} = \hat{\nu}_{CLEAN} + \alpha(\hat{\tau}_{p2}^{(n)} - \hat{\tau}_{CLEAN})$.

Step 8: **if** $\left|\tilde{O}_{Res}^{(n-1)}(\hat{\tau}_{p1}^{(n)}, \hat{\nu}_{p1}^{(n)})\right| \geq \left|\tilde{O}_{Res}^{(n-1)}(\hat{\tau}_{p2}^{(n)}, \hat{\nu}_{p2}^{(n)})\right|$ **then**

$\hat{a}_{p1}^{(n)} = \tilde{O}_{Res}^{(n-1)}(\hat{\tau}_{p1}^{(n)}, \hat{\nu}_{p1}^{(n)})$,

$\hat{a}_{p2}^{(n)} = \tilde{O}_{Res}^{(n-1)}(\hat{\tau}_{p2}^{(n)}, \hat{\nu}_{p2}^{(n)}) - \hat{a}_{p1}^{(n)} \cdot \tilde{P}_{\hat{\tau}_{p1}^{(n)}, \hat{\nu}_{p1}^{(n)}}(\hat{\tau}_{p2}^{(n)}, \hat{\nu}_{p2}^{(n)})$

else

$\hat{a}_{p2}^{(n)} = \tilde{O}_{Res}^{(n-1)}(\hat{\tau}_{p2}^{(n)}, \hat{\nu}_{p2}^{(n)})$,

$\hat{a}_{p1}^{(n)} = \tilde{O}_{Res}^{(n-1)}(\hat{\tau}_{p1}^{(n)}, \hat{\nu}_{p1}^{(n)}) - \hat{a}_{p2}^{(n)} \cdot \tilde{P}_{\hat{\tau}_{p2}^{(n)}, \hat{\nu}_{p2}^{(n)}}(\hat{\tau}_{p1}^{(n)}, \hat{\nu}_{p1}^{(n)})$

end if

Step 9: $\tilde{O}_{Res}^{(n)}(\tau, \nu) = \tilde{O}_{Res}^{(n-1)}(\tau, \nu) - \hat{a}_{p1}^{(n)} \cdot \tilde{P}_{\hat{\tau}_{p1}^{(n)}, \hat{\nu}_{p1}^{(n)}}(\tau, \nu) - \hat{a}_{p2}^{(n)} \cdot \tilde{P}_{\hat{\tau}_{p2}^{(n)}, \hat{\nu}_{p2}^{(n)}}(\tau, \nu)$.

Step 10: record $(\hat{\tau}_{p1}^{(n)}, \hat{\nu}_{p1}^{(n)}, \hat{a}_{p1}^{(n)}, \hat{\tau}_{p2}^{(n)}, \hat{\nu}_{p2}^{(n)}, \hat{a}_{p2}^{(n)})$, $n = n + 1$.

end while

Step 11: Apply all estimated target parameters as the initial parameters $(\hat{\tau}_{p1}^{(1)}, \hat{\nu}_{p1}^{(1)}, \hat{a}_{p1}^{(1)}, \hat{\tau}_{p2}^{(1)}, \hat{\nu}_{p2}^{(1)}, \hat{a}_{p2}^{(1)}, \cdots)$, then do the Gauss-Newton algorithm to find the nonlinear least squares estimates of target parameters, $(\hat{\tau}_{LS1}^{(1)}, \hat{\nu}_{LS1}^{(1)}, \hat{a}_{LS1}^{(1)}, \hat{\tau}_{LS2}^{(1)}, \hat{\nu}_{LS2}^{(1)}, \hat{a}_{LS2}^{(1)}, \cdots)$.

3.7 Estimator Performance

3.7.1 Case 1

The performance of the target parameter estimate system is shown in Table 3.1. Here we apply six different cases, from 50% to 75%, which represent different percentages of overlap of two targets' matched filter output response. All six cases are under the condition that two targets lying along a ridge line with slope α. Moreover, in each case, we run the estimator 1000 times (generate 1000 different complex AWGN input patterns), and we fix the SNR to 30dB. Then we check the probability of successful estimate (the estimated parameters are convergent and are within the tolerable region, i.e., $|\tau - \hat{\tau}_{pk}| \leq 0.1T$ and $|\nu - \hat{\nu}_{pk}| \leq \alpha \cdot 0.1T$, or $|\tau - \hat{\tau}_{LSk}| \leq 0.1T$ and $|\nu - \hat{\nu}_{LSk}| \leq \alpha \cdot 0.1T$, $\forall k$).

From the performance results we know that the noise-target fringe analysis approach for target parameter estimate can have near to 90% success. Moreover, if we regard the parameters as the initial parameters and further apply the Gauss-Newton optimization, we can achieve above a 90% successful estimation rate.

Table 3.1. Probability of successful parameter estimate. %Overlap means the percentage of overlap of two targets' matched filter output responses. $\underline{\hat{\theta}}_{pk}$ is the parameter vector estimated by the output of the noise-target fringe analysis, i.e., $\underline{\hat{\theta}}_{pk} = (\hat{\tau}_{p1}, \hat{\nu}_{p1}, \hat{a}_{p1}, \hat{\tau}_{p2}, \hat{\nu}_{p2}, \hat{a}_{p2})$; $\underline{\hat{\theta}}_{LSk}$ is the parameter vector estimated by the output of the Gauss-Newton algorithm, i.e., $\underline{\hat{\theta}}_{LSk} = (\hat{\tau}_{LS1}, \hat{\nu}_{LS1}, \hat{a}_{LS1}, \hat{\tau}_{LS2}, \hat{\nu}_{LS2}, \hat{a}_{LS2})$.

Success Prob. %Overlap / Parameter	50%	55%	60%	65%	70%	75%
$\underline{\hat{\theta}}_{pk}$	95.0%	96.5%	92.8%	88.8%	87.0%	92.8%
$\underline{\hat{\theta}}_{LSk}$	97.7%	98.8%	96.0%	90.2%	92.0%	99.5%

3.7.2 Case 2

Now we consider the four-target case, i.e., four targets lie along a line with slope α, the chirp rate of transmitted waveform. The three different scenarios are:

Scenario 1: The target parameters (normalized) are

$$(\tau_1/T, \nu_1 T, a_1) = (0, 0, 1),$$
$$(\tau_2/T, \nu_2 T, a_2) = (0.5, 5, 1),$$
$$(\tau_3/T, \nu_3 T, a_3) = (1, 10, 1),$$
$$(\tau_4/T, \nu_4 T, a_4) = (1.5, 15, 1).$$

Scenario 2: The target parameters (normalized) are

$$(\tau_1/T, \nu_1 T, a_1) = (0, 0, 1),$$
$$(\tau_2/T, \nu_2 T, a_2) = (0.5, 5, 0.5),$$
$$(\tau_3/T, \nu_3 T, a_3) = (1, 10, 0.5),$$
$$(\tau_4/T, \nu_4 T, a_4) = (1.5, 15, 1).$$

Scenario 3: The target parameters (normalized) are

$$(\tau_1/T, \nu_1 T, a_1) = (0, 0, 0.5),$$
$$(\tau_2/T, \nu_2 T, a_2) = (0.5, 5, 1),$$
$$(\tau_3/T, \nu_3 T, a_3) = (1, 10, 1),$$
$$(\tau_4/T, \nu_4 T, a_4) = (1.5, 15, 0.5).$$

The chirp matched filter delay-Doppler output response (noise-free) corresponding to the three scenarios are shown in Figure 3.12, 3.13 and 3.14.

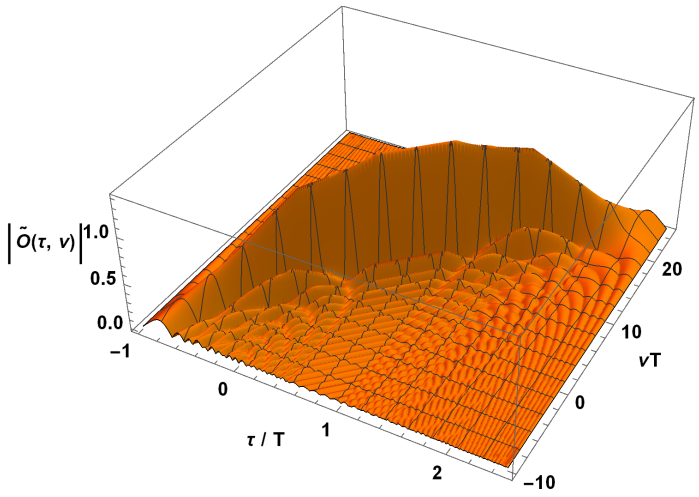

Fig. 3.12. Chirp matched filter delay-Doppler output response of scenario 1.

Now, under the 30dB maximal SNR (at the matched filter output) condition, we compare the performance of targets' delay-Doppler estimates based on the following metric (the waveform duration T can be ignored by setting it equal to 1):

$$\mathcal{P} = \frac{1}{4} \sum_{k=1}^{4} \left[(\hat{\tau}_k - \tau_k)^2 + (\hat{\nu}_k - \nu_k)^2 \right],$$

which tells us the averaged squared distance between the true target's delay-Doppler position and the delay-Doppler position of the estimated target. The four targets' parameters at the estimator output are reordered (according to their delay values) before calculating the performance metric $\mathcal{P}$.

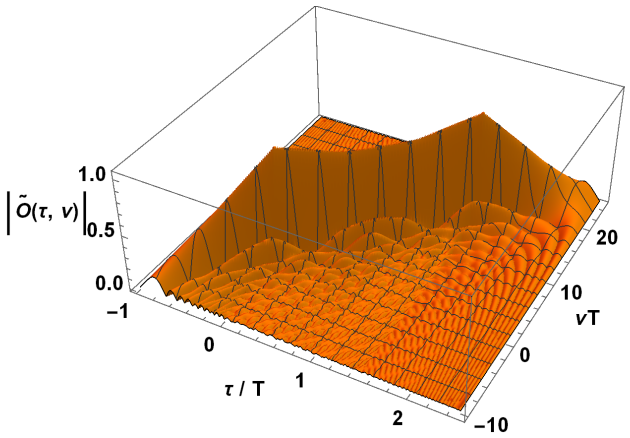

Fig. 3.13. Chirp matched filter delay-Doppler output response of scenario 2.

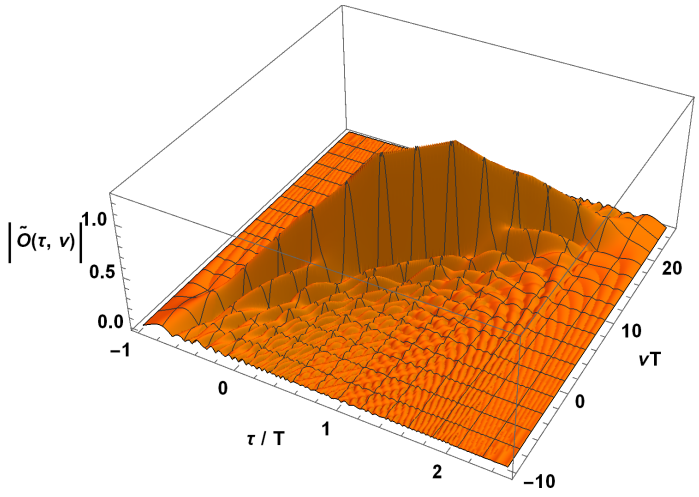

Fig. 3.14. Chirp matched filter delay-Doppler output response of scenario 3.

Here, two different estimators are compared: 1) the coherent CLEAN estimator, and 2) the noise-target fringe analysis (NTFA) estimator, and in each scenario we run the two estimators 200 times (generate 200 different complex AWGN input patterns and then apply the input patterns to two estimators separately), and the results (200 times averaging) are shown in Table 3.2. The results show that the noise-target fringe analysis estimator can have a more accurate delay-Doppler estimate than the coherent CLEAN estimators. The large averaged squared error of the coherent CLEAN estimator comes from the fact that it almost recognizes four targets as only three

Table 3.2. Estimator performance comparison.

	Scenario 1	Scenario 2	Scenario 3
$\mathcal{P}_{\text{coherentCLEAN}}$	10.3132	5.38245	4.29357
$\mathcal{P}_{\text{NTFA}}$	3.12587	3.92539	2.73756

targets, i.e., two of the four targets are estimated with nearly the same delay and Doppler value. However, the noise-target fringe analysis estimator has higher probability in discriminating all four targets, and the corresponding averaged squared error is smaller than the averaged squared error of the coherent CLEAN estimator. In Table 3.3, we randomly pick a number of simulation results, and we can easily see that the coherent CLEAN estimator usually regards four targets as three targets. Therefore, the noise-target fringe analysis estimator has better ability in target separation than the pure coherent CLEAN estimator. To get more accurate delay-Doppler estimates, we can further apply the Gauss-Newton algorithm to get the nonlinear least squares estimates of all target parameters.

Table 3.3.: Delay-Doppler estimates of two estimators.

j-th time	pure coherent CLEAN	noist-target fringe analysis
1	$(\hat{\tau}_1, \hat{\nu}_1) = (0.01, 0.2)$ $(\hat{\tau}_2, \hat{\nu}_2) = (1, 9.94)$ $(\hat{\tau}_3, \hat{\nu}_3) = (1, 10.82)$ $(\hat{\tau}_4, \hat{\nu}_4) = (1.5, 15.1)$ $\mathcal{P} = 6.343$	$(\hat{\tau}_1, \hat{\nu}_1) = (0, 0.1)$ $(\hat{\tau}_2, \hat{\nu}_2) = (0.71, 7.2)$ $(\hat{\tau}_3, \hat{\nu}_3) = (1.12, 11.3)$ $(\hat{\tau}_4, \hat{\nu}_4) = (1.42, 14.3)$ $\mathcal{P} = 1.774$
2	$(\hat{\tau}_1, \hat{\nu}_1) = (0, 0.12)$ $(\hat{\tau}_2, \hat{\nu}_2) = (0.5, 4.88)$ $(\hat{\tau}_3, \hat{\nu}_3) = (0.5, 5.74)$	$(\hat{\tau}_1, \hat{\nu}_1) = (-0.02, -0.08)$ $(\hat{\tau}_2, \hat{\nu}_2) = (0.86, 8.72)$ $(\hat{\tau}_3, \hat{\nu}_3) = (1.2, 12.12)$

Continued on next page

Table 3.3.: Delay-Doppler estimates of two estimators. (cont.)

j-th time	pure coherent CLEAN	noist-target fringe analysis
	$(\hat{\tau}_4, \hat{\nu}_4) = (1.51, 15.22)$	$(\hat{\tau}_4, \hat{\nu}_4) = (1.49, 15.02)$
	$\mathcal{P} = 4.618$	$\mathcal{P} = 4.626$
	$(\hat{\tau}_1, \hat{\nu}_1) = (0., 0.09)$	$(\hat{\tau}_1, \hat{\nu}_1) = (-0.02, -0.11)$
	$(\hat{\tau}_2, \hat{\nu}_2) = (1., 9.92)$	$(\hat{\tau}_2, \hat{\nu}_2) = (0.7, 7.09)$
3	$(\hat{\tau}_3, \hat{\nu}_3) = (1.01, 10.83)$	$(\hat{\tau}_3, \hat{\nu}_3) = (1.02, 10.29)$
	$(\hat{\tau}_4, \hat{\nu}_4) = (1.5, 15.12)$	$(\hat{\tau}_4, \hat{\nu}_4) = (1.41, 14.19)$
	$\mathcal{P} = 6.291$	$\mathcal{P} = 1.292$
	$(\hat{\tau}_1, \hat{\nu}_1) = (0., 0.1)$	$(\hat{\tau}_1, \hat{\nu}_1) = (0., 0.1)$
	$(\hat{\tau}_2, \hat{\nu}_2) = (0.5, 4.93)$	$(\hat{\tau}_2, \hat{\nu}_2) = (0.91, 9.2)$
4	$(\hat{\tau}_3, \hat{\nu}_3) = (0.51, 5.88)$	$(\hat{\tau}_3, \hat{\nu}_3) = (1.22, 12.3)$
	$(\hat{\tau}_4, \hat{\nu}_4) = (1.5, 15.1)$	$(\hat{\tau}_4, \hat{\nu}_4) = (1.49, 15.0)$
	$\mathcal{P} = 4.309$	$\mathcal{P} = 5.788$
	$(\hat{\tau}_1, \hat{\nu}_1) = (0., 0.13)$	$(\hat{\tau}_1, \hat{\nu}_1) = (0., 0.11)$
	$(\hat{\tau}_2, \hat{\nu}_2) = (0.5, 5.71)$	$(\hat{\tau}_2, \hat{\nu}_2) = (0.7, 7.11)$
5	$(\hat{\tau}_3, \hat{\nu}_3) = (0.51, 4.98)$	$(\hat{\tau}_3, \hat{\nu}_3) = (1.25, 12.61)$
	$(\hat{\tau}_4, \hat{\nu}_4) = (1.5, 15.11)$	$(\hat{\tau}_4, \hat{\nu}_4) = (1.47, 14.81)$
	$\mathcal{P} = 6.493$	$\mathcal{P} = 2.853$
	$(\hat{\tau}_1, \hat{\nu}_1) = (0, 0.14)$	$(\hat{\tau}_1, \hat{\nu}_1) = (0, 0.14)$
	$(\hat{\tau}_2, \hat{\nu}_2) = (0.48, 5.54)$	$(\hat{\tau}_2, \hat{\nu}_2) = (0.83, 8.44)$
6	$(\hat{\tau}_3, \hat{\nu}_3) = (0.5, 4.92)$	$(\hat{\tau}_3, \hat{\nu}_3) = (1, 10.14)$
	$(\hat{\tau}_4, \hat{\nu}_4) = (1.5, 15.11)$	$(\hat{\tau}_4, \hat{\nu}_4) = (1.48, 14.94)$
	$\mathcal{P} = 6.594$	$\mathcal{P} = 2.996$
	$(\hat{\tau}_1, \hat{\nu}_1) = (0.01, 0.2)$	$(\hat{\tau}_1, \hat{\nu}_1) = (0, 0.15)$
	$(\hat{\tau}_2, \hat{\nu}_2) = (0.51, 4.92)$	$(\hat{\tau}_2, \hat{\nu}_2) = (0.44, 4.55)$
7	$(\hat{\tau}_3, \hat{\nu}_3) = (0.59, 6.63)$	$(\hat{\tau}_3, \hat{\nu}_3) = (0.49, 5.05)$
	$(\hat{\tau}_4, \hat{\nu}_4) = (1.5, 15.15)$	$(\hat{\tau}_4, \hat{\nu}_4) = (1.42, 14.35)$
		Continued on next page

Table 3.3.: Delay-Doppler estimates of two estimators. (cont.)

j-th time	pure coherent CLEAN	noist-target fringe analysis
	$\mathcal{P} = 2.898$	$\mathcal{P} = 6.354$
8	$(\hat{\tau}_1, \hat{\nu}_1) = (0., 0.12)$ $(\hat{\tau}_2, \hat{\nu}_2) = (0.9, 9.88)$ $(\hat{\tau}_3, \hat{\nu}_3) = (1.01, 10)$ $(\hat{\tau}_4, \hat{\nu}_4) = (1.5, 15.1)$ $\mathcal{P} = 5.999$	$(\hat{\tau}_1, \hat{\nu}_1) = (0., 0.1)$ $(\hat{\tau}_2, \hat{\nu}_2) = (0.35, 3.6)$ $(\hat{\tau}_3, \hat{\nu}_3) = (0.82, 8.3)$ $(\hat{\tau}_4, \hat{\nu}_4) = (1.42, 14.3)$ $\mathcal{P} = 1.353$
9	$(\hat{\tau}_1, \hat{\nu}_1) = (0, 0.12)$ $(\hat{\tau}_2, \hat{\nu}_2) = (1, 9.86)$ $(\hat{\tau}_3, \hat{\nu}_3) = (1.01, 10.8)$ $(\hat{\tau}_4, \hat{\nu}_4) = (1.5, 15.1)$ $\mathcal{P} = 6.133$	$(\hat{\tau}_1, \hat{\nu}_1) = (0.06, 0.7)$ $(\hat{\tau}_2, \hat{\nu}_2) = (0.63, 6.4)$ $(\hat{\tau}_3, \hat{\nu}_3) = (0.96, 9.7)$ $(\hat{\tau}_4, \hat{\nu}_4) = (1.47, 14.8)$ $\mathcal{P} = 0.651$
10	$(\hat{\tau}_1, \hat{\nu}_1) = (0, 0.1)$ $(\hat{\tau}_2, \hat{\nu}_2) = (1, 10.75)$ $(\hat{\tau}_3, \hat{\nu}_3) = (1.01, 10.01)$ $(\hat{\tau}_4, \hat{\nu}_4) = (1.51, 15.21)$ $\mathcal{P} = 8.341$	$(\hat{\tau}_1, \hat{\nu}_1) = (0, 0.11)$ $(\hat{\tau}_2, \hat{\nu}_2) = (0.26, 2.71)$ $(\hat{\tau}_3, \hat{\nu}_3) = (0.48, 4.91)$ $(\hat{\tau}_4, \hat{\nu}_4) = (1.42, 14.31)$ $\mathcal{P} = 7.993$
11	$(\hat{\tau}_1, \hat{\nu}_1) = (0.01, 0.22)$ $(\hat{\tau}_2, \hat{\nu}_2) = (1, 9.9)$ $(\hat{\tau}_3, \hat{\nu}_3) = (1.01, 10.86)$ $(\hat{\tau}_4, \hat{\nu}_4) = (1.5, 15.11)$ $\mathcal{P} = 6.264$	$(\hat{\tau}_1, \hat{\nu}_1) = (0.06, 0.71)$ $(\hat{\tau}_2, \hat{\nu}_2) = (0.61, 6.2)$ $(\hat{\tau}_3, \hat{\nu}_3) = (0.7, 7.11)$ $(\hat{\tau}_4, \hat{\nu}_4) = (1.48, 14.91)$ $\mathcal{P} = 2.608$
12	$(\hat{\tau}_1, \hat{\nu}_1) = (0, 0.1)$ $(\hat{\tau}_2, \hat{\nu}_2) = (1, 9.91)$ $(\hat{\tau}_3, \hat{\nu}_3) = (1, 10.67)$ $(\hat{\tau}_4, \hat{\nu}_4) = (1.5, 15.1)$	$(\hat{\tau}_1, \hat{\nu}_1) = (0, 0.1)$ $(\hat{\tau}_2, \hat{\nu}_2) = (0.6, 6.1)$ $(\hat{\tau}_3, \hat{\nu}_3) = (1.19, 12.0)$ $(\hat{\tau}_4, \hat{\nu}_4) = (1.49, 15.0)$
		Continued on next page

Table 3.3.: Delay-Doppler estimates of two estimators. (cont.)

j-th time	pure coherent CLEAN	noist-target fringe analysis
	$\mathcal{P} = 6.206$	$\mathcal{P} = 1.316$
13	$(\hat{\tau}_1, \hat{\nu}_1) = (0.01, 0.22)$ $(\hat{\tau}_2, \hat{\nu}_2) = (0.9, 9.84)$ $(\hat{\tau}_3, \hat{\nu}_3) = (1.01, 10.05)$ $(\hat{\tau}_4, \hat{\nu}_4) = (1.5, 15.11)$ $\mathcal{P} = 5.912$	$(\hat{\tau}_1, \hat{\nu}_1) = (0.04, 0.52)$ $(\hat{\tau}_2, \hat{\nu}_2) = (0.3, 3.12)$ $(\hat{\tau}_3, \hat{\nu}_3) = (0.44, 4.52)$ $(\hat{\tau}_4, \hat{\nu}_4) = (1.42, 14.32)$ $\mathcal{P} = 8.664$
14	$(\hat{\tau}_1, \hat{\nu}_1) = (0, 0.1)$ $(\hat{\tau}_2, \hat{\nu}_2) = (1, 10.83)$ $(\hat{\tau}_3, \hat{\nu}_3) = (1.01, 10.06)$ $(\hat{\tau}_4, \hat{\nu}_4) = (1.5, 15.1)$ $\mathcal{P} = 8.565$	$(\hat{\tau}_1, \hat{\nu}_1) = (0, 0.1)$ $(\hat{\tau}_2, \hat{\nu}_2) = (0.9, 9.1)$ $(\hat{\tau}_3, \hat{\nu}_3) = (1.22, 12.3)$ $(\hat{\tau}_4, \hat{\nu}_4) = (1.48, 14.9)$ $\mathcal{P} = 5.582$
15	$(\hat{\tau}_1, \hat{\nu}_1) = (0, 0.1)$ $(\hat{\tau}_2, \hat{\nu}_2) = (0.5, 4.79)$ $(\hat{\tau}_3, \hat{\nu}_3) = (0.5, 5.63)$ $(\hat{\tau}_4, \hat{\nu}_4) = (1.5, 15.11)$ $\mathcal{P} = 4.853$	$(\hat{\tau}_1, \hat{\nu}_1) = (0.03, 0.4)$ $(\hat{\tau}_2, \hat{\nu}_2) = (0.32, 3.3)$ $(\hat{\tau}_3, \hat{\nu}_3) = (0.87, 8.8)$ $(\hat{\tau}_4, \hat{\nu}_4) = (1.5, 15.1)$ $\mathcal{P} = 1.137$
16	$(\hat{\tau}_1, \hat{\nu}_1) = (0, 0.12)$ $(\hat{\tau}_2, \hat{\nu}_2) = (1, 9.91)$ $(\hat{\tau}_3, \hat{\nu}_3) = (1.01, 10.86)$ $(\hat{\tau}_4, \hat{\nu}_4) = (1.51, 15.22)$ $\mathcal{P} = 6.29$	$(\hat{\tau}_1, \hat{\nu}_1) = (0, 0.12)$ $(\hat{\tau}_2, \hat{\nu}_2) = (0.61, 6.22)$ $(\hat{\tau}_3, \hat{\nu}_3) = (0.88, 8.92)$ $(\hat{\tau}_4, \hat{\nu}_4) = (1.5, 15.12)$ $\mathcal{P} = 0.677$
17	$(\hat{\tau}_1, \hat{\nu}_1) = (0.01, 0.2)$ $(\hat{\tau}_2, \hat{\nu}_2) = (0.89, 9.76)$ $(\hat{\tau}_3, \hat{\nu}_3) = (1.01, 10.04)$ $(\hat{\tau}_4, \hat{\nu}_4) = (1.5, 15.11)$	$(\hat{\tau}_1, \hat{\nu}_1) = (-0.01, 0.0)$ $(\hat{\tau}_2, \hat{\nu}_2) = (0.81, 8.2)$ $(\hat{\tau}_3, \hat{\nu}_3) = (0.86, 8.67)$ $(\hat{\tau}_4, \hat{\nu}_4) = (1.52, 15.3)$
		Continued on next page

Table 3.3.: Delay-Doppler estimates of two estimators. (cont.)

j-th time	pure coherent CLEAN	noist-target fringe analysis
	$\mathcal{P} = 5.715$	$\mathcal{P} = 3.033$
18	$(\hat{\tau}_1, \hat{\nu}_1) = (0, 0.11)$ $(\hat{\tau}_2, \hat{\nu}_2) = (1, 10)$ $(\hat{\tau}_3, \hat{\nu}_3) = (1.01, 10.92)$ $(\hat{\tau}_4, \hat{\nu}_4) = (1.5, 15.1)$ $\mathcal{P} = 6.529$	$(\hat{\tau}_1, \hat{\nu}_1) = (0, 0.11)$ $(\hat{\tau}_2, \hat{\nu}_2) = (0.3, 3.11)$ $(\hat{\tau}_3, \hat{\nu}_3) = (1.14, 11.51)$ $(\hat{\tau}_4, \hat{\nu}_4) = (1.48, 14.91)$ $\mathcal{P} = 1.483$
19	$(\hat{\tau}_1, \hat{\nu}_1) = (0, 0.12)$ $(\hat{\tau}_2, \hat{\nu}_2) = (0.5, 4.9)$ $(\hat{\tau}_3, \hat{\nu}_3) = (0.5, 5.72)$ $(\hat{\tau}_4, \hat{\nu}_4) = (1.5, 15.13)$ $\mathcal{P} = 4.652$	$(\hat{\tau}_1, \hat{\nu}_1) = (0., 0.13)$ $(\hat{\tau}_2, \hat{\nu}_2) = (0.26, 2.73)$ $(\hat{\tau}_3, \hat{\nu}_3) = (0.47, 4.83)$ $(\hat{\tau}_4, \hat{\nu}_4) = (1.42, 14.33)$ $\mathcal{P} = 8.172$
20	$(\hat{\tau}_1, \hat{\nu}_1) = (0, 0.11)$ $(\hat{\tau}_2, \hat{\nu}_2) = (1, 9.87)$ $(\hat{\tau}_3, \hat{\nu}_3) = (1.01, 10.82)$ $(\hat{\tau}_4, \hat{\nu}_4) = (1.5, 15.09)$ $\mathcal{P} = 6.165$	$(\hat{\tau}_1, \hat{\nu}_1) = (0, 0.09)$ $(\hat{\tau}_2, \hat{\nu}_2) = (0.74, 7.49)$ $(\hat{\tau}_3, \hat{\nu}_3) = (1.12, 11.29)$ $(\hat{\tau}_4, \hat{\nu}_4) = (1.42, 14.29)$ $\mathcal{P} = 2.113$

3.8 Summary and Conclusions

In this chapter, we established a radar target parameter estimate system, which is combined by the CLEAN algorithm, the noise-target fringe analysis and the Gauss-Newton optimization, to achieve high accuracy of target parameter estimate and the ability of target discrimination. Furthermore, we showed the outstanding performance of target discrimination of the noise-target fringe analysis approach in some cases that the chirp-matched-filtering-only can not achieve successful target discrimination. Therefore, this target parameter estimate system can not only enhance the α-rotated ridge resolution but achieve much better target-discrimination ability.

Moreover, from the derivations of the matched filter delay-Doppler output response (Equation (3.4)) and the correlation between two delay-Doppler matched filter outputs driven by AWGN input (Equation (3.15)), we know that the same phase variation behavior exists in a target's output response and in the output response of noise, which depends on the ambiguity function of the matching template waveform. Therefore, we can take advantage of the "same phase variation behavior but with different phase offsets" properties to indicate the fringe of a target's response and to provide the accurate target parameter estimates. For example, based on the shape of the ambiguity function of the matching template waveform, We can sample the highly correlated matched filter delay-Doppler outputs and observe the phase relationship among these output samples to find the fringe of a target's matched filter output response. In this way, the noise-target fringe analysis approach may be a useful tool for target parameter estimate in frequency-modulated and phase-coded radars.

4. CHIRP HYBRID FILTERS FOR DELAY-DOPPLER RESOLUTION ENHANCEMENT

4.1 Introduction

Delay-Doppler resolution is one of the most important metrics for assessing the performance of a radar system. It determines the ability of detecting targets with close distances and Doppler shifts. Compared to an unmodulated waveform, the chirp waveform, one kind of linear frequency modulation (LFM) waveform, has better range and Doppler resolution. Thus, chirp waveforms have become the most widely used waveform in radar systems.

The difference of an unmodulated rectangular pulse and a chirp pulse is that the matched filter output response of an unmodulated rectangular pulse has a triangular envelope in the delay axis ($\nu = 0$); however, the matched filter output response of a chirp pulse also has a triangular envelope but along the α-rotated axis ($\nu = \alpha\tau$), where α is the chirp rate of the chirp pulse. Therefore, when any pair of targets are close enough in delay and Doppler shift, and they have a Doppler shift difference which equals to their delay difference multiply by the chirp rate of the transmitted chirp waveform α, the traditional chirp matched filter output response will have a mixed envelope combined by two partially overlapping triangular envelopes. Furthermore, when one of the two target returns is smaller, the smaller triangular envelope may be concealed in the mixed envelope, causing a missed detection of the smaller target. In this situation, the chirp matched filtering process may not work well in detecting and resolving two targets.

To solve this problem, we apply a mismatched filter, which considers a chirp waveform with chirp rate β ($\beta \neq \alpha$) as a matching template, to change the slope of the triangular envelope (ridge) of the filter output response. Then we combine

the linearly-shifted delay-Doppler responses to correct all targets' delays and Doppler shifts. Finally, we apply some non-linear processing to the matched filter output response and the combination of linearly-shifted mismatched filter output responses. For each target, because there are two triangular envelopes with the same peak (target's (τ, ν) position) but with different ridge slopes, if a non-linear processing is properly applied, any pair of targets under the above-mentioned condition can be easily detected and resolved. Therefore, the target resolution capability can be greatly improved.

Also, in terms of system complexity issues, the mismatched filter only changes the matching template from the matched chirp waveform to a chirp waveform with another chirp rate, and pre-multiplies by a continuous wave (for the e^{it^2}-term cancellation) before the filtering process. Thus, the mismatched filtering does not cause heavy computational complexity. In addition, the transmitter is completely the same as in a traditional chirp radar system; therefore, the mismatched filtering process can be added to any chirp radar system without affecting the original functionality. Figure 4.1 is whole chirp hybrid filter system structure.

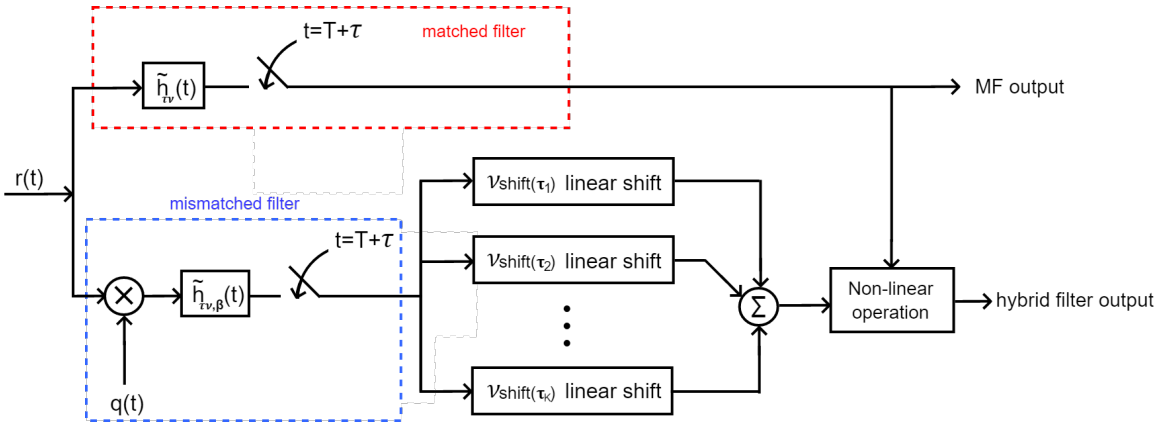

Fig. 4.1. Chirp hybrid filter structure.

4.2 Mathematical Model for Mismatched Filter

In a chirp radar system, a chirp waveform of duration T and chirp rate α of the following form is generated and transmitted:

$$s_{Tx}(t) = e^{i\pi\alpha t^2} \cdot 1_{[0,T]}(t). \tag{4.1}$$

At the receiver, the received waveform is the combination of all targets' reflected waveforms (here we assume that for target k, the delay and Doppler shift are (τ_k, ν_k), $k = 1, 2, \cdots$.), and it can be represented as

$$\begin{aligned} s_{Recv}(t) &= \sum_k a_k s_{\tau_k \nu_k}(t) \\ &= \sum_k a_k s_{Tx}(t - \tau_k) e^{i2\pi\nu_k t} \\ &= \sum_k a_k e^{i\pi\alpha(t-\tau_k)^2} \cdot 1_{[0,T]}(t - \tau_k) e^{i2\pi\nu_k t}, \end{aligned} \tag{4.2}$$

where a_k is the amplitude of the k-th target's reflected waveform, τ_k is the delay (two-way) of the k-th target's reflected waveform, and ν_k is the Doppler shift of the k-th target's reflected waveform. Note that any two different targets, which are at (τ_m, ν_m) and $(\tau_n, \nu_n), m \neq n$, can only have the same delay ($\tau_m = \tau_n$) or the same Doppler shift ($\nu_m = \nu_n$) because we regard two targets with the same delay and same Doppler shift ($\tau_m = \tau_n$ and $\nu_m = \nu_n$) as the same target.

Now, in traditional matched filter designs, a specific matching template $g(t) = s_{Tx}(t)$ is applied, and a matched filter matched to a τ-delayed, ν-Doppler shifted version of a template signal is

$$\begin{aligned} g_{\tau\nu}(t) &= s_{Tx}(t - \tau) e^{i2\pi\nu t} \\ &= e^{i\pi\alpha(t-\tau)^2} \cdot 1_{[0,T]}(t - \tau) e^{i2\pi\nu t}, \end{aligned} \tag{4.3}$$

and sampled at time $t = T + \tau$. Then, the matched filter impulse response $\tilde{h}_{\tau\nu}(t)$ will be of the form

$$\begin{aligned}\tilde{h}_{\tau\nu}(t) &= g^*_{\tau\nu}(T + \tau - t) \\ &= s^*_{Tx}(T + \tau - t - \tau)e^{-i2\pi\nu(T+\tau-t)} \\ &= s^*_{Tx}(T - t)e^{-i2\pi\nu(T+\tau-t)} \\ &= e^{-i\pi\alpha(T-t)^2} \cdot 1_{[0,T]}(T - t)e^{-i2\pi\nu(T+\tau-t)}, \end{aligned} \tag{4.4}$$

and the matched filter output at time $t = T + \tau$ will be

$$\begin{aligned}&\tilde{O}_{\mathrm{MF}}(\tau, \nu) = s_{Recv}(t) * \tilde{h}_{\tau\nu}(t)|_{t=T+\tau} \\ &= \int_{-\infty}^{\infty} s_{Recv}(p)\tilde{h}_{\tau\nu}(t - p)dp|_{t=T+\tau} \\ &= \int_{-\infty}^{\infty} s_{Recv}(p)\tilde{h}_{\tau\nu}(T + \tau - p)dp \\ &= \int_{-\infty}^{\infty} \sum_k a_k s_{Tx}(p - \tau_k)e^{i2\pi\nu_k p} \cdot s^*_{Tx}(p - \tau)e^{-i2\pi\nu p}dp \\ &= \sum_k a_k \left(\int_{-\infty}^{\infty} s_{Tx}(p - \tau_k)s^*_{Tx}(p - \tau)e^{-i2\pi(\nu-\nu_k)p}dp \right) \\ &(\text{let } p - \tau_k = m_k,\ p = m_k + \tau_k, \text{ and } dp = dm_k) \\ &= \sum_k a_k \int_{-\infty}^{\infty} s_{Tx}(m_k)s^*_{Tx}(m_k - (\tau - \tau_k))e^{-i2\pi(\nu-\nu_k)(m_k+\tau_k)}dm_k \\ &= \sum_k a_k e^{-i2\pi(\nu-\nu_k)\tau_k} \int_{-\infty}^{\infty} s_{Tx}(m_k)s^*_{Tx}(m_k - (\tau - \tau_k))e^{-i2\pi(\nu-\nu_k)m_k}dm_k \\ &= \sum_k a_k e^{-i2\pi(\nu-\nu_k)\tau_k}\chi_s(\tau - \tau_k, \nu - \nu_k), \end{aligned} \tag{4.5}$$

where

$$\chi_s(\tau, \nu) = \int_{-\infty}^{\infty} s_{Tx}(t)s^*_{Tx}(t - \tau)e^{-i2\pi\nu t}dt$$

is the ambiguity function of the waveform $s_{Tx}(t)$. From the above equation we know that $\tilde{O}_{\mathrm{MF}}(\tau, \nu)$, the matched filter output response sampled at time $t = T + \tau$, is the combination of weighted and phase-shifted version of (τ_k, ν_k)-shifted ambiguity functions, where $k = 1, \cdots, K$. Here we let K be the total number of target returns.

Figure 4.2 shows the matched filter output response of a chirp transmitted waveform with chirp rate $\alpha = 54.0$ and a matched filter with the same chirp waveform as the matching template waveform (one target case). We can see that the delay-Doppler response has a peak at the target's true delay and Doppler shift. Furthermore, the output response has a ridge shape with a slope α, which corresponds to the chirp rate of the matching template waveform. Similarly, when the received signal is combined by signals from K different distances (delays), then the resulting matched filter output response is a linear combination of K different peak-shifted ambiguity functions, and the k-th delay-Doppler response has a peak value at (τ_k, ν_k), which corresponds to k-th target's delay and Doppler shift. Also, for all K delay-Doppler responses, they have the ridge shape with same slope α, which corresponds to the chirp rate of the matching template waveform.

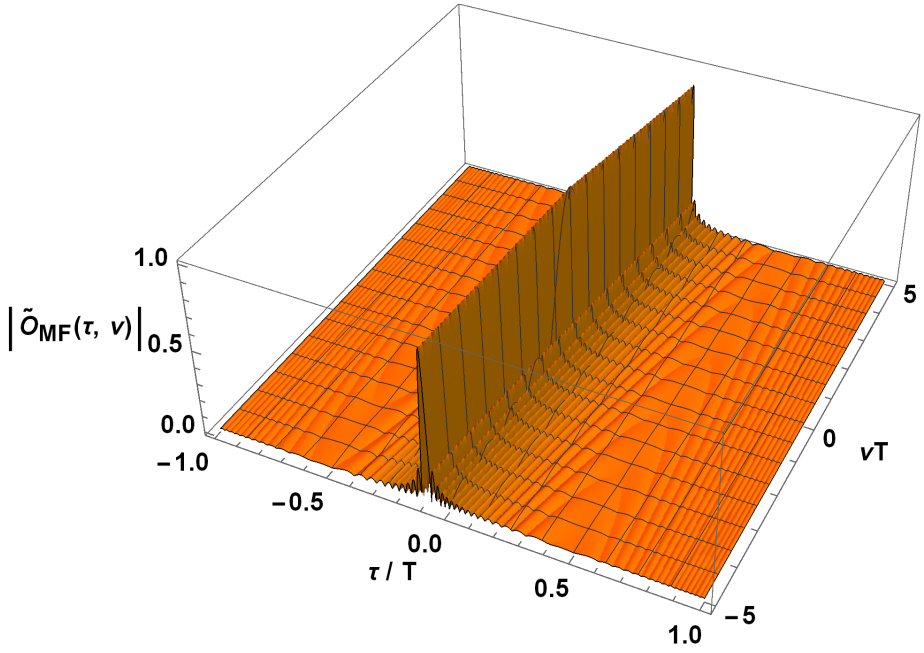

Fig. 4.2. Matched filter output response of a chirp transmitted waveform (chirp rate $\alpha = 54.0$).

This phenomenon led us to ask the questions: "What will happen to the slope of the ridge in delay-Doppler response when applying a matching template waveform

with a chirp rate different from the chirp rate of the transmitted waveform?", "Is it possible to acquire much better delay-Doppler resolution by doing some linear or non-linear operations in both the matched filter output response and the mismatched filter output response?", and "If the above thought works, then how much better with respect to delay and Doppler resolutions in this design than in the chirp matched filter delay-Doppler response?" Based on the motivations, in the following we introduce a mismatched filter which applies $g(t) = e^{i\pi\beta t^2} \cdot 1_{[0,T]}(t)$, $\beta \neq \alpha$, as a matching template signal.

Now, when the above matching template $g(t)$ is applied, we then have the mismatched filter impulse response

$$\begin{aligned}\tilde{h}_{\tau\nu,\beta}(t) &= g^*_{\tau\nu}(T+\tau-t) \\ &= g^*(T+\tau-t-\tau)e^{-i2\pi\nu(T+\tau-t)} \\ &= g^*(T-t)e^{-i2\pi\nu(T+\tau-t)} \\ &= e^{-i\pi\beta(T-t)^2} \cdot 1_{[0,T]}(T-t)e^{-i2\pi\nu(T+\tau-t)}, \end{aligned} \tag{4.6}$$

and the filter output response at time $t = T + \tau$ is

$$\begin{aligned}&\tilde{O}(\tau,\nu) = s_{Recv}(t) * \tilde{h}_{\tau\nu,\beta}(t)|_{t=T+\tau} \\ &= \sum_k a_k e^{-i\pi(\beta\tau^2-\alpha\tau_k^2)} \int_{-\infty}^{\infty} e^{-i\pi(\beta-\alpha)t^2} e^{-i2\pi[(\nu-\nu_k)-(\beta\tau-\alpha\tau_k)]t} \cdot 1_{[0,T]}(t-\tau_k)1_{[0,T]}(t-\tau)dt. \end{aligned} \tag{4.7}$$

From (4.7) we observe that the term $e^{-i\pi(\beta-\alpha)t^2}$ exists inside the integration, which will destroy the ridge shape in the delay-Doppler response. So, before the mismatched filtering process, we can pre-multiply the integrand by $e^{i\pi(\beta-\alpha)t^2}$ to cancel

the $e^{-i\pi(\beta-\alpha)t^2}$ term. Here we let $q(t) = e^{i\pi(\beta-\alpha)t^2}$ be the pre-multiplication waveform, then we have

$$\begin{aligned}\hat{O}(\tau,\nu) &= [s_{Recv}(t)q(t)] * \tilde{h}_{\tau\nu,\beta}(t)|_{t=T+\tau} \\ &= \sum_k a_k e^{-i\pi(\beta\tau^2-\alpha\tau_k^2)} \int_{-\infty}^{\infty} e^{-i2\pi[(\nu-\nu_k)-(\beta\tau-\alpha\tau_k)]t} 1_{[0,T]}(t-\tau_k)\cdot 1_{[0,T]}(t-\tau)dt \\ &= \sum_k a_k e^{-i\pi(\beta\tau^2-\alpha\tau_k^2)} e^{-i\pi[(\nu-\nu_k)-(\beta\tau-\alpha\tau_k)](T+\tau+\tau_k)} \cdot (T-|\tau-\tau_k|) \\ &\quad \cdot \operatorname{sinc}\left([(\nu-\nu_k)-(\beta\tau-\alpha\tau_k)]\,(T-|\tau-\tau_k|)\right)\cdot 1_{[0,T]}(|\tau-\tau_k|). \end{aligned} \tag{4.8}$$

For clarity, we can write (4.8) as

$$\hat{O}(\tau,\nu) = \sum_k \hat{O}_{\tau_k}(\tau,\nu),$$

where

$$\begin{aligned}\hat{O}_{\tau_k}(\tau,\nu) &= a_k e^{-i\pi(\beta\tau^2-\alpha\tau_k^2)} e^{-i\pi[(\nu-\nu_k)-(\beta\tau-\alpha\tau_k)](T+\tau+\tau_k)} \cdot (T-|\tau-\tau_k|) \\ &\quad \cdot \operatorname{sinc}\left([(\nu-\nu_k)-(\beta\tau-\alpha\tau_k)]\,(T-|\tau-\tau_k|)\right)\cdot 1_{[0,T]}(|\tau-\tau_k|). \end{aligned} \tag{4.9}$$

We know from (4.9) that $\hat{O}(\tau,\nu)$ is composed of K delay-Doppler responses $\hat{O}_{\tau_k}(\tau,\nu)$, where $k = 1,\cdots,K$, and each $\hat{O}_{\tau_k}(\tau,\nu)$ has a peak value at $(\tau_k, \nu_k+(\beta-\alpha)\tau_k)$ and a ridge with slope β. However, we know that in the matched filtering process, the k-th delay-Doppler output response, $\tilde{O}_{\mathrm{MF,k}}(\tau,\nu)$, has a peak value at (τ_k,ν_k), which is the k-th target's true delay and Doppler shift. The Doppler shift bias in the mismatched delay-Doppler response comes from the slope change of the ridge, which is due to the usage of a different chirp rate for the matching template signal. Therefore, to recover the mismatched output response back to the correct delay-Doppler positions, for any fixed delay τ_k, we apply a linear shift to $\hat{O}(\tau,\nu)$ in Doppler axis to correct the Doppler shift bias at the line $\tau=\tau_k$ from $\nu_k+(\beta-\alpha)\tau_k$ back to ν_k, i.e.,

$$\hat{O}_{\nu_{\mathrm{shift}}(\tau_k)}(\tau,\nu) = \hat{O}(\tau,\nu+(\beta-\alpha)\tau_k). \tag{4.10}$$

Then for each $\hat{O}_{\nu_{\mathrm{shift}}(\tau_k)}(\tau,\nu)$, the Doppler shift bias at the line $\tau=\tau_k$ is corrected.

Now, to keep all targets lying in the correct delay-Doppler positions, we can apply some operations to these responses $\hat{O}_{\nu_{\mathrm{shift}}(\tau_k)}(\tau,\nu)$, $k=1,2,\cdots$. The following

are two simple operations: i) point-wise selection of the maximum amplitude of these responses:

$$\hat{O}_{\max\{\nu_{\text{shift}}(\tau_k)\}}(\tau,\nu) = \max_k \left\{ |\hat{O}_{\nu_{\text{shift}}(\tau_k)}(\tau,\nu)| \right\}, k = 1, 2, \cdots, \tag{4.11}$$

and ii) summing over all $\hat{O}_{\nu_{\text{shift}}(\tau_k)}(\tau,\nu)$, $k = 1, 2, \cdots$. Then we get

$$\begin{aligned} \hat{O}_{\sum_k \nu_{\text{shift}}(\tau_k)}(\tau,\nu) &= \sum_k \hat{O}_{\nu_{\text{shift}}(\tau_k)}(\tau,\nu) \\ &= \sum_k \hat{O}(\tau, \nu + (\beta-\alpha)\tau_k). \end{aligned} \tag{4.12}$$

From the above two kinds of operations, we have the results $\hat{O}_{\max\{\nu_{\text{shift}}(\tau_k)\}}(\tau,\nu)$ and $\hat{O}_{\sum_k \nu_{\text{shift}}(\tau_k)}(\tau,\nu)$, which correct all Doppler positions in the lines $\tau = \tau_k$, $k = 1, 2, \cdots$. As a result, when the targets have delays at τ_k, $k = 1, 2, \cdots$, we can apply one of the above two operations to get the targets' true delay-Doppler positions. Furthermore, for the targets with delay and Doppler shift at (τ_k, ν_k), $k = 1, 2, \cdots$, the output responses $\hat{O}_{\max\{\nu_{\text{shift}}(\tau_k)\}}(\tau,\nu)$ and $\hat{O}_{\sum_k \nu_{\text{shift}}(\tau_k)}(\tau,\nu)$ have peak values at (τ_k, ν_k), $k = 1, 2, \cdots$, along with the ridges with slope β. We illustrate the two operations and show the output responses by applying an example as follows.

Figures 4.3, 4.4, 4.5 and 4.6 show an example to illustrate the process of combining correctly-shifted mismatched delay-Doppler responses. For the received waveform, two targets are at $(\tau_1, \nu_1) = (-0.3, 0.8)$ and $(\tau_2, \nu_2) = (0.7, -0.9)$, with the corresponding amplitudes 0.75 and 1.0. The transmitted chirp waveform has chirp rate $\alpha = 54.0$, and the mismatched filter applies a matching template signal with the chirp rate $\beta = -66.0$.

First of all, after the mismatched filtering and without any shift to the delay-Doppler response, two peaks are nearly at $(\tau_1^*, \nu_1^*) = (-0.3, 36.8)$ and $(\tau_2^*, \nu_2^*) = (0.7, -84.9)$, where $\nu_k^* = \nu_k + (\beta - \alpha)\tau_k$, $k = 1, 2$. Note that the two ridges have the same slope $\beta = -66.0$ in the delay-Doppler response. The output response is shown in Figure 4.3.

Now, to recover all targets' Doppler positions (in this case, we have two targets at two different delays, $\tau_1 = -0.3, \tau_2 = 0.7$), first we recover target 1's Doppler position

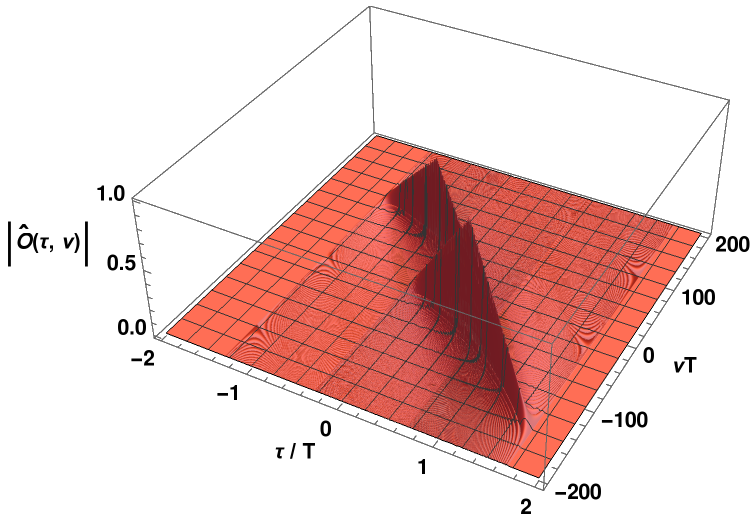

Fig. 4.3. Non-shifted mismatched filter delay-Doppler response. Two peaks are at $(\tau_1^*, \nu_1^*) = (-0.3, 36.8)$ and $(\tau_2^*, \nu_2^*) = (0.7, -84.9)$. The Doppler shift deviations of two targets are caused by the chirp rate difference between the transmitted waveform and the matching template signal.

by linear shifting the whole delay-Doppler response in Doppler axis, and the shifted bias is $-(\beta - \alpha)\tau_1 = -36.0$. By doing so, we can position target 1, which lies in $(\tau_1^*, \nu_1^*) = (-0.3, 36.8)$, back to the true position $(\tau_1, \nu_1) = (-0.3, 0.8)$. Similarly, to recover target 2's position, we shift the whole delay-Doppler response by the bias $-(\beta - \alpha)\tau_2 = 84.0$. Then target 2's position is corrected back to its true position $(\tau_2, \nu_2) = (0.7, -0.9)$. The shifted delay-Doppler responses with respect to target 1 and target 2 are shown in Figure 4.4 and 4.5.

However, from Figures 4.4 and 4.5, we can obviously see that because the linear shift operation to a delay-Doppler response can only correct one specific Doppler axis ($\tau = c, c$ is constant) at a time, the other targets which lie in different delays will linearly shift to other wrong Doppler positions. As a result, when we add $\nu(\tau_1)$-shifted and $\nu(\tau_2)$-shifted delay-Doppler responses together, two ghost ridges, which come from shifting $\nu(\tau_2)$ to target 1 and shifting $\nu(\tau_1)$ to target 2, will appear.

To keep all true targets positioning in the right delay-Doppler positions, we apply i) the combination of all $\nu(\tau_k)$-shifted responses or ii) point-wise selection of the

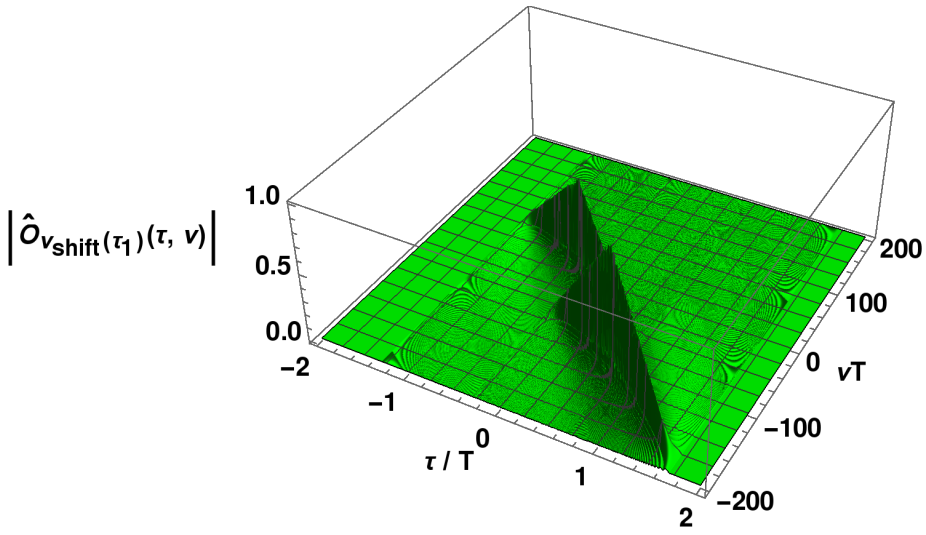

Fig. 4.4. The shifted delay-Doppler response with respect to target 1. The target 1's Doppler position is correctly shifted from $(\tau_1^*, \nu_1^*) = (-0.3, 36.8)$ back to $(\tau_1, \nu_1) = (-0.3, 0.8)$; however, target 2's position also shifted from $(\tau_2^*, \nu_2^*) = (0.7, -84.9)$ to $(\tau_2, \nu_2) = (0.7, -120.9)$.

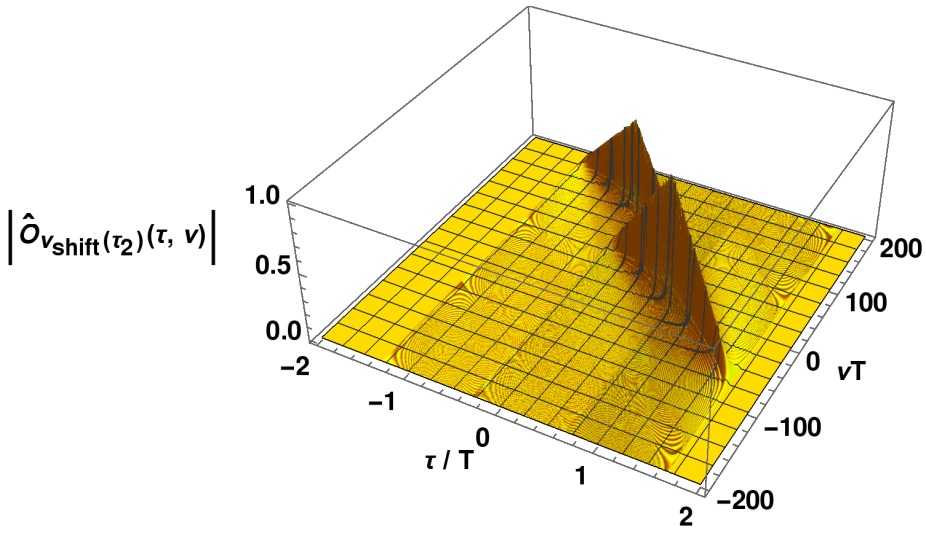

Fig. 4.5. The shifted delay-Doppler response with respect to target 2. Same as in Figure 4.4, the target 2's Doppler position is correctly shifted from $(\tau_2^*, \nu_2^*) = (0.7, -84.9)$ back to $(\tau_2, \nu_2) = (0.7, -0.9)$; however, target 1's position also shifted from $(\tau_1^*, \nu_1^*) = (-0.3, 36.8)$ to $(\tau_1, \nu_1) = (-0.3, 120.8)$.

maximum of all $\nu(\tau_k)$-shifted responses. In Figure 4.6(a) we add two shifted output

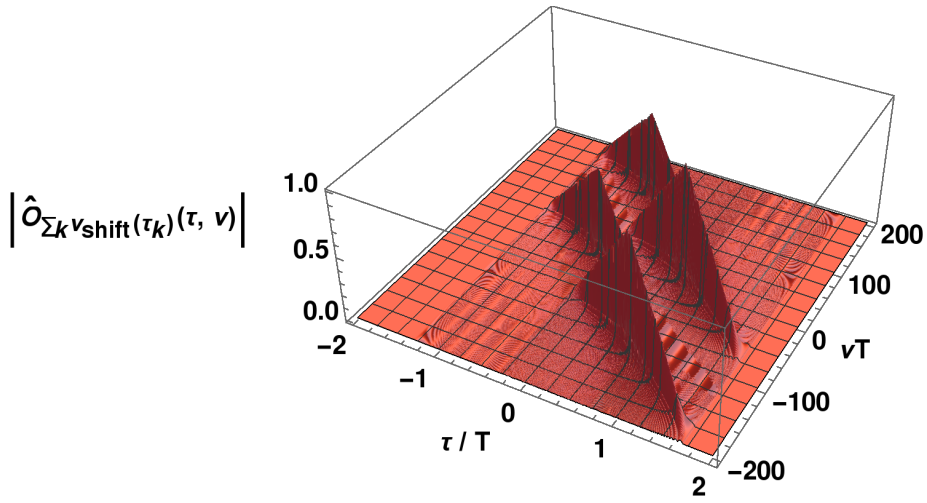

(a) Sum of two shifted delay-Doppler responses

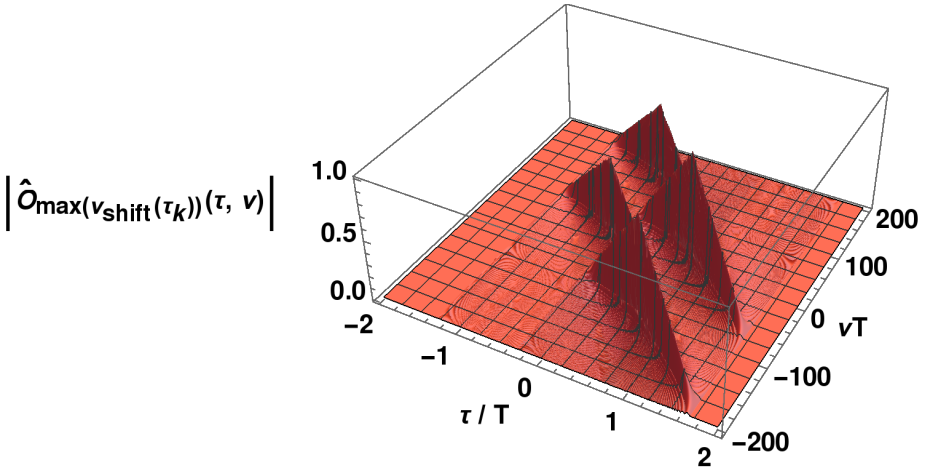

(b) Point-wise selection of the maximum of two shifted delay-Doppler responses

Fig. 4.6. (a) Sum of two shifted delay-Doppler responses (b) Point-wise selection of the maximum of two shifted delay-Doppler responses. Two peaks are at $(-0.3, 0.8)$ and $(0.7, -0.9)$, which are the two targets' true delay-Doppler positions. In addition, other two peaks at $(-0.3, 120.8)$ and $(0.7, -120.9)$ are the undesired ghost targets.

responses $\hat{O}_{\nu_{\text{shift}}(-0.3)}(\tau, \nu)$ and $\hat{O}_{\nu_{\text{shift}}(0.7)}(\tau, \nu)$. Also, in Figure 4.6(b) we point-wisely select the maximum amplitude of the two shifted output responses $\hat{O}_{\nu_{\text{shift}}(-0.3)}(\tau, \nu)$ and $\hat{O}_{\nu_{\text{shift}}(0.7)}(\tau, \nu)$. The results are shown in Figure 4.6.

Finally, due to the same delay and Doppler shift of each true target but with two different slopes of ridges in the matched filter output response and in the sum (max-

imum) of $\nu(\tau_k)$-shifted delay-Doppler responses, the two ridges only intersect at the target's true delay and Doppler shift for each target, i.e., (τ_k, ν_k), $k = 1, \cdots, K$, K is the total number of targets. Because of this, we can further apply some non-linear operations such as point-wise multiplication or point-wise selection of the minimum amplitude of the matched and the mismatched filter delay-Doppler responses. Then all of the targets' corresponding delay and Doppler positions can still keep high amplitudes, which is due to the high amplitude at (τ_k, ν_k) position in both the matched and mismatched delay-Doppler responses. However, for positions other than (τ_k, ν_k), only one of the two responses has higher amplitude or both responses have lower amplitudes, so after the non-linear operations, the (τ, ν) positions without any target have much smaller amplitudes, resulting in a better performance in terms of the larger signal to interference ratio. The following are two kinds of simple non-linear operations: i) point-wise multiplication of the matched and the sum (point-wise maximum) of shifted mismatched filter delay-Doppler responses:

$$\begin{aligned} \hat{O}_{\text{mult}}(\tau, \nu) &= \tilde{O}_{\text{MF}}(\tau, \nu) \cdot \hat{O}_{\sum_k \nu_{\text{shift}}(\tau_k)}(\tau, \nu) \\ \text{or } \hat{O}_{\text{mult}}(\tau, \nu) &= \tilde{O}_{\text{MF}}(\tau, \nu) \cdot \hat{O}_{\max\{\nu_{\text{shift}}(\tau_k)\}}(\tau, \nu), \end{aligned} \tag{4.13}$$

and ii) point-wise selection the minimum amplitude of the matched and the sum (point-wise maximum) of shifted mismatched filter delay-Doppler responses:

$$\begin{aligned} \hat{O}_{\min}(\tau, \nu) &= \min_{\tau,\nu} \left(\tilde{O}_{\text{MF}}(\tau, \nu), \hat{O}_{\sum_k \nu_{\text{shift}}(\tau_k)}(\tau, \nu) \right) \\ \text{or } \hat{O}_{\min}(\tau, \nu) &= \min_{\tau,\nu} \left(\tilde{O}_{\text{MF}}(\tau, \nu), \hat{O}_{\max\{\nu_{\text{shift}}(\tau_k)\}}(\tau, \nu) \right). \end{aligned} \tag{4.14}$$

Continuing with the previous example, we apply the above two non-linear operations and observe the resulting delay-Doppler responses. First, when we point-wisely multiply the matched filter output response and the sum (point-wise maximum) of shifted mismatched delay-Doppler responses, we have the resulting delay-Doppler response shown in Figure 4.7. Also, when we point-wisely select the minimum amplitude of the matched filter output response and the sum (point-wise maximum) of shifted mismatched delay-Doppler responses, we have the output delay-Doppler response shown

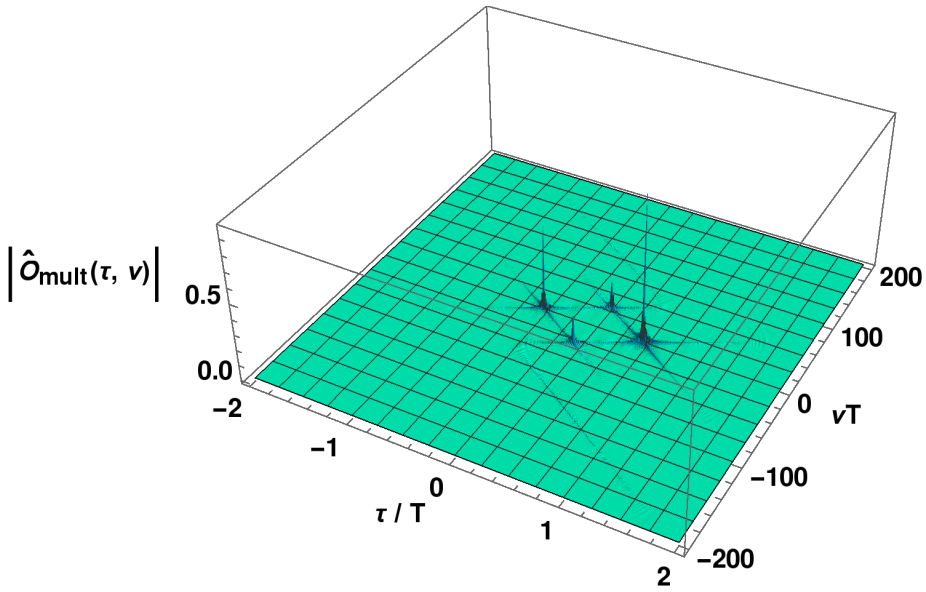

Fig. 4.7. The output response of point-wise multiplication between the chirp matched filter output response and the sum (point-wise maximum) of two shifted mismatched delay-Doppler responses with respect to target 1 and target 2.

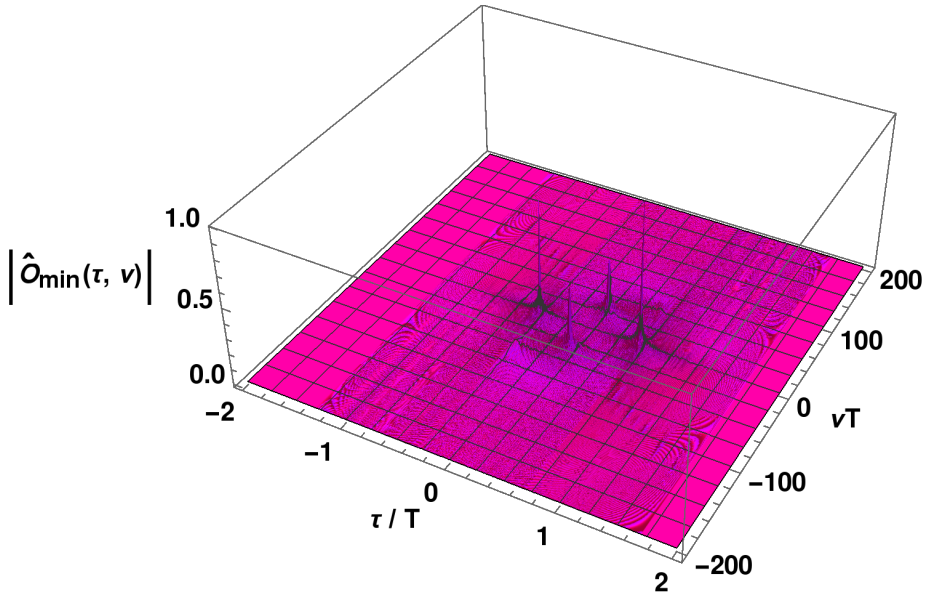

Fig. 4.8. The output response of point-wise selection of minimum amplitude between the chirp matched filter output response and the sum (point-wise maximum) of two Shifted mismatched delay-Doppler responses with respect to target 1 and target 2.

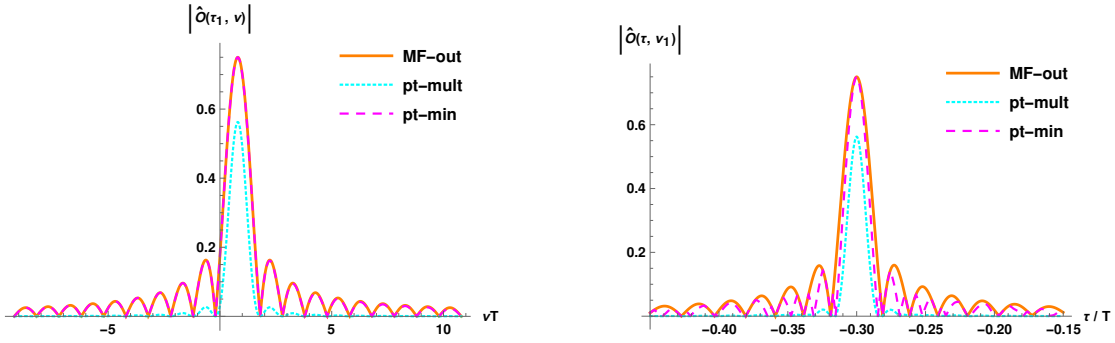

(a) τ_1-delay cut (b) ν_1-Doppler cut

Fig. 4.9. (a) τ_1-delay cut and (b) ν_1-Doppler cut comparisons at target 1 ($(\tau_1, \nu_1) = (-0.3, 0.8)$, amplitude=0.75). The matched filter output, the point-wise multiplication output and the point-wise selection of minimum amplitude output are compared.

in Figure 4.8. From Figures 4.7 and 4.8, we know that both of the above mentioned non-linear operations can sharpen the targets' delay-Doppler response width due to the operations on different ridge slopes in matched and mismatched filter output responses, thus causing much finer delay and Doppler resolutions. To further investigate the targets' delay-Doppler resolutions, we plot the zero-delay cut and zero-Doppler cut with respect to target 1 and target 2 in Figure 4.9 and 4.10. Note that target 1 is at (τ_1, ν_1) and target 2 is at (τ_2, ν_2), so the zero-delay cut of target 1 is the τ_1-delay cut of the delay-Doppler response, and the zero-Doppler cut of target 1 is the ν_1-Doppler cut of the delay-Doppler response. Likewise, for target 2, the zero-delay cut and the zero-Doppler cut are then the τ_2-delay cut and the ν_2-Doppler cut of the delay-Doppler response, respectively.

From Figures 4.9(a) and 4.10(a), we see that the three schemes have the same mainlobe width in the zero-delay cut. On the other hand, from Figures 4.9(b) and 4.10(b), we see that the point-wise multiplication and the point-wise minimum selection schemes have much sharper mainlobe widths than the mainlobe width of the matched filter in the zero-Doppler cut. Furthermore, both point-wise multiplication scheme and point-wise minimum selection scheme have the smaller amplitudes in sidelobes than the sidelobe amplitudes of the matched filter output, which shows higher

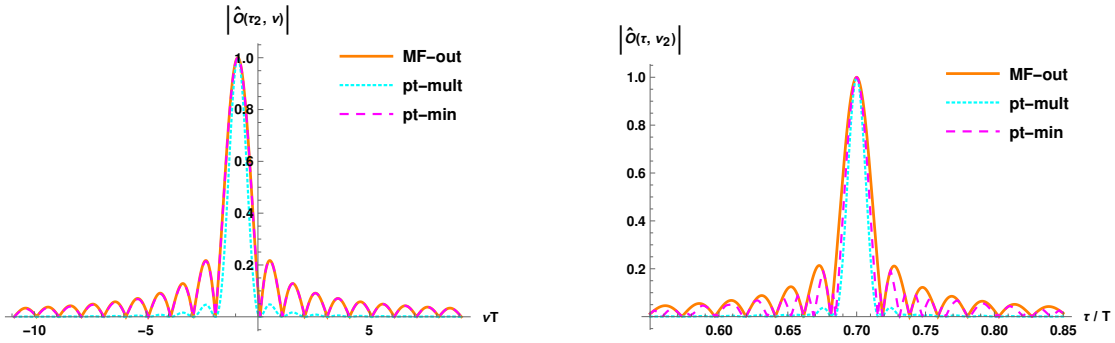

(a) τ_2-delay cut (b) ν_2-Doppler cut

Fig. 4.10. (a) τ_2-delay cut and (b) ν_2-Doppler cut comparisons at target 2 ($(\tau_2, \nu_2) = (0.7, -0.9)$, amplitude=1.0). The matched filter output, the point-wise multiplication output and the point-wise selection of minimum amplitude output are compared.

mainlobe to peak sidelobe ratio in both non-linear operation schemes. Therefore, non-linear operations obviously can improve the targets' delay resolution.

Even though there are advantages in terms of the improved delay-Doppler resolutions by applying the non-linear operations, we observe that two peaks other than the two true target returns show up in the delay-Doppler response in Figures 4.7 and 4.8. The two false peaks may cause problems in target detection. To further illustrate this problem, we analyze some properties of these false peaks in the following section.

4.3 Position and Amplitude Analysis of False Targets

In this section, we discuss about how false targets are generated when doing the above-mentioned mismatched filtering process, and we also provide detailed analyses of the targets' delay-Doppler positions as well as the targets' amplitudes.

Figure 4.11 is an example showing the overlapping plot of the matched filter output response and the sum (point-wise maximum) of shifted mismatched delay-Doppler responses, which are from the previous two-target example. To simplify the illustrations, we look the response from the top view and regard it as a two-dimensional plot (without the amplitude axis of the output responses), which only shows ridge slopes of the matched filtering response (with slope α) and ridge slopes of the sum (point-wise maximum) of shifted mismatched filtering responses (with slope β) in the delay-Doppler plane. Here we take a two-target case as an example. First of all, the matched filter output response has two targets at (τ_1, ν_1) and (τ_2, ν_2) with the slope α. Due to the limited duration of waveform transmission T and the duration of matching correlation, the ridges in each target can be seen as a line segment, i.e., at target (τ_1, ν_1), the ridge can be seen as a line segment from $(\tau_1 - T, \nu_1 - \alpha T)$ to $(\tau_1 + T, \nu_1 + \alpha T)$. Similarly, at target (τ_2, ν_2), the ridge can also be seen as a line segment from $(\tau_2 - T, \nu_2 - \alpha T)$ to $(\tau_2 + T, \nu_2 + \alpha T)$.

As for the mismatched filtering process, the output response shows that the two targets are at $(\tau_1, \nu_1 + (\beta - \alpha)\tau_1)$ and $(\tau_2, \nu_2 + (\beta - \alpha)\tau_2)$, both with the same slope

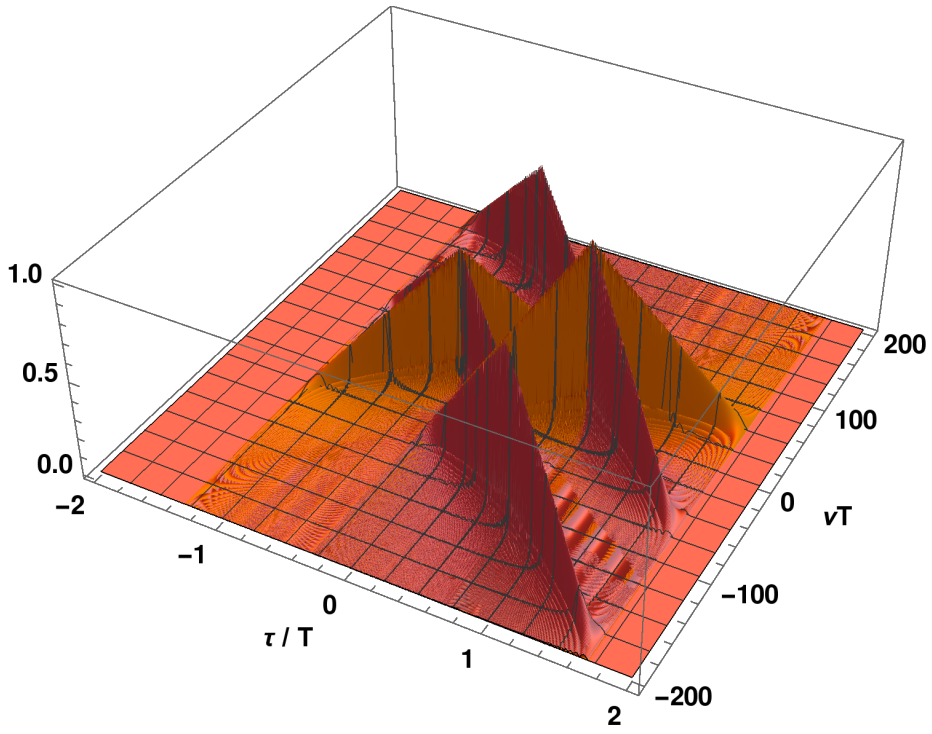

Fig. 4.11. Overlapping delay-Doppler output response of the matched filter output response and the sum (point-wise maximum) of shifted delay-Doppler responses with respect to target 1 and target 2.

β. Here we can easily see that applying different chirp template waveform in the mismatched filtering process will linearly shift the output response in the Doppler domain, and the shifted value is linearly related to the delay value and the chirp rate difference between the transmitted chirp signal and the chirp matching template signal. Now, to recover the shifts in the Doppler of the output response, first we shift the whole output response to match all Doppler positions at delay τ_1, then the target at (τ_1, ν_1) is corrected, and the other target response moves from $(\tau_2, \nu_2 + (\beta - \alpha)\tau_2)$ to $(\tau_2, \nu_2 + (\beta - \alpha)(\tau_2 - \tau_1))$. Just as in the previous discussions, the ridge of the target at (τ_1, ν_1) can be seen as a line segment from $(\tau_1 - T, \nu_1 - \beta T)$ to $(\tau_1 + T, \nu_1 + \beta T)$, and the ridge of target at $(\tau_2, \nu_2 + (\beta - \alpha)(\tau_2 - \tau_1))$ can also be seen as a line segment from $(\tau_2 - T, \nu_2 + (\beta - \alpha)(\tau_2 - \tau_1) - \beta T)$ to $(\tau_2 + T, \nu_2 + (\beta - \alpha)(\tau_2 - \tau_1) + \beta T)$. Likewise, when shifting the whole output response to match all Doppler positions at

delay τ_2, the target at (τ_2, ν_2) is then matched, and the other target response shifts from $(\tau_1, \nu_1 + (\beta - \alpha)\tau_1)$ to $(\tau_1, \nu_1 + (\beta - \alpha)(\tau_1 - \tau_2))$. Also, the ridge of the target at (τ_2, ν_2) can be seen as a line segment from $(\tau_2 - T, \nu_2 - \beta T)$ to $(\tau_2 + T, \nu_2 + \beta T)$, and the ridge of target at $(\tau_1, \nu_1 + (\beta - \alpha)(\tau_1 - \tau_2))$ can also be seen as a line segment from $(\tau_1 - T, \nu_1 + (\beta - \alpha)(\tau_1 - \tau_2) - \beta T)$ to $(\tau_1 + T, \nu_1 + (\beta - \alpha)(\tau_1 - \tau_2) + \beta T)$. Figure 4.12 shows how these line segments are generated in the process.

In the following subsections, we provide more detailed analyses of the targets' delay-Doppler positions and the targets' amplitudes.

4.3.1 Discussion of False Targets' Delay-Doppler Positions

Continuing the two-target example above, when the matched filter with chirp rate α is applied, the two-dimensional delay-Doppler plot has two line segments centering at (τ_1, ν_1), (τ_2, ν_2), both with slope α, which are the solid lines in Figure 4.12(a). We can write the two line segments as

$$\nu - \nu_1 = \alpha(\tau - \tau_1), \ |\tau - \tau_1| \leq T, \tag{4.15}$$

$$\nu - \nu_2 = \alpha(\tau - \tau_2), \ |\tau - \tau_2| \leq T. \tag{4.16}$$

Likewise, when a mismatched filter with chirp rate β is applied, the two-dimensional delay-Doppler plot has two line segments centering at $(\tau_1, \nu_1 + (\beta - \alpha)\tau_1)$, $(\tau_2, \nu_2 + (\beta - \alpha)\tau_2)$, and both with slope β. Then after shifting to match the delay and Doppler positions of target 1, the two-dimensional delay-Doppler plot has two line segments centering at (τ_1, ν_1), $(\tau_2, \nu_2 + (\beta - \alpha)(\tau_2 - \tau_1))$, and both with slope β. We can write the two line segments as

$$\nu - \nu_1 = \beta(\tau - \tau_1), \ |\tau - \tau_1| \leq T, \tag{4.17}$$

$$\nu - \nu_2 = (\beta - \alpha)(\tau_2 - \tau_1) + \beta(\tau - \tau_2), \ |\tau - \tau_2| \leq T. \tag{4.18}$$

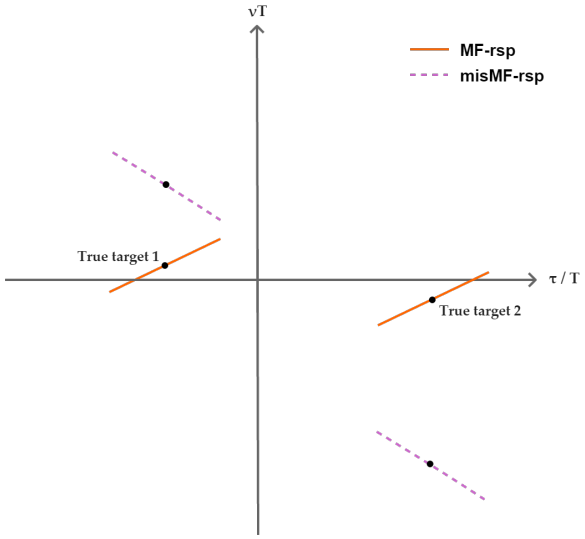

(a)

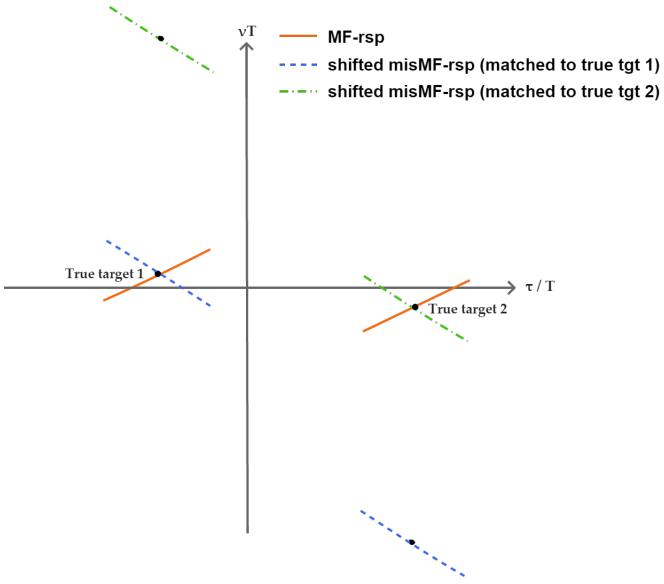

(b)

Fig. 4.12. Demonstrations about the linear shifting process of a mismatched filter response. (a) the matched filter response (solid) and the non-shifted mismatched filter response (dashed). (b) the matched filter response (solid) and two linearly-shifted mismatched filter responses, matching to the target 1 and the target 2 respectively (dashed).

Just as in the above process, when the mismatched output response shifts to match target 2, we have

$$\nu - \nu_1 = (\beta - \alpha)(\tau_1 - \tau_2) + \beta(\tau - \tau_1), \ |\tau - \tau_1| \leq T, \tag{4.19}$$

$$\nu - \nu_2 = \beta(\tau - \tau_2), \ |\tau - \tau_2| \leq T. \tag{4.20}$$

Now we regard the line segments as lines first and solve these linear equations to find positions of true targets and false targets. We have

$$
\begin{aligned}
&\text{eq.}(4.15),(4.17) : (\tau,\nu) = (\tau_1,\nu_1)\\
&\text{eq.}(4.15),(4.18) : (\tau,\nu) =\\
&\left(\tau_1 + \frac{\alpha}{\alpha-\beta}(\tau_1-\tau_2) + \frac{1}{\alpha-\beta}(\nu_2-\nu_1), \nu_1 + \frac{\alpha}{\alpha-\beta}(\nu_2-\nu_1) + \frac{\alpha^2}{\alpha-\beta}(\tau_1-\tau_2)\right)\\
&\text{eq.}(4.15),(4.19) : (\tau,\nu) = (\tau_2, \nu_1 + \alpha(\tau_2-\tau_1))\\
&\text{eq.}(4.15),(4.20) : (\tau,\nu) =\\
&\left(\tau_1 + \frac{\beta}{\alpha-\beta}(\tau_1-\tau_2) + \frac{1}{\alpha-\beta}(\nu_2-\nu_1), \nu_2 + \frac{\beta}{\alpha-\beta}(\nu_2-\nu_1) + \frac{\alpha\beta}{\alpha-\beta}(\tau_1-\tau_2)\right)\\
&\text{eq.}(4.16),(4.17) : (\tau,\nu) =\\
&\left(\tau_2 + \frac{\beta}{\alpha-\beta}(\tau_2-\tau_1) + \frac{1}{\alpha-\beta}(\nu_1-\nu_2), \nu_1 + \frac{\beta}{\alpha-\beta}(\nu_1-\nu_2) + \frac{\alpha\beta}{\alpha-\beta}(\tau_2-\tau_1)\right)\\
&\text{eq.}(4.16),(4.18) : (\tau,\nu) = (\tau_1, \nu_2 + \alpha(\tau_1-\tau_2))\\
&\text{eq.}(4.16),(4.19) : (\tau,\nu) =\\
&\left(\tau_2 + \frac{\alpha}{\alpha-\beta}(\tau_2-\tau_1) + \frac{1}{\alpha-\beta}(\nu_1-\nu_2), \nu_2 + \frac{\alpha}{\alpha-\beta}(\nu_1-\nu_2) + \frac{\alpha^2}{\alpha-\beta}(\tau_2-\tau_1)\right)\\
&\text{eq.}(4.16),(4.20) : (\tau,\nu) = (\tau_2,\nu_2). \qquad (4.21)
\end{aligned}
$$

In general, when two targets' delay and Doppler differences $|\tau_1-\tau_2|$, $|\nu_1-\nu_2|$ are moderately large, to let the false targets from the intersections of eq.(4.15), (4.19) and eq.(4.16), (4.18) lie in the sufficiently large Doppler shift ν (out of the range of interest), we control the chirp rate α and make $|\alpha|$ sufficiently large. Furthermore, when $|\alpha|$ is set to be a larger value, we can also control the chirp rate of the matching template signal β such that $|\alpha-\beta|$ is small, then the false targets from the intersections of eq.(4.15), (4.18), eq.(4.15), (4.20), eq.(4.16), (4.17) and eq.(4.16), (4.19) can also lie at sufficiently large Doppler shifts such that these Doppler shifts are out of the range of interest. To further investigate the false target positions, we consider four different cases for illustrations.

Two Targets with the Same Delay

When two targets have the same delay but with different Doppler shifts, i.e., $|\tau_2 - \tau_1| = 0$ and $|\nu_2 - \nu_1| \neq 0$, the equations in (4.21) become

$$\begin{aligned}
&\text{eq.}(4.15), (4.17) : (\tau, \nu) = (\tau_1, \nu_1) \\
&\text{eq.}(4.15), (4.18) : (\tau, \nu) = \left(\tau_1 + \frac{1}{\alpha - \beta}(\nu_2 - \nu_1), \nu_1 + \frac{\alpha}{\alpha - \beta}(\nu_2 - \nu_1)\right) \\
&\text{eq.}(4.15), (4.19) : (\tau, \nu) = (\tau_1, \nu_1) \\
&\text{eq.}(4.15), (4.20) : (\tau, \nu) = \left(\tau_1 + \frac{1}{\alpha - \beta}(\nu_2 - \nu_1), \nu_2 + \frac{\beta}{\alpha - \beta}(\nu_2 - \nu_1)\right) \\
&\text{eq.}(4.16), (4.17) : (\tau, \nu) = \left(\tau_1 + \frac{1}{\alpha - \beta}(\nu_1 - \nu_2), \nu_1 + \frac{\beta}{\alpha - \beta}(\nu_1 - \nu_2)\right) \\
&\text{eq.}(4.16), (4.18) : (\tau, \nu) = (\tau_1, \nu_2) \\
&\text{eq.}(4.16), (4.19) : (\tau, \nu) = \left(\tau_1 + \frac{1}{\alpha - \beta}(\nu_1 - \nu_2), \nu_2 + \frac{\alpha}{\alpha - \beta}(\nu_1 - \nu_2)\right) \\
&\text{eq.}(4.16), (4.20) : (\tau, \nu) = (\tau_1, \nu_2). \qquad (4.22)
\end{aligned}$$

Obviously, we can see that when $|\alpha|$, $|\beta|$ are large, and $|\alpha - \beta|$ is small, all the false targets will lie outside the range of interest in Doppler shift, and only the true targets will remain.

Two Targets with the Same Doppler Shift

When two targets have the same Doppler shift but with different delays, i.e., $|\tau_2 - \tau_1| \neq 0$ and $|\nu_2 - \nu_1| = 0$, the equations in (4.21) become

$$\begin{aligned}
&\text{eq.}(4.15), (4.17) : (\tau, \nu) = (\tau_1, \nu_1) \\
&\text{eq.}(4.15), (4.18) : (\tau, \nu) = \left(\tau_1 + \frac{\alpha}{\alpha - \beta}(\tau_1 - \tau_2), \nu_1 + \frac{\alpha^2}{\alpha - \beta}(\tau_1 - \tau_2)\right) \\
&\text{eq.}(4.15), (4.19) : (\tau, \nu) = (\tau_2, \nu_1 + \alpha(\tau_2 - \tau_1)) \\
&\text{eq.}(4.15), (4.20) : (\tau, \nu) = \left(\tau_1 + \frac{\beta}{\alpha - \beta}(\tau_1 - \tau_2), \nu_1 + \frac{\alpha\beta}{\alpha - \beta}(\tau_1 - \tau_2)\right) \\
&\text{eq.}(4.16), (4.17) : (\tau, \nu) = \left(\tau_2 + \frac{\beta}{\alpha - \beta}(\tau_2 - \tau_1), \nu_1 + \frac{\alpha\beta}{\alpha - \beta}(\tau_2 - \tau_1)\right) \\
&\text{eq.}(4.16), (4.18) : (\tau, \nu) = (\tau_1, \nu_1 + \alpha(\tau_1 - \tau_2)) \\
&\text{eq.}(4.16), (4.19) : (\tau, \nu) = \left(\tau_2 + \frac{\alpha}{\alpha - \beta}(\tau_2 - \tau_1), \nu_1 + \frac{\alpha^2}{\alpha - \beta}(\tau_2 - \tau_1)\right) \\
&\text{eq.}(4.16), (4.20) : (\tau, \nu) = (\tau_2, \nu_1). \qquad (4.23)
\end{aligned}$$

As in the previous case, when $|\alpha|, |\beta|$ are large and $|\alpha - \beta|$ is small, all the false targets will lie outside the range of interest in Doppler shift, and only the true targets will remain.

Two Targets Lie in a Line with Slope β

When two targets lie in the delay-Doppler plane with slope β, i.e., the first target is at (τ_1, ν_1) and the second target is at $(\tau_1+\Delta, \nu_1+\beta\Delta)$, then the equations in (4.21) become

$$\begin{aligned}
&\text{eq.}(4.15), (4.17) : (\tau, \nu) = (\tau_1, \nu_1) \\
&\text{eq.}(4.15), (4.18) : (\tau, \nu) = (\tau_1 - \Delta, \nu_1 - \alpha\Delta) \\
&\text{eq.}(4.15), (4.19) : (\tau, \nu) = (\tau_1 + \Delta, \nu_1 + \alpha\Delta) \\
&\text{eq.}(4.15), (4.20) : (\tau, \nu) = (\tau_1, \nu_1) \\
&\text{eq.}(4.16), (4.17) : (\tau, \nu) = (\tau_1 + \Delta, \nu_1 + \beta\Delta) \\
&\text{eq.}(4.16), (4.18) : (\tau, \nu) = (\tau_1, \nu_1 + (\beta - \alpha)\Delta) \\
&\text{eq.}(4.16), (4.19) : (\tau, \nu) = (\tau_1 + 2\Delta, \nu_1 + (\alpha + \beta)\Delta) \\
&\text{eq.}(4.16), (4.20) : (\tau, \nu) = (\tau_1 + \Delta, \nu_1 + \beta\Delta). \qquad (4.24)
\end{aligned}$$

In this case, there are four false targets with four different Doppler shifts, $\nu_1 - \alpha\Delta$, $\nu_1 + \alpha\Delta$, $\nu_1 + (\beta - \alpha)\Delta$, and $\nu_1 + (\beta + \alpha)\Delta$. In general, we would like these four false target Doppler shifts to be significantly different from target 1's Doppler ν_1 and target 2's Doppler $\nu_1 + \beta\Delta$ to push the false targets out of the range of interest. So, under a specific minimum target separation requirement, Δ, we can control α, β to let $\nu_1 + \min_{\alpha,\beta}(|\alpha\Delta|, |(\beta - \alpha)\Delta|, |(\beta + \alpha)\Delta|)$ be out of the Doppler range of interest, then the false targets can be removed.

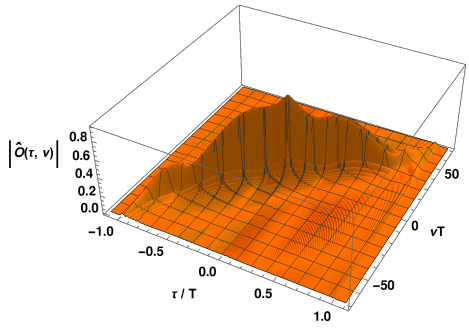

(a) Matched filter response

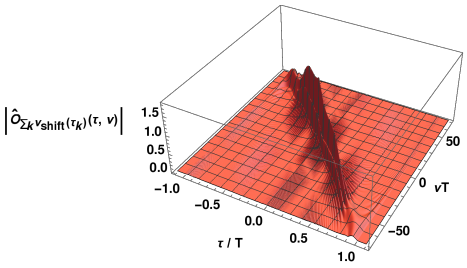

(b) Sum of two shifted mismatched filter responses

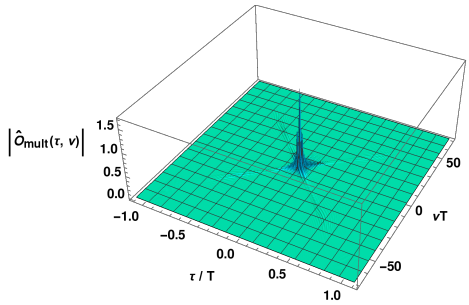

(c) Point-wise multiplication response (zoom-out view)

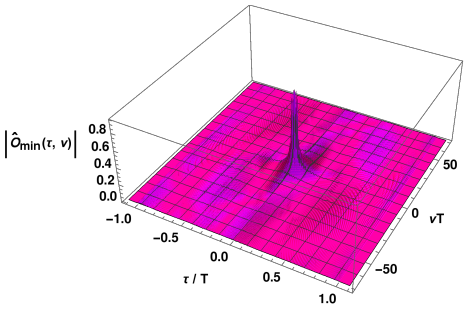

(d) Point-wise minimum selection response (zoom-out view)

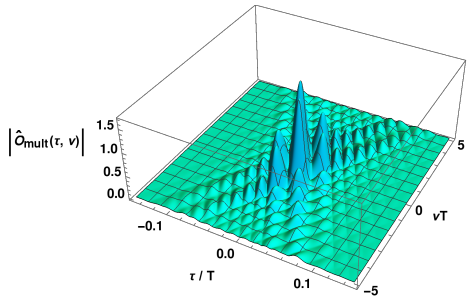

(e) Point-wise multiplication response (zoom-in view)

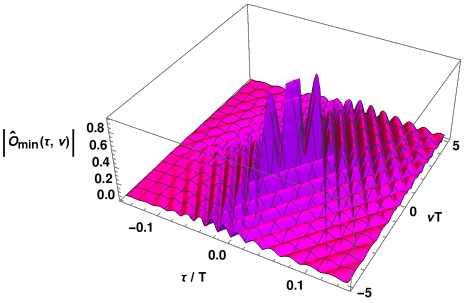

(f) Point-wise minimum selection response (zoom-in view)

Fig. 4.13. An example of two targets lying in a line with slope $\beta = -66.0$. Target 1 is at $(\tau_1, \nu_1) = (0.0075749, -0.499943)$, and target 2 is at $(\tau_2, \nu_2) = (-0.0075749, 0.499943)$. The distance between the two targets is 1.0, which equals to the signal duration T. (Note: $|d_{\text{delay}}| = 0.0151497$, $|d_{\text{Doppler}}| = 0.0151497 * |\beta| = 0.99988$)

Two Targets Lie in a Line with Slope α

When two targets lie in the delay-Doppler plane with the slope α, i.e., the first target is at (τ_1, ν_1) and the second target is at $(\tau_1 + \Delta, \nu_1 + \alpha\Delta)$, then the equations in (4.21) become

$$\begin{aligned}
&\text{eq.}(4.15), (4.17) : (\tau, \nu) = (\tau_1, \nu_1) \\
&\text{eq.}(4.15), (4.18) : (\tau, \nu) = (\tau_1, \nu_1) \\
&\text{eq.}(4.15), (4.19) : (\tau, \nu) = (\tau_1 + \Delta, \nu_1 + \alpha\Delta) \\
&\text{eq.}(4.15), (4.20) : (\tau, \nu) = (\tau_1 + \Delta, \nu_1 + \alpha\Delta) \\
&\text{eq.}(4.16), (4.17) : (\tau, \nu) = (\tau_1, \nu_1) \\
&\text{eq.}(4.16), (4.18) : (\tau, \nu) = (\tau_1, \nu_1) \\
&\text{eq.}(4.16), (4.19) : (\tau, \nu) = (\tau_1 + \Delta, \nu_1 + \alpha\Delta) \\
&\text{eq.}(4.16), (4.20) : (\tau, \nu) = (\tau_1 + \Delta, \nu_1 + \alpha\Delta). \qquad (4.25)
\end{aligned}$$

Actually, when the two targets are at (τ_1, ν_1) and $(\tau_1 + \Delta, \nu_1 + \alpha\Delta)$, (4.17) and (4.18) are equivalent, (4.19) and (4.20) are also equivalent. So the intersections of all pairs of equations are at (τ_1, ν_1) and $(\tau_1 + \Delta, \nu_1 + \alpha\Delta)$, corresponding to the delay and Doppler shifts of the two true targets. Therefore, no false target is generated in this case. We can easily see from Figure 4.14(a) that when the received waveform goes through the matched filtering process, the delay-Doppler response has two partially overlapping ridges with the same slope α when the two targets' absolute delay difference $|\Delta| < 2T$. However, from Figure 4.14(b) we see that when the received waveform goes through the mismatched filtering process, the delay-Doppler response has two parallel ridges with the same slope β even when the two targets' absolute delay difference becomes really small. Therefore, finding intersections of lines in (4.21) is reduced to finding intersections of the three lines left, and all the intersections are the true targets' delay-Doppler positions.

From the above four cases, we know that the positions of all false targets can be decided by solving the linear equations in (4.21). Therefore, by appropriately

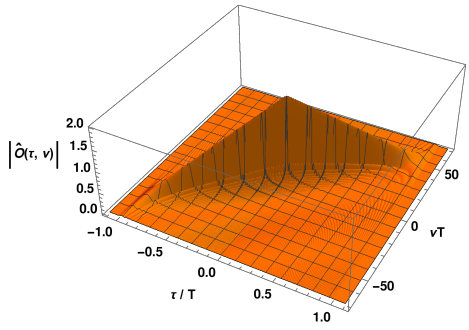

(a) Matched filter response

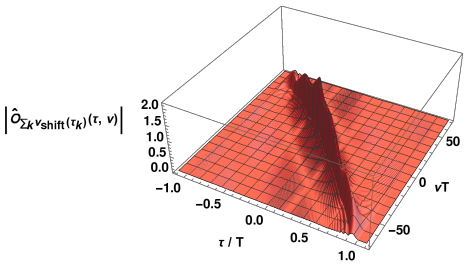

(b) Sum of two shifted mismatched filter responses

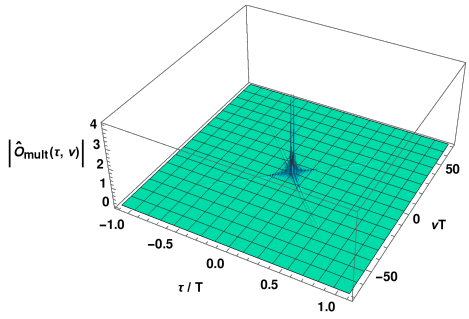

(c) Point-wise multiplication response (zoom-out view)

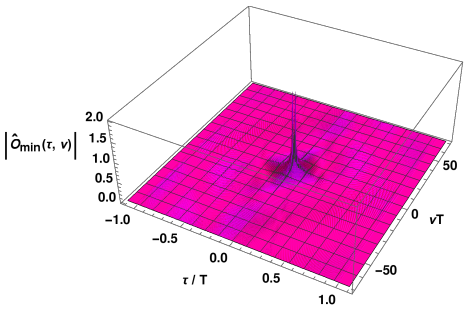

(d) Point-wise minimum selection response (zoom-out view)

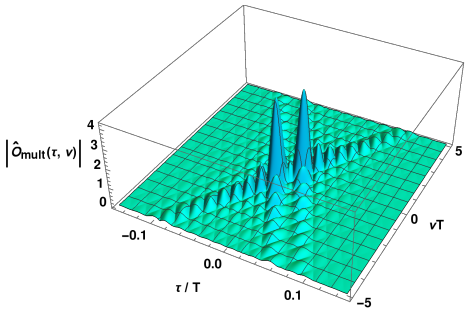

(e) Point-wise multiplication response (zoom-in view)

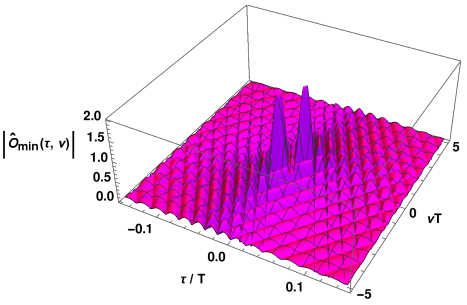

(f) Point-wise minimum selection response (zoom-in view)

Fig. 4.14. An example of two targets lying in a line with the slope $\alpha = 54.0$. Target 1 is at $(\tau_1, \nu_1) = (0.0092576, 0.499913)$, and target 2 is at $(\tau_2, \nu_2) = (-0.0092576, -0.499913)$. The distance between the two targets is 1.0, which equals to the signal duration T. (Note: $|d_{\text{delay}}| = 0.0185153$, $|d_{\text{Doppler}}| = 0.0185153 * |\alpha| = 0.99982$)

controlling the chirp rates of the transmitted waveform and the matching template waveform, we can design a radar system which not only has a better resolution in delay-Doppler response but moves false targets out of the delay-Doppler range of interest. Especially in the last case, we can not differentiate two spatially close targets from the chirp matched filter output response because of the partial overlap in two targets' response. However, the above-mentioned mismatched filter can easily solve this problem by rotating the slope of ridges in the target output response, and the enhanced delay-Doppler resolutions can be achieved.

4.3.2 Discussion of False Targets' Amplitudes

From the previous derivations about the delay-Doppler responses of the chirp matched filter and the chirp mismatched filter, we know that any target in the delay-Doppler plane has a ridge with a slope which is equivalent to the chirp rate of the matching template signal in the receive filter. Furthermore, the amplitude along the ridge linearly attenuates with the delay difference, i.e., $T - |\tau|$. Due to the waveform duration T in a chirp pulse, the waveform correlations only has the output when $\tau \in [-T, T]$. Moreover, target positions are the ridge intersections from the chirp matched filter output and from the sum (point-wise maximum) of shifted mismatched filter output responses, so a false target's amplitude is fully decided by the delay difference between the position of intersection and the two peaks of the intersected ridges, and by the peak amplitudes of the two intersected ridges. To be more specific, we assume that two true targets are at (τ_1, ν_1) and (τ_2, ν_2), and the two targets have the corresponding peak amplitudes a_1 and a_2. We further assume that the two true targets' ridges intersect at (τ^*, ν^*). Now, when τ^* lies within the delay interval $[\max(\tau_1, \tau_2) - T, \min(\tau_1, \tau_2) + T]$, a false target will be generated, and the amplitude of the false target is

$$\min\big(a_1(T - |\tau^* - \tau_1|), a_2(T - |\tau^* - \tau_2|)\big)$$

when the point-wise selection of the minimum amplitude is applied as the non-linear operation in the mismatched filter. Likewise, when we use the point-wise multiplication of two amplitudes to be the non-linear operation in the mismatched filter, then the false target's amplitude is

$$a_1(T - |\tau^* - \tau_1|) * a_2(T - |\tau^* - \tau_2|).$$

In the following we apply the two target example described in section II to further illustrate the false target's amplitude. The point-wise selection of the minimum amplitude is applied as the non-linear operation in the mismatched filter.

Now we discuss the false targets' amplitudes in the example described in section II. Two true targets are at $(\tau_1, \nu_1) = (-0.3, 0.8)$ and $(\tau_2, \nu_2) = (0.7, -0.9)$, with the corresponding amplitudes 0.75 and 1.0. The matching template in the matched filter has the chirp rate $\alpha = 54.0$, and the matching template in the mismatched filter has the chirp rate $\beta = -66.0$. By applying the above parameters into (4.21), we have the targets' delay-Doppler positions as follows:

$$(\tau, \nu) = (-0.3, 0.8)$$
$$(\tau, \nu) = (-0.764, -24.265)$$
$$(\tau, \nu) = (0.7, 54.8)$$
$$(\tau, \nu) = (0.236, 29.735)$$
$$(\tau, \nu) = (0.164, -29.835)$$
$$(\tau, \nu) = (-0.3, -54.9)$$
$$(\tau, \nu) = (1.164, 24.165)$$
$$(\tau, \nu) = (0.7, -0.9).$$

The first one and the last one are the two true targets' delay-Doppler positions, i.e., $(\tau_1, \nu_1) = (-0.3, 0.8)$ and $(\tau_2, \nu_2) = (0.7, -0.9)$, and the other six intersections are the false targets' positions. Now we let

$$\begin{aligned}
(\tau_{f_1}, \nu_{f_1}) &= (-0.764, -24.265) \\
(\tau_{f_2}, \nu_{f_2}) &= (0.7, 54.8) \\
(\tau_{f_3}, \nu_{f_3}) &= (0.236, 29.735) \\
(\tau_{f_4}, \nu_{f_4}) &= (0.164, -29.835) \\
(\tau_{f_5}, \nu_{f_5}) &= (-0.3, -54.9) \\
(\tau_{f_6}, \nu_{f_6}) &= (1.164, 24.165),
\end{aligned}$$

then for false target f_1, $(\tau_{f_1}, \nu_{f_1}) = (-0.764, -24.265)$, which lies outside the delay interval $[\max(\tau_1, \tau_2) - T, \min(\tau_1, \tau_2) + T] = [\tau_2 - T, \tau_1 + T] = [-0.3, 0.7]$. So the intersection is the extension of the line segments, then false target f_1 can not be generated in reality. Likewise, false target f_6, which lies at $(\tau_{f_6}, \nu_{f_6}) = (1.164, 24.165)$, also can not be generated.

For false target f_2, $(\tau_{f_2}, \nu_{f_2}) = (0.7, 54.8)$, and the amplitude is

$$\begin{aligned}
|\hat{O}_{\min}(\tau_{f_2}, \nu_{f_2})| &= \min\Big(0.75(T - |\tau_{f_2} - \tau_1|), 1.0(T - |\tau_{f_2} - \tau_2|)\Big) \\
&= \min\Big(0.75(T - |0.7 - (-0.3)|), 1.0(T - |0.7 - 0.7|)\Big) \\
&= \min\Big(0.75(T - 1), 1.0(T - 0)\Big) \\
&= \min(0, 1) \\
&= 0.
\end{aligned}$$

Note that $T = 1.0$ is the pulse duration. Therefore, false target f_2 is with amplitude 0. Likewise, for false target f_5, $(\tau_{f_5}, \nu_{f_5}) = (-0.3, -54.9)$, the amplitude is

$$\begin{aligned}
|\hat{O}_{\min}(\tau_{f_5}, \nu_{f_5})| &= \min\Big(0.75(T - |\tau_{f_5} - \tau_1|), 1.0(T - |\tau_{f_5} - \tau_2|)\Big) \\
&= \min\Big(0.75(T - |-0.3 - (-0.3)|), 1.0(T - |-0.3 - 0.7|)\Big) \\
&= \min\Big(0.75(T - 0), 1.0(T - 1)\Big) \\
&= \min(0.75, 0) \\
&= 0.
\end{aligned}$$

Therefore, false target f_5 also has amplitude 0.

Now, for false target f_3, $(\tau_{f_3}, \nu_{f_3}) = (0.236, 29.735)$, and the amplitude is

$$\begin{aligned}
|\hat{O}_{\min}(\tau_{f_3}, \nu_{f_3})| &= \min\Big(0.75(T - |\tau_{f_3} - \tau_1|), 1.0(T - |\tau_{f_3} - \tau_2|)\Big) \\
&= \min\Big(0.75(T - |0.236 - (-0.3)|), 1.0(T - |0.236 - 0.7|)\Big) \\
&= \min\Big(0.75(T - 0.536), 1.0(T - 0.464)\Big) \\
&= \min(0.348, 0.536) \\
&= 0.348.
\end{aligned}$$

So false target f_3 has the amplitude $|\hat{O}_{\min}(\tau_{f_3}, \nu_{f_3})| = 0.348$. Likewise, for false target f_4, $(\tau_{f_4}, \nu_{f_4}) = (0.164, -29.835)$, and the amplitude is

$$\begin{aligned}
|\hat{O}_{\min}(\tau_{f_4}, \nu_{f_4})| &= \min\Big(0.75(T - |\tau_{f_4} - \tau_1|), 1.0(T - |\tau_{f_4} - \tau_2|)\Big) \\
&= \min\Big(0.75(T - |0.164 - (-0.3)|), 1.0(T - |0.164 - 0.7|)\Big) \\
&= \min\Big(0.75(T - 0.464), 1.0(T - 0.536)\Big) \\
&= \min(0.402, 0.464) \\
&= 0.402.
\end{aligned}$$

Therefore, false target f_4 has the amplitude $|\hat{O}_{\min}(\tau_{f_4}, \nu_{f_4})| = 0.402$. The positions and amplitudes of false target f_3 and f_4 are shown in Figure 4.8.

From the example we know that the false targets' delay-Doppler positions and the amplitudes can be fully determined once we know the true targets' delay-Doppler positions and the amplitudes.

4.4 Minimum Resolvable Target Separation

In this section, we would like to investigate how close the two targets can be and we still can discriminate them. For simplicity, we discuss a two-target case only, and this case can be extended to any pair of targets. Now, based on the difficulty in resolving two close targets lying in the line with the slope α, the chirp rate of the transmitted waveform, in the chirp matched delay-Doppler response, in the following we apply the hybrid filter in this scenario to deal with this problem and see how close in delay and Doppler the two targets can be and we still have a successful discrimination.

Figures 4.15 to 4.22 show the hybrid filter output responses with eight different β values, 50.0, 10.0, 5.0, 1.0, -1.0, -5.0, -10.0 and -50.0. Here we let $\alpha = 10.0$ be the chirp rate of the transmitted signal for all cases. Furthermore, the point-wise selection of the minimum amplitude is applied in the nonlinear operation. And, in each case, the responses of four different distances are compared, and the distance between the two targets, d, is defined as

$$\begin{aligned} d &= \sqrt{d_{\text{delay}}^2 + d_{\text{Doppler}}^2} \\ &= \sqrt{(\frac{\Delta\tau}{T})^2 + (\Delta\nu T)^2}. \end{aligned} \tag{4.26}$$

In Figure 4.15, $\beta/\alpha = 5.0$, we can see that the two targets cannot be differentiated when $d = 0.125$. Then in Figure 4.16, $\beta/\alpha = 1.0$, which is the matched filter case, the two targets can not be differentiated even when $d = 1.0$. Also, in Figure 4.17, $\beta/\alpha = 0.5$, the two targets can not be differentiated when $d = 1.0$. In Figure 4.18, $\beta/\alpha = 0.1$, the two targets can not be differentiated when $d = 0.5$. Also in Figure 4.19, $\beta/\alpha = -0.1$, the two targets can not be differentiated when $d = 0.5$. In Figure 4.20, $\beta/\alpha = -0.5$, the two targets can not be differentiated when $d = 0.25$. Then in

Figure 4.21, $\beta/\alpha = -1.0$, the two targets can not be differentiated when $d = 0.25$. Finally, in Figure 4.22, $\beta/\alpha = -5.0$, the two targets can be differentiated even when $d = 0.125$. Table 4.1 shows the above observations.

Table 4.1. Minimum separable distance between two targets from Figures 4.15 to 4.22. Four different distances (1.0, 0.5, 0.25, 0.125) are compared.

β/α	5.0	1.0	0.5	0.1	-0.1	-0.5	-1.0	-5.0
Minimum Separable Distance	0.25	none	none	1.0	1.0	0.5	0.5	0.125

From Table 4.1 we know that when α and β are with different signs and β/α gets larger, the ability in target discrimination becomes better. Therefore, we have the following conclusions:

I) The high delay-Doppler resolutions come from the fact that two different ridge slopes at the same target's delay-Doppler positions, and when the two ridge slopes differs more, the mutual interference along the ridge gets smaller, then the target discrimination ability can be improved.

II) No matter what the values of α and β are, when β/α gets much farther away from 1.0, by doing the nonlinear operation then we can have much finer delay-Doppler resolutions.

III) We can regard the unmodulated rectangular pulse as the chirp waveform with $\alpha = 0$, and it is easy to see that for any chirp waveform with the chirp rate α, the matched filter output response has a triangular shape along the ridge of slope α, thus causing a bad ridge resolution. We can know the bad ridge resolution comes from by the equation 4.8.

4.5 Signal to Noise Ratio Analysis of the Mismatched Filter Output

Figure 4.1 is the chirp hybrid receiver structure combined by a matched filter (upper part) and a mismatched filter (lower part). For the mismatched filtering

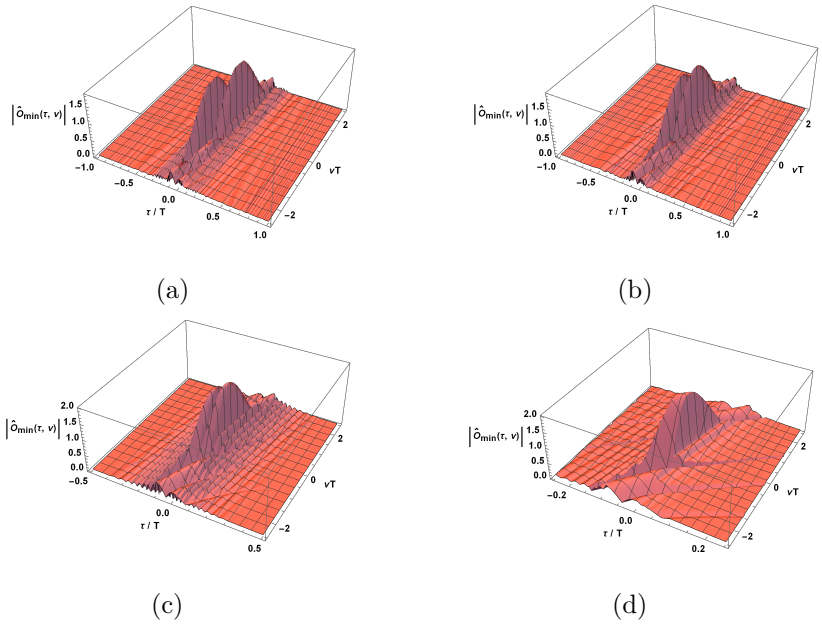

Fig. 4.15. The mismatched filter output response of two targets lying in the line with slope $\alpha = 10.0$, and $\beta = 50.0$. (a) d = 1.0 (b) d = 0.5 (c) d = 0.25 (d) d = 0.125.

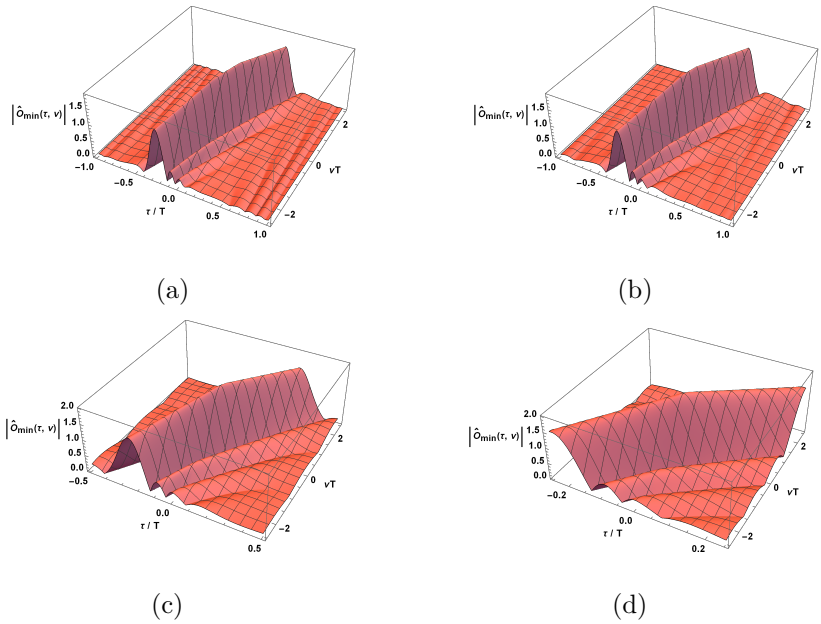

Fig. 4.16. The mismatched filter output response of two targets lying in the line with slope $\alpha = 10.0$, and $\beta = 10.0$. (a) d = 1.0 (b) d = 0.5 (c) d = 0.25 (d) d = 0.125.

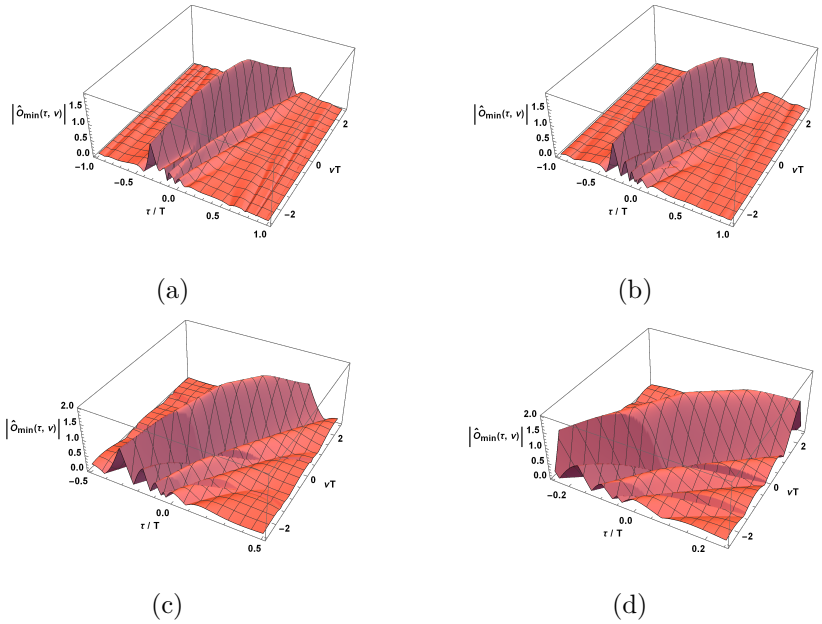

Fig. 4.17. The mismatched filter output response of two targets lying in the line with slope $\alpha = 10.0$, and $\beta = 5.0$. (a) d = 1.0 (b) d = 0.5 (c) d = 0.25 (d) d = 0.125.

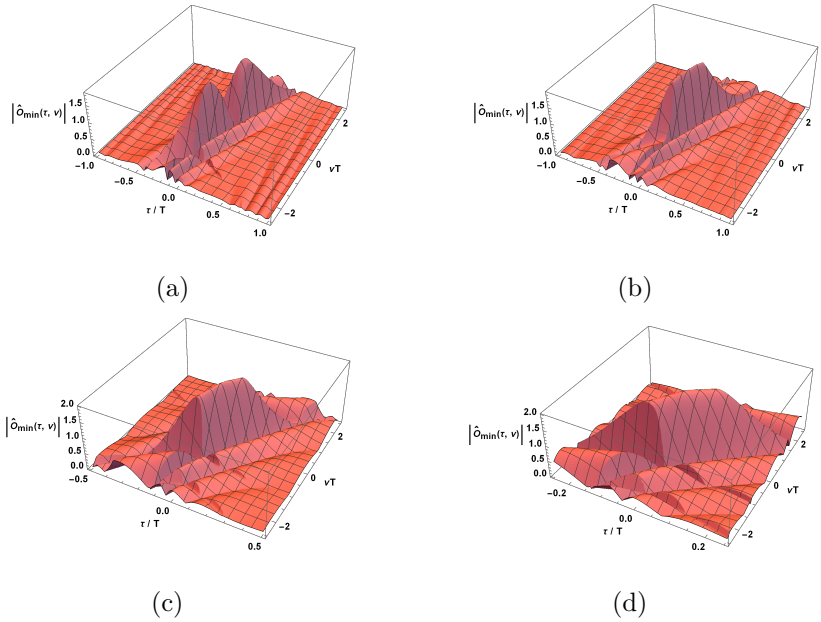

Fig. 4.18. The mismatched filter output response of two targets lying in the line with slope $\alpha = 10.0$, and $\beta = 1.0$. (a) d = 1.0 (b) d = 0.5 (c) d = 0.25 (d) d = 0.125.

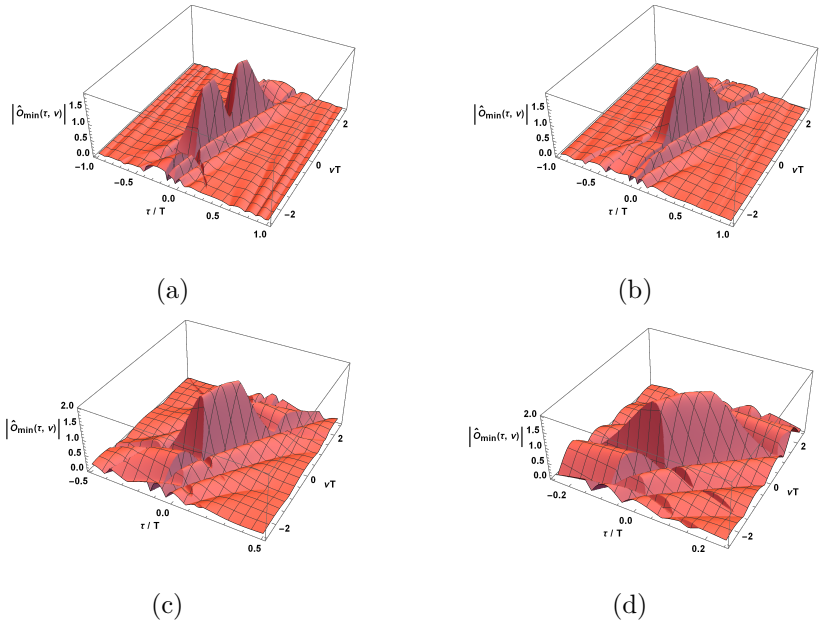

Fig. 4.19. The mismatched filter output response of two targets lying in the line with slope $\alpha = 10.0$, and $\beta = -1.0$. (a) d = 1.0 (b) d = 0.5 (c) d = 0.25 (d) d = 0.125.

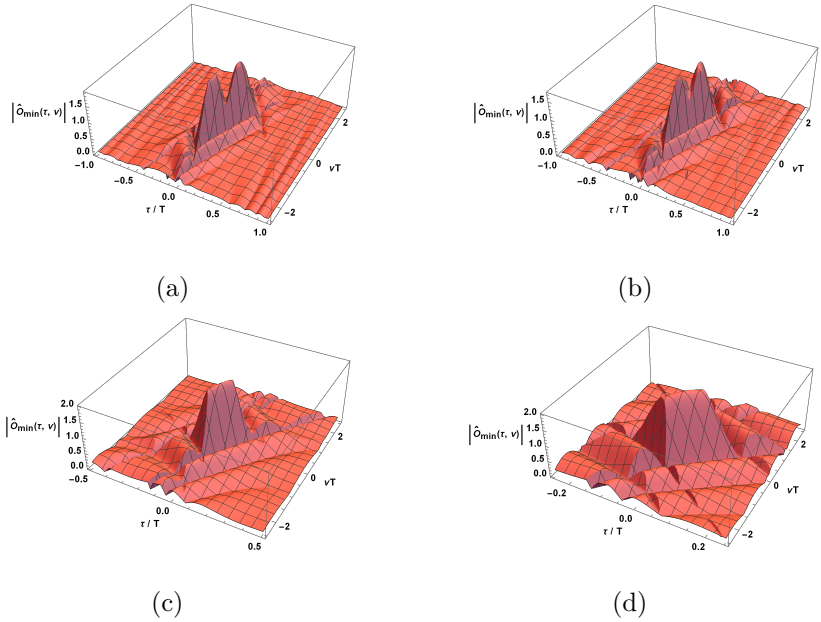

Fig. 4.20. The mismatched filter output response of two targets lying in the line with slope $\alpha = 10.0$, and $\beta = -5.0$. (a) d = 1.0 (b) d = 0.5 (c) d = 0.25 (d) d = 0.125.

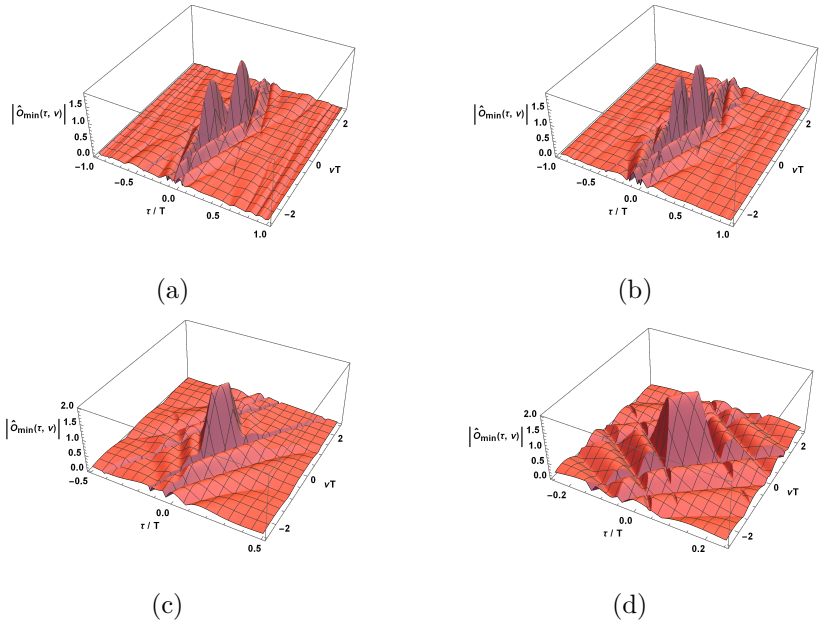

Fig. 4.21. The mismatched filter output response of two targets lying in the line with slope $\alpha = 10.0$, and $\beta = -10.0$. (a) d = 1.0 (b) d = 0.5 (c) d = 0.25 (d) d = 0.125.

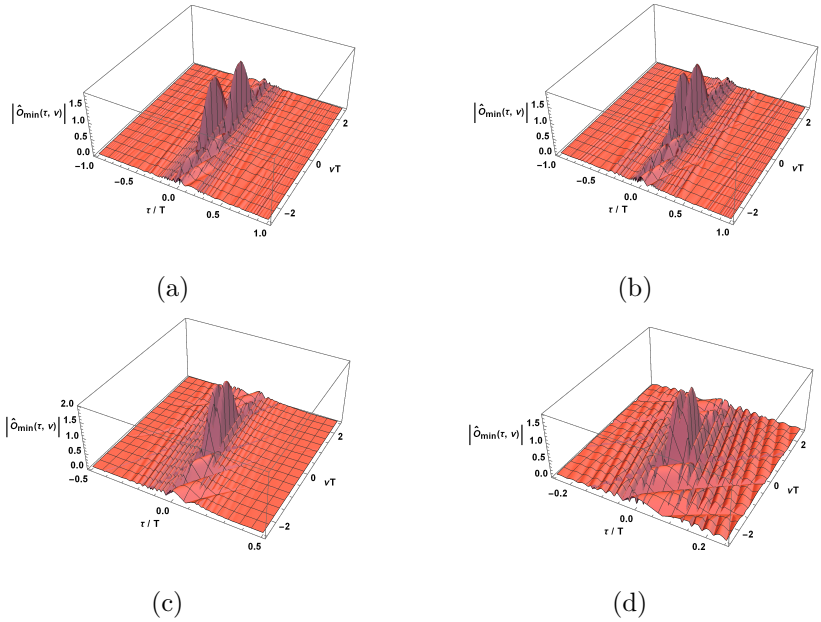

Fig. 4.22. The mismatched filter output response of two targets lying in the line with slope $\alpha = 10.0$, and $\beta = -50.0$. (a) d = 1.0 (b) d = 0.5 (c) d = 0.25 (d) d = 0.125.

process, we will divide it into two parts and analyze the signal-to-noise ratio at the two outputs in the followings.

4.5.1 SNR of x(t)

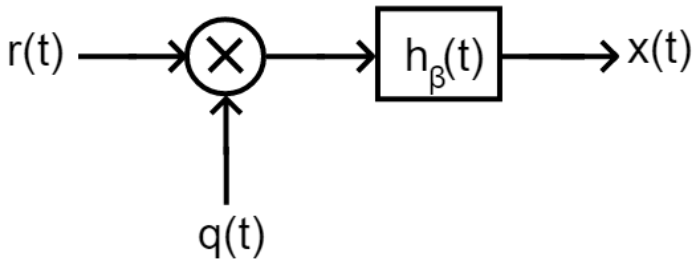

Fig. 4.23. The mismatched filter output $x(t)$.

In Figure 4.23, suppose a radar receives the signal $r(t)$ consisting of a τ_0-delayed, ν_0-Doppler shifted reflected signal $s_{\tau_0\nu_0}(t)$ and the wideband stationary additive white noise $n(t)$ [55]:

$$r(t) = s_{\tau_0\nu_0}(t) + n(t), \tag{4.27}$$

where

$$\begin{aligned} s_{\tau_0\nu_0}(t) &= s_{Tx}(t-\tau_0)e^{i2\pi\nu_0 t} \\ &= e^{i\pi\alpha(t-\tau_0)^2} \cdot 1_{[0,T]}(t-\tau_0) \cdot e^{i2\pi\nu_0 t}, \end{aligned} \tag{4.28}$$

and $n(t)$ has the autocorrelation function

$$\begin{aligned} R_{nn}(t_1,t_2) &= E[n(t_1)n^*(t_2)] \\ &= \frac{N_0}{2}\delta(t_1-t_2). \end{aligned} \tag{4.29}$$

Note that $s_{Tx}(t)$ is the transmitted chirp signal from (4.1), and

$$\begin{aligned}\int_{-\infty}^{\infty}|s_{Tx}(t)|^2dt &= \int_{-\infty}^{\infty}1_{[0,T]}(t)dt\\ &= \int_0^T 1^2dt\\ &= T\\ &= E_s. \end{aligned} \tag{4.30}$$

First of all, we pre-multiply the received signal $r(t)$ by a signal $q(t)$ to get $z(t)$

$$\begin{aligned} z(t) &= r(t)q(t)\\ &= \left(s_{\tau_0\nu_0}(t)+n(t)\right)q(t)\\ &= s_{\tau_0\nu_0}(t)q(t)+n(t)q(t)\\ &= \widetilde{s}_{\tau_0\nu_0}(t)+\widetilde{n}(t), \end{aligned} \tag{4.31}$$

where

$$q(t) = e^{i\pi(\beta-\alpha)t^2}. \tag{4.32}$$

For $\widetilde{n}(t)$, the autocorrelation function is

$$\begin{aligned} R_{\widetilde{n}\widetilde{n}}(t_1,t_2) &= E[\widetilde{n}(t_1)\widetilde{n}^*(t_2)]\\ &= E[n(t_1)q(t_1)n^*(t_2)q^*(t_2)]\\ &= E\left[n(t_1)e^{i\pi(\beta-\alpha)t_1^2}n^*(t_2)e^{-i\pi(\beta-\alpha)t_2^2}\right]\\ &= E\left[n(t_1)n^*(t_2)e^{i\pi(\beta-\alpha)(t_1^2-t_2^2)}\right]\\ &= e^{i\pi(\beta-\alpha)[(t_1+t_2)(t_1-t_2)]}E[n(t_1)n^*(t_2)]\\ &= e^{i\pi(\beta-\alpha)[(t_1+t_2)(t_1-t_2)]}R_{nn}(t_1,t_2)\\ &= e^{i\pi(\beta-\alpha)[(t_1+t_2)(t_1-t_2)]}\frac{N_0}{2}\delta(t_1-t_2)\\ &= \begin{cases}\frac{N_0}{2} & \text{if } t_1=t_2,\\ 0 & \text{otherwise}\end{cases}\\ &= R_{nn}(t_1,t_2). \end{aligned} \tag{4.33}$$

The result shows that for the wideband stationary additive white noise $n(t)$, multiplying by $q(t)$ will not change the autocorrelation function of the noise.

Now, a matching template $g(t) = e^{i\pi\beta t^2} \cdot 1_{[0,T]}(t)$, $\beta \neq \alpha$ is applied in the mismatched filter, and a τ-delayed, ν-Doppler shifted version of the template signal is $g_{\tau\nu}(t)$. Furthermore, to make sure the filter can operate on all of the relevant signal information, we sample the filter output at time $t = T + \tau$, and then $\tilde{h}_{\tau\nu,\beta}(t)$ is

$$\begin{aligned}\tilde{h}_{\tau\nu,\beta}(t) &= g^*_{\tau\nu}(T+\tau-t) \\ &= g^*(T+\tau-t-\tau)e^{-i2\pi\nu(T+\tau-t)} \\ &= e^{-i\pi\beta(T-t)^2} \cdot 1_{[0,T]}(T-t) \cdot e^{-i2\pi\nu(T+\tau-t)}. \end{aligned} \tag{4.34}$$

In the following derivations we replace $\tilde{h}_{\tau\nu,\beta}(t)$ to be $h_\beta(t)$ for brevity. Let $x_s(t)$ and $x_n(t)$ represent the signal and noise components of $x(t)$ after passing through the filter $h_\beta(t)$:

$$\begin{aligned} x(t) &= z(t) * h_\beta(t) \\ &= \int_{-\infty}^{\infty} h_\beta(l) z(t-l) dl \\ &= \int_{-\infty}^{\infty} h_\beta(l) \left[\widetilde{s}_{\tau_0\nu_0}(t-l) + \widetilde{n}(t-l)\right] dl \\ &= \int_{-\infty}^{\infty} h_\beta(l) \widetilde{s}_{\tau_0\nu_0}(t-l) dl + \int_{-\infty}^{\infty} h_\beta(l) \widetilde{n}(t-l) dl \\ &= x_s(t) + x_n(t), \end{aligned} \tag{4.35}$$

where $x_n(t)$ has the autocorrelation function $R_{x_n x_n}(t_1, t_2)$:

$$\begin{aligned} &R_{x_n x_n}(t_1,t_2) = E[x_n(t_1) x_n^*(t_2)] \\ &= E\left[\int_{-\infty}^{\infty} h_\beta(l_1)\widetilde{n}(t_1-l_1)dl_1 \cdot \int_{-\infty}^{\infty} h^*_\beta(l_2)\widetilde{n}^*(t_2-l_2)dl_2\right] \\ &= E\left[\int_{-\infty}^{\infty}\int_{-\infty}^{\infty} h_\beta(l_1)\widetilde{n}(t_1-l_1) \cdot h^*_\beta(l_2)\widetilde{n}^*(t_2-l_2)dl_1 dl_2\right] \\ &= \int_{-\infty}^{\infty}\int_{-\infty}^{\infty} h_\beta(l_1) h^*_\beta(l_2) E\left[\widetilde{n}(t_1-l_1)\widetilde{n}^*(t_2-l_2)\right] dl_1 dl_2 \\ &= \int_{-\infty}^{\infty}\int_{-\infty}^{\infty} h_\beta(l_1) h^*_\beta(l_2) \frac{N_0}{2} \delta(t_1 - t_2 - (l_1 - l_2)) dl_1 dl_2. \end{aligned} \tag{4.36}$$

As for the output signal $x_s(t)$,

$$\begin{aligned}
x_s(t) &= \int_{-\infty}^{\infty} h_\beta(l)\widetilde{s}_{\tau_0\nu_0}(t-l)dl \\
&= \int_{-\infty}^{\infty} h_\beta(t-l)\widetilde{s}_{\tau_0\nu_0}(l)dl \\
&= \int_{-\infty}^{\infty} h_\beta(t-l)s_{\tau_0\nu_0}(l)q(l)dl \\
&= \int_{-\infty}^{\infty} e^{-i\pi\beta(T-(t-l))^2}1_{[0,T]}(T-(t-l))e^{-i2\pi\nu(T+\tau-(t-l))} \\
&\cdot e^{i\pi\alpha(l-\tau_0)^2}1_{[0,T]}(l-\tau_0)e^{i2\pi\nu_0 l}\cdot e^{i\pi(\beta-\alpha)l^2}dl. \qquad (4.37)
\end{aligned}$$

The signal-to-noise ratio of $x(t)$ at time t is defined as

$$\mathrm{SNR}_t \equiv \frac{|x_s(t)|^2}{E\left[|x_n(t)|^2\right]}. \qquad (4.38)$$

Now, when the delay and Doppler shift are perfectly matched, and the perfect sampling time for observing the entire signal component is achieved, the maximum signal-to-noise ratio can be achieved, i.e., when $(\tau,\nu)=(\tau_0,\nu_0+(\beta-\alpha)\tau_0)$ and $t=T+\tau_0$,

$$\mathrm{maxSNR}_t = \mathrm{SNR}_{T+\tau_0}. \qquad (4.39)$$

In this case, we have

$$\begin{aligned}
x_s(T+\tau_0) =& \int_{-\infty}^{\infty} e^{-i\pi\beta(T-(T+\tau_0-l))^2}\cdot 1_{[0,T]}(T-(T+\tau_0-l)) \\
&\cdot e^{-i2\pi(\nu_0+(\beta-\alpha)\tau_0)(T+\tau_0-(T+\tau_0-l))}e^{i\pi\alpha(l-\tau_0)^2}\cdot 1_{[0,T]}(l-\tau_0)\cdot e^{i2\pi\nu_0 l}e^{i\pi(\beta-\alpha)l^2}dl \\
=& \int_{-\infty}^{\infty} e^{-i\pi\beta(l-\tau_0)^2}\cdot 1_{[0,T]}(l-\tau_0)e^{-i2\pi(\nu_0+(\beta-\alpha)\tau_0)l} \\
&\cdot e^{i\pi\alpha(l-\tau_0)^2}\cdot 1_{[0,T]}(l-\tau_0)e^{i2\pi\nu_0 l}e^{i\pi(\beta-\alpha)l^2}dl \\
=& \int_{-\infty}^{\infty} e^{-i\pi\beta(-2\tau_0 l+\tau_0^2)}e^{-i2\pi(\beta-\alpha)\tau_0 l}e^{i\pi\alpha(-2\tau_0 l+\tau_0^2)}\cdot 1_{[0,T]}(l-\tau_0)dl \\
=& e^{-i\pi(\beta-\alpha)\tau_0^2}\int_{-\infty}^{\infty} 1_{[0,T]}(l-\tau_0)dl \\
=& e^{-i\pi(\beta-\alpha)\tau_0^2}\int_{\tau_0}^{\tau_0+T} 1dl \\
=& Te^{-i\pi(\beta-\alpha)\tau_0^2}. \qquad (4.40)
\end{aligned}$$

Then

$$\begin{aligned} |x_s(T+\tau_0)|^2 &= \left| T e^{-i\pi(\beta-\alpha)\tau_0^2} \right|^2 \\ &= T^2 \\ &= E_s^2. \end{aligned} \tag{4.41}$$

Also, from (4.36), let $t_1 = t_2 = T + \tau_0$, then

$$\begin{aligned} E\left[|x_n(T+\tau_0)|^2\right] =& E[x_n(T+\tau_0)x_n^*(T+\tau_0)] \\ =& \int_{-\infty}^{\infty}\int_{-\infty}^{\infty} h_\beta(l_1)h_\beta^*(l_2)\frac{N_0}{2}\delta(T+\tau_0-(T+\tau_0)-(l_1-l_2))dl_1dl_2 \\ =& \int_{-\infty}^{\infty}\int_{-\infty}^{\infty} h_\beta(l_1)h_\beta^*(l_2)\frac{N_0}{2}\delta(l_2-l_1)dl_1dl_2 \\ =& \frac{N_0}{2}\int_{-\infty}^{\infty} h_\beta(l_1)h_\beta^*(l_1)dl_1 \\ =& \frac{N_0}{2}\int_{-\infty}^{\infty} e^{-i\pi\beta(T-l_1)^2}1_{[0,T]}(T-l_1)e^{-i2\pi\nu(T+\tau-l_1)} \\ & \cdot\left(e^{-i\pi\beta(T-l_1)^2}1_{[0,T]}(T-l_1)e^{-i2\pi\nu(T+\tau-l_1)}\right)^* dl_1 \\ =& \frac{N_0}{2}\int_{-\infty}^{\infty} 1_{[0,T]}(T-l_1)dl_1 \\ =& \frac{N_0}{2}[(l_1+T)-l_1] \\ =& \frac{N_0}{2}T \\ =& \frac{N_0}{2}E_s. \end{aligned} \tag{4.42}$$

Therefore,

$$\begin{aligned} \text{maxSNR}_t &= \text{SNR}_{T+\tau_0} \\ &= \frac{|x_s(T+\tau_0)|^2}{E\left[|x_n(T+\tau_0)|^2\right]} \\ &= \frac{E_s^2}{\frac{N_0}{2}E_s} \\ &= \frac{2E_s}{N_0}. \end{aligned} \tag{4.43}$$

The result shows that the mismatched filter has the same maximum signal-to-noise ratio as the maximum signal-to-noise ratio of the matched filter, $2E_s/N_0$.

4.5.2 Noise Analysis of the Sum of τ_k-shifted Responses from the Mismatched Filter Output

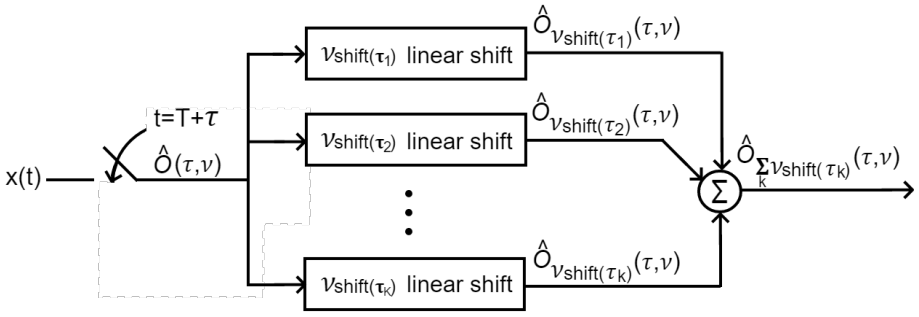

Fig. 4.24. Structure of operations of shifted mismatched filter output responses.

In Figure 4.24, to recover all delays and Doppler shifts of the mismatched output response, $\hat{O}(\tau,\nu)$ will pass through an array of linear-shift-in-Doppler processors. Each of the linear-shift-in-Doppler processors linearly shifts the whole delay-Doppler output $\hat{O}(\tau,\nu)$ to match each target's true Doppler position with respect to its delay τ_k:

$$\begin{aligned}\hat{O}_{\nu_{\text{shift}}(\tau_k)}(\tau,\nu) &= \hat{O}(\tau,\nu+(\beta-\alpha)\tau_k)\\ &= \hat{O}_s(\tau,\nu+(\beta-\alpha)\tau_k)+\hat{O}_n(\tau,\nu+(\beta-\alpha)\tau_k),\ \forall k. \end{aligned} \tag{4.44}$$

Then we combine all of the Doppler-corrected output responses (signal and noise) to keep all targets lying in the correct delay-Doppler positions. Therefore, for any (τ,ν), we have

$$\begin{aligned}\hat{O}_{\sum_k \nu_{\text{shift}}(\tau_k)}(\tau,\nu) &= \sum_k \hat{O}_{\nu_{\text{shift}}(\tau_k)}(\tau,\nu)\\ &= \sum_k \hat{O}(\tau,\nu+(\beta-\alpha)\tau_k)\\ &= \sum_k \left[\hat{O}_s(\tau,\nu+(\beta-\alpha)\tau_k)+\hat{O}_n(\tau,\nu+(\beta-\alpha)\tau_k)\right]\\ &= \sum_k \hat{O}_s(\tau,\nu+(\beta-\alpha)\tau_k)+\sum_k \hat{O}_n(\tau,\nu+(\beta-\alpha)\tau_k),\ \forall k. \end{aligned} \tag{4.45}$$

We now focus on the case where all targets lying in the same line of slope α, and $-\infty < \alpha < \infty$. In this case, any two targets do not have the same delay, so the equation (4.45) becomes

$$\hat{O}_{\sum_k \nu_{\text{shift}}(\tau_k)}(\tau,\nu) = \hat{O}_s(\tau,\nu+(\beta-\alpha)\tau) + \sum_k \hat{O}_n(\tau,\nu+(\beta-\alpha)\tau_k),\ \forall k. \tag{4.46}$$

In the following, for any specific k, we will demonstrate how to get $\hat{O}_n(\tau,\nu+(\beta-\alpha)\tau_k)$ from $x_n(t)$, and then we will analyze the SNR of $\hat{O}_{\sum_k \nu_{\text{shift}}(\tau_k)}(\tau,\nu)$. From (4.35), we know that

$$\begin{aligned}
&x_n(t) = \widetilde{n}(t) * h_\beta(t) \\
&= \int_{-\infty}^{\infty} h_\beta(m)\widetilde{n}(t-m)dm \\
&= \int_{-\infty}^{\infty} h_\beta(m)n(t-m)q(t-m)dm \\
&= \int_{-\infty}^{\infty} e^{-i\pi\beta(T-m)^2}\cdot 1_{[0,T]}(T-m)e^{-i2\pi\nu(T+\tau-m)}\cdot n(t-m)e^{i\pi(\beta-\alpha)(t-m)^2}dm,
\end{aligned} \tag{4.47}$$

and we sample at $t = T+\tau$, then

$$\begin{aligned}
&x_n(T+\tau) \\
&= \int_{-\infty}^{\infty} e^{-i\pi\beta(T-m)^2}\cdot 1_{[0,T]}(T-m)\cdot e^{-i2\pi\nu(T+\tau-m)}\cdot n(T+\tau-m)e^{i\pi(\beta-\alpha)(T+\tau-m)^2}dm \\
&= \int_{-\infty}^{\infty} e^{-i\pi\beta(T-m)^2}e^{-i2\pi\nu(T+\tau-m)}\cdot e^{i\pi(\beta-\alpha)[(T-m)^2+2\tau(T-m)+\tau^2]}n(T+\tau-m)1_{[0,T]}(T-m)dm \\
&= \int_{-\infty}^{\infty} e^{-i\pi\alpha(T-m)^2}e^{-i2\pi\nu[(T-m)+\tau]}e^{-i\pi(\alpha-\beta)[2\tau(T-m)+\tau^2]}\cdot n(T+\tau-m)\cdot 1_{[0,T]}(T-m)dm \\
&= \int_{-\infty}^{\infty} e^{-i\pi\alpha(T-m)^2}e^{-i2\pi[\nu+(\alpha-\beta)\tau](T-m)}e^{-i\pi\tau[2\nu+(\alpha-\beta)\tau]}\cdot n(T+\tau-m)\cdot 1_{[0,T]}(T-m)dm \\
&(\text{Let } l = T+\tau-m, \text{ then } dl = -dm) \\
&= \int_{-\infty}^{\infty} e^{-i\pi\alpha(l-\tau)^2}e^{-i2\pi[\nu+(\alpha-\beta)\tau](l-\tau)}\cdot e^{-i\pi\tau[2\nu+(\alpha-\beta)\tau]}\cdot n(l)\cdot 1_{[0,T]}(l-\tau)dl.
\end{aligned} \tag{4.48}$$

Now, for any $\hat{k}$, the portion of the noise at $\hat{O}_{\sum_k \nu_{\text{shift}}(\tau_k)}(\tau,\nu)$, which is contributed by the $\nu(\tau_{\hat{k}})$-shifted delay-Doppler response, is $\hat{O}_n(\tau,\nu+(\beta-\alpha)\tau_{\hat{k}})$. Therefore, we have

$$\begin{aligned}
&\hat{O}_n(\tau,\nu+(\beta-\alpha)\tau_{\hat{k}}) \\
&= \int_{-\infty}^{\infty} e^{-i\pi\alpha(l-\tau)^2} e^{-i2\pi[(\nu+(\beta-\alpha)\tau_{\hat{k}})+(\alpha-\beta)\tau](l-\tau)} \cdot e^{-i\pi\tau[2(\nu+(\beta-\alpha)\tau_{\hat{k}})+(\alpha-\beta)\tau]} \cdot n(l) \cdot 1_{[0,T]}(l-\tau) dl \\
&= \int_{-\infty}^{\infty} e^{-i\pi\alpha(l-\tau)^2} e^{-i2\pi[\nu+(\alpha-\beta)(\tau-\tau_{\hat{k}})](l-\tau)} \cdot e^{-i\pi\tau[2\nu+(\alpha-\beta)(\tau-2\tau_{\hat{k}})]} \cdot n(l) \cdot 1_{[0,T]}(l-\tau) dl \\
&= e^{-i\pi\tau[2\nu+(\alpha-\beta)(\tau-2\tau_{\hat{k}})]} \cdot \int_{-\infty}^{\infty} e^{-i\pi\alpha(l-\tau)^2} 1_{[0,T]}(l-\tau) n(l) e^{-i2\pi[\nu+(\alpha-\beta)(\tau-\tau_{\hat{k}})](l-\tau)} dl \\
&= e^{-i\pi(\beta-\alpha)\tau^2} \cdot \chi_{s_{Tx},n}(\tau,\nu+(\alpha-\beta)(\tau-\tau_{\hat{k}})), \qquad (4.49)
\end{aligned}$$

where

$$\chi_{s_{Tx},n}(\tau,\nu) = \int_{-\infty}^{\infty} s_{Tx}^*(t-\tau) n(t) e^{-i2\pi\nu t} dt$$

is the cross ambiguity function of the transmitted signal $s_{Tx}(t)$ and noise $n(t)$. Obviously, the noise content from the $\nu(\tau_{\hat{k}})$-shifted delay-Doppler response, $\hat{O}_n(\tau,\nu+(\beta-\alpha)\tau_{\hat{k}})$, is the cross ambiguity function of the transmitted signal $s_{Tx}(t)$ and noise $n(t)$, sampling at the delay-Doppler position $(\tau,\nu+(\alpha-\beta)(\tau-\tau_{\hat{k}}))$ and multiplying by the phase shift $e^{-i\pi(\beta-\alpha)\tau^2}$. Therefore, from Equation (4.46) and Equation (4.49) we know that

$$\begin{aligned}
&\hat{O}_{\sum_k \nu_{\text{shift}}(\tau_k)}(\tau,\nu)|_{t=T+\tau} \\
&= \hat{O}_s(\tau,\nu+(\beta-\alpha)\tau) + \sum_k \hat{O}_n(\tau,\nu+(\beta-\alpha)\tau_k) \\
&= \hat{O}_s(\tau,\nu+(\beta-\alpha)\tau) + \sum_k e^{-i\pi(\beta-\alpha)\tau^2} \cdot \chi_{s_{Tx},n}(\tau,\nu+(\alpha-\beta)(\tau-\tau_k)) \\
&= \hat{O}_s(\tau,\nu+(\beta-\alpha)\tau) + e^{-i\pi(\beta-\alpha)\tau^2} \sum_k \chi_{s_{Tx},n}(\tau,\nu+(\alpha-\beta)(\tau-\tau_k)). \qquad (4.50)
\end{aligned}$$

The above result shows that the total noise output response is the sum of cross ambiguity functions between the transmitted signal $s_{Tx}(t)$ and noise input $n(t)$, sampling

at $(\tau, \nu+(\alpha-\beta)(\tau-\tau_k))$, and then multiply by the phase shift $e^{-i\pi(\beta-\alpha)\tau^2}$. Therefore, the output SNR is

$$\begin{aligned}
\text{maxSNR}_t &= \text{SNR}_{T+\tau} \\
&= \frac{|\hat{O}_s(\tau, \nu+(\beta-\alpha)\tau)|^2}{E\left[|\sum_k \hat{O}_n(\tau, \nu+(\beta-\alpha)\tau_k)|^2\right]} \\
&= \frac{|\hat{O}_s(\tau, \nu+(\beta-\alpha)\tau)|^2}{E\left[|e^{-i\pi(\beta-\alpha)\tau^2}\sum_k \chi_{s_{Tx},n}(\tau, \nu+(\alpha-\beta)(\tau-\tau_k))|^2\right]}. \qquad (4.51)
\end{aligned}$$

For the signal (the numerator in (4.51)), we know from (4.40) and (4.41) that the signal has energy E_s^2. As for the noise (the denominator in (4.51)), we let

$$\begin{aligned}
\hat{n}(\tau, \nu) &= \sum_k \hat{O}_n(\tau, \nu+(\beta-\alpha)\tau_k) \\
&= e^{-i\pi(\beta-\alpha)\tau^2}\sum_k \chi_{s_{Tx},n}(\tau, \nu+(\alpha-\beta)(\tau-\tau_k)).
\end{aligned}$$

Then the correlation function is

$$
\begin{aligned}
&R_{\hat{n}\hat{n}}(\tau_1,\tau_2,\nu_1,\nu_2) = E\left[\hat{n}(\tau_1,\nu_1)\hat{n}^*(\tau_2,\nu_2)\right] \\
=&E\left[\left(\sum_k \hat{O}_n(\tau_1,\nu_1+(\beta-\alpha)\tau_k)\right)\left(\sum_j \hat{O}_n(\tau_2,\nu_2+(\beta-\alpha)\tau_j)\right)^*\right] \\
=&E\left[\left(\sum_k \hat{O}_n(\tau_1,\nu_1+(\beta-\alpha)\tau_k)\right)\left(\sum_j \hat{O}_n^*(\tau_2,\nu_2+(\beta-\alpha)\tau_j)\right)\right] \\
=&E\left[\sum_k\sum_j \hat{O}_n(\tau_1,\nu_1+(\beta-\alpha)\tau_k)\hat{O}_n^*(\tau_2,\nu_2+(\beta-\alpha)\tau_j)\right] \\
=&\sum_k\sum_j E\left[\hat{O}_n(\tau_1,\nu_1+(\beta-\alpha)\tau_k)\hat{O}_n^*(\tau_2,\nu_2+(\beta-\alpha)\tau_j)\right] \\
=&\sum_k\sum_j E\left[\left(e^{-i\pi(\beta-\alpha)\tau_1^2}\chi_{s_{Tx},n}(\tau_1,\nu_1+(\alpha-\beta)(\tau_1-\tau_k))\right)\right. \\
&\left.\cdot\left(e^{i\pi(\beta-\alpha)\tau_2^2}\chi^*_{s_{Tx},n}(\tau_2,\nu_2+(\alpha-\beta)(\tau_2-\tau_j))\right)\right] \\
=&\sum_k\sum_j e^{-i\pi(\beta-\alpha)(\tau_1^2-\tau_2^2)}E\left[\chi_{s_{Tx},n}(\tau_1,\nu_1+(\alpha-\beta)(\tau_1-\tau_k))\chi^*_{s_{Tx},n}(\tau_2,\nu_2+(\alpha-\beta)(\tau_2-\tau_j))\right] \\
=&\sum_k\sum_j e^{-i\pi(\beta-\alpha)(\tau_1^2-\tau_2^2)}E\left[\left(\int_{-\infty}^{\infty} s^*_{Tx}(t_1-\tau_1)n(t_1)e^{-i2\pi[\nu_1+(\alpha-\beta)(\tau_1-\tau_k)]t_1}dt_1\right)\right. \\
&\left.\cdot\left(\int_{-\infty}^{\infty} s_{Tx}(t_2-\tau_2)n^*(t_2)e^{i2\pi[\nu_2+(\alpha-\beta)(\tau_2-\tau_j)]t_2}dt_2\right)\right] \\
=&\sum_k\sum_j e^{-i\pi(\beta-\alpha)(\tau_1^2-\tau_2^2)}\int_{-\infty}^{\infty}\int_{-\infty}^{\infty} s^*_{Tx}(t_1-\tau_1)s_{Tx}(t_2-\tau_2)\cdot E[n(t_1)n^*(t_2)] \\
&\cdot e^{-i2\pi\{(\nu_1t_1-\nu_2t_2)+(\alpha-\beta)[(\tau_1-\tau_k)t_1-(\tau_2-\tau_j)t_2]\}}dt_1dt_2 \\
=&\sum_k\sum_j e^{-i\pi(\beta-\alpha)(\tau_1^2-\tau_2^2)}\int_{-\infty}^{\infty}\int_{-\infty}^{\infty} s^*_{Tx}(t_1-\tau_1)s_{Tx}(t_2-\tau_2)\cdot\frac{N_0}{2}\delta(t_1-t_2) \\
&\cdot e^{-i2\pi\{(\nu_1t_1-\nu_2t_2)+(\alpha-\beta)[(\tau_1-\tau_k)t_1-(\tau_2-\tau_j)t_2]\}}dt_1dt_2 \\
&(\text{let } t_1=t_2=t) \\
=&e^{-i\pi(\beta-\alpha)(\tau_1^2-\tau_2^2)}\sum_k\sum_j\int_{-\infty}^{\infty} s^*_{Tx}(t-\tau_1)s_{Tx}(t-\tau_2)\frac{N_0}{2}e^{-i2\pi\{(\nu_1-\nu_2)t+(\alpha-\beta)[\tau_1-\tau_2-(\tau_k-\tau_j)t]\}}dt \\
&(\text{let } x=t-\tau_2, \text{ then } t=x+\tau_2, \text{ and } dx=dt) \\
=&e^{-i\pi(\beta-\alpha)(\tau_1^2-\tau_2^2)}\sum_k\sum_j\int_{-\infty}^{\infty} s_{Tx}(x)s^*_{Tx}(x-(\tau_1-\tau_2))\frac{N_0}{2}e^{-i2\pi\{(\nu_1-\nu_2)+(\alpha-\beta)[\tau_1-\tau_2-(\tau_k-\tau_j)]\}(x+\tau_2)}dx
\end{aligned}
$$

$$
\begin{aligned}
=&\frac{N_0}{2}e^{-i\pi(\beta-\alpha)(\tau_1^2-\tau_2^2)}\sum_k\sum_j e^{-i2\pi\{(\nu_1-\nu_2)+(\alpha-\beta)[\tau_1-\tau_2-(\tau_k-\tau_j)]\}\tau_2}\\
&\cdot\int_{-\infty}^{\infty}s_{Tx}(x)s_{Tx}^*(x-(\tau_1-\tau_2))e^{-i2\pi\{(\nu_1-\nu_2)+(\alpha-\beta)[\tau_1-\tau_2-(\tau_k-\tau_j)]\}x}dx\\
=&\frac{N_0}{2}e^{-i\pi(\beta-\alpha)(\tau_1^2-\tau_2^2)}\sum_k\sum_j e^{-i2\pi\{(\nu_1-\nu_2)+(\alpha-\beta)[\tau_1-\tau_2-(\tau_k-\tau_j)]\}\tau_2}\\
&\cdot\chi_s(\tau_1-\tau_2,(\nu_1-\nu_2)+(\alpha-\beta)[\tau_1-\tau_2-(\tau_k-\tau_j)]),
\end{aligned}
\tag{4.52}
$$

where

$$
\chi_s(\tau,\nu)=\int_{-\infty}^{\infty}s_{Tx}(t)s_{Tx}^*(t-\tau)e^{-i2\pi\nu t}dt.
$$

Also, we can further divide Equation (4.52) into the auto terms and the cross terms as follows

$$
\begin{aligned}
&R_{\hat{n}\hat{n}}(\tau_1,\tau_2,\nu_1,\nu_2)\\
&=\frac{N_0}{2}e^{-i\pi(\beta-\alpha)(\tau_1^2-\tau_2^2)}\left\{\sum_k e^{-i2\pi[(\nu_1-\nu_2)+(\alpha-\beta)(\tau_1-\tau_2)]\tau_2}\chi_s(\tau_1-\tau_2,(\nu_1-\nu_2)+(\alpha-\beta)(\tau_1-\tau_2))\right.\\
&\left.+\sum_k\sum_{j,j\neq k}e^{-i2\pi\{(\nu_1-\nu_2)+(\alpha-\beta)[\tau_1-\tau_2-(\tau_k-\tau_j)]\}\tau_2}\chi_s(\tau_1-\tau_2,(\nu_1-\nu_2)+(\alpha-\beta)[\tau_1-\tau_2-(\tau_k-\tau_j)])\right\}.
\end{aligned}
\tag{4.53}
$$

From (4.53) we know that the correlation of $\hat{n}(\tau,\nu)$ is the coherent sum of the K phase-shifted ambiguity functions, sampling at $(\tau_1-\tau_2,(\nu_1-\nu_2)+(\alpha-\beta)(\tau_1-\tau_2))$, combined with the non-coherent sum of the $K(K-1)$ phase-shifted ambiguity functions, sampling at $(\tau_1-\tau_2,(\nu_1-\nu_2)+(\alpha-\beta)[\tau_1-\tau_2-(\tau_k-\tau_j)]), k\neq j$. Here we assume that K Doppler axes in the delay-Doppler grids are corrected. Therefore, to suppress the output noise and then to increase the SNR, we need to control α and β such that $|\chi_s(\tau_1-\tau_2,(\nu_1-\nu_2)+(\alpha-\beta)(\tau_1-\tau_2))|$ remains small, then the term of the coherent sum is small. The following is one of the simple constraints to make $|\chi_s(\tau_1-\tau_2,(\nu_1-\nu_2)+(\alpha-\beta)(\tau_1-\tau_2))|$ small: if we let

$$
(\nu_1-\nu_2)+(\alpha-\beta)(\tau_1-\tau_2)\neq\alpha(\tau_1-\tau_2),
$$

which is equivalent to

$$(\nu_1 - \nu_2) \neq \beta(\tau_1 - \tau_2).$$

Then $|\chi_s(\tau_1 - \tau_2, (\nu_1 - \nu_2) + (\alpha - \beta)(\tau_1 - \tau_2))|$ does not lie in the chirp ridge of the ambiguity function, and then the amplitude is small.

Now, to compute the SNR in (4.51), we let $\tau_1 = \tau_2 = \tau$ and $\nu_1 = \nu_2 = \nu$, then

$$\begin{aligned} R_{\hat{n}\hat{n}}(\tau, \tau, \nu, \nu) &= \frac{N_0}{2}\left\{\sum_k \chi_s(0,0) + \sum_k \sum_{j,j\neq k} e^{-i2\pi[(\alpha-\beta)(\tau_j-\tau_k)]\tau}\chi_s(0,(\alpha-\beta)(\tau_j-\tau_k))\right\} \\ &= \frac{N_0}{2}\left\{K\cdot\chi_s(0,0) + \sum_k \sum_{j,j\neq k} e^{-i2\pi[(\alpha-\beta)(\tau_j-\tau_k)]\tau}\chi_s(0,(\alpha-\beta)(\tau_j-\tau_k))\right\} \\ &= \frac{N_0}{2}\left\{K\cdot T + \sum_k \sum_{j,j\neq k} e^{-i2\pi[(\alpha-\beta)(\tau_j-\tau_k)]\tau}\chi_s(0,(\alpha-\beta)(\tau_j-\tau_k))\right\}. \end{aligned} \tag{4.54}$$

Now, from the symmetric property of the ambiguity function, we know

$$\begin{aligned} \chi_s(-\tau,-\nu) &= \int_{-\infty}^{\infty} s_{Tx}(t)s_{Tx}^*(t-(-\tau))e^{-i2\pi(-\nu)t}dt \\ &\qquad (\text{ Let } t+\tau = m,\ dt = dm\ ) \\ &= \int_{-\infty}^{\infty} s_{Tx}(m-\tau)s_{Tx}^*(m)e^{-i2\pi(-\nu)(m-\tau)}dm \\ &= e^{-i2\pi\tau\nu}\left[\int_{-\infty}^{\infty} s_{Tx}(m)s_{Tx}^*(m-\tau)e^{-i2\pi\nu m}dm\right]^* \\ &= e^{-i2\pi\tau\nu}\chi_s^*(\tau,\nu). \end{aligned} \tag{4.55}$$

Then (4.54) can be further simplified to

$$\begin{aligned}
R_{\hat{n}\hat{n}}(\tau,\tau,\nu,\nu) =& \frac{N_0}{2}\Bigg\{K\cdot T+\sum_k\sum_{j>k}\Big(e^{-i2\pi[(\alpha-\beta)(\tau_j-\tau_k)]\tau}\chi_s(0,(\alpha-\beta)(\tau_j-\tau_k)) \\
&+e^{-i2\pi[-(\alpha-\beta)(\tau_j-\tau_k)]\tau}\chi_s(0,-(\alpha-\beta)(\tau_j-\tau_k))\Big)\Bigg\} \\
=& \frac{N_0}{2}\Bigg\{K\cdot T+\sum_k\sum_{j>k}\Big(e^{-i2\pi[(\alpha-\beta)(\tau_j-\tau_k)]\tau}\chi_s(0,(\alpha-\beta)(\tau_j-\tau_k)) \\
&+e^{-i2\pi[-(\alpha-\beta)(\tau_j-\tau_k)]\tau}\chi_s^*(0,(\alpha-\beta)(\tau_j-\tau_k))\Big)\Bigg\} \\
=& \frac{N_0}{2}\left\{K\cdot T+2\sum_k\sum_{j>k}\mathrm{Re}\left\{e^{-i2\pi[(\alpha-\beta)(\tau_j-\tau_k)]\tau}\chi_s(0,(\alpha-\beta)(\tau_j-\tau_k))\right\}\right\}.
\end{aligned} \tag{4.56}$$

Therefore, to increase the SNR, we need to let

$$2\sum_k\sum_{j>k}\mathrm{Re}\left\{e^{-i2\pi[(\alpha-\beta)(\tau_j-\tau_k)]\tau}\chi_s(0,(\alpha-\beta)(\tau_j-\tau_k))\right\}$$

be negative and with the maximum absolute value.

4.6 Practical Implementation of the Chirp Hybrid Filter

To practically implement the chirp hybrid filter, we first apply the noise-target fringe analysis approach introduced in Chapter 3 to provide accurate target delay estimates. We apply the target delay estimates to shift the mismatched filter output responses and apply non-linear operations with the matched filter response to generate the hybrid filter output response. The detailed description is as follows:

STEP 1: follow the target parameter estimate algorithm in Section 3.6 to acquire the delay estimates of all targets.

STEP 2: shift the mismatched filter output response with respect to each estimated target delay value to get the shifted mismatched filter output responses.

STEP 3: sum of all shifted mismatched filter output responses.

STEP 4: do the non-linear operation to the matched filter output response and the sum of shifted mismatched filter output responses to generate the hybrid filter output response.

By doing so, we can improve the delay-Doppler resolution and the resolution along the chirp ridge in the chirp hybrid filter output response. The whole system flow chart is shown in Figure 4.25.

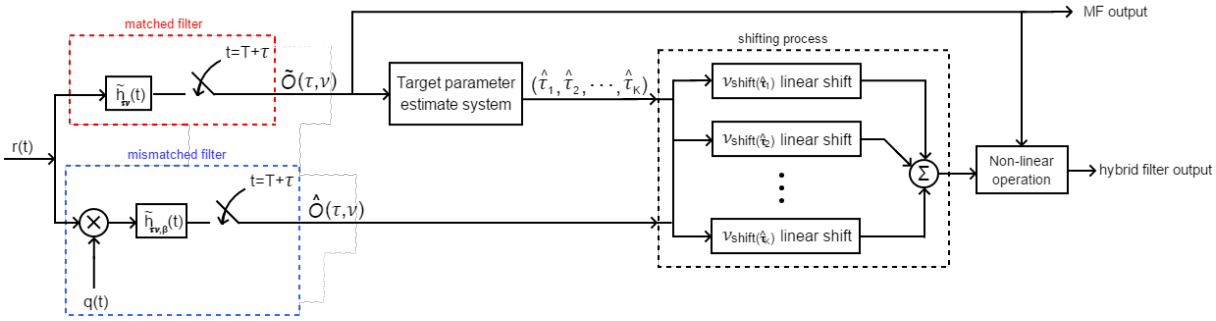

Fig. 4.25. The practical chirp hybrid filter system flow chart.

4.7 Conclusion

In this chapter, we established a chirp hybrid filter system which combines a chirp matched filter with a chirp mismatched filter to effectively improve the delay-Doppler resolutions. We also provided a thorough analyses of the mismatched filter output response, the targets' delay-Doppler positions, and the signal to noise ratio (SNR) at the output of the mismatched filter. Furthermore, we illustrated the outstanding target discrimination performance of the hybrid filter in some cases that the matched filter cannot successfully discriminate targets. Therefore, this chirp hybrid filter system can not only enhance delay-Doppler resolution but can also achieve much better performance in target discrimination.

5. SUMMARY AND CONCLUSIONS

In this thesis, our main goal is to improve the target discrimination ability in chirp radar systems. We proposed three different methods to achieve the goal. First, in Chapter 2, we designed a non-constant modulus waveform illumination at the target by synthesizing an array of constant modulus waveforms with different frequency offsets. From the resulting ambiguity function analysis, it showed better delay-Doppler sidelobe suppression performance than performance of the constant modulus waveform at the cost of slightly wider mainlobe width. In addition, we also showed that the non-constant modulus waveform can have slightly better angular resolution than the angular resolution of a constant modulus waveform but at the cost of slightly higher peak sidelobe ratio. Furthermore, we analyzed the energy density at targets in different angles and found that it is distributed more evenly in the non-constant modulus waveform case than in the constant modulus waveform case. However, due to the signal cancellations in the non-constant modulus synthesized waveform, the signal energy at targets is much smaller in the non-constant modulus waveform than in the constant modulus waveform under the consideration of same total transmitted energy.

In Chapter 3, we treated the matched filter delay-Doppler output response as an image, and we introduced the noise-target fringe analysis approach which can effectively estimate targets' delays. Moreover, we proposed an algorithm which combined the noise-target fringe analysis with the coherent CLEAN algorithm to accurately provide the radar target parameter estimates in terms of ranges, velocities, and amplitudes. To acquire more accurate parameter estimates, we applied the Gauss-Newton method and showed that estimation performance can be further improved. The target estimation algorithm effectively improves the target discrimination ability.

In Chapter 4, we established a chirp hybrid filter system to effectively improve the delay and the Doppler resolutions. We also demonstrated the outstanding performance of target discrimination of the hybrid filter in some cases that the matched filter cannot have a successful target discrimination, which showed the superior target discrimination ability of the hybrid filtering systems. Furthermore, we derived the maximum signal to noise ratio (SNR) at the mismatched filter output, which has the same magnitude as the maximum SNR at the matched filter output. Finally, we demonstrated how to apply the noise-target fringe analysis approach as the algorithm to the chirp hybrid filter for practical implementations and to achieve much better delay-Doppler resolution and target discrimination ability.

REFERENCES

REFERENCES

[1] J. R. Klauder, A. C. Price, S. Darlington, and W. J. Albersheim, "The Theory and Design of Chirp Radars," *The Bell System Technical Journal,* vol. 39, issue 4, 1960.

[2] E. N. Fowle, "The design of FM pulse-compression signals," *IEEE Transactions on Information Theory,* vol. IT-10, no. 1, Jan. 1964, pp. 61-67, 1964.

[3] J. P. Costas, "A study of a class of detection waveforms having nearly ideal range–Doppler ambiguity properties," *Proceedings of the IEEE,* vol. 72, no. 8, August 1984, pp. 996– 1009, 1984.

[4] S. W. Golomb and H. Taylor, "Constructions and properties of Costas arrays," *Proceedings of the IEEE,* vol. 72, no. 9, September 1984, pp. 1143–1163, 1984.

[5] A. Freedman and N. Levanon, "Any two N×N costas signals must have at least one common ambiguity sidelobe if N>3–a proof," *Proc. IEEE,* vol.73, pp.1530–1531, Oct.1985.

[6] S. V. Maric, I. Seskar, and E. L. Titlebaum, "On cross-ambiguity properties of welch-costas arrays," *IEEETrans. Aerosp. Electron. Syst.,* vol.30, pp.1063-1071, Oct. 1994.

[7] C.-F. Chang and M. R. Bell, "Frequency-coded waveforms for enhanced delay-Doppler resolution," *IEEE Trans. Inf. Theory,* vol.49, pp.2960-2971, Nov. 2003.

[8] C. E. Cook and M. Bernfeld, *Radar Signals: An Introduction to Theory and Application.* Academic Press, New York, 1967.

[9] A. W. Rihaczek, *Principles of High Resolution Radar.* McGraw-Hill, New York, 1969.

[10] N. Levanon and E. Mozeson, *Radar Signals.* John Wiley & Sons, 2004.

[11] J.-C. Guey and M. R. Bell, "Diversity waveform sets for delay-doppler imaging," *IEEE Trans. Inf. Theory,* vol.44, pp.1504-1522, July 1998.

[12] R. Calderbank, S. Howard, and B. Moran, "Waveform diversity in radar signal processing," *IEEE Signal Processing Magazine,* vol. 26, issue 1, Jan. 2009.

[13] M. Wicks, E. Mokole, S. D. Blunt, V. Amuso, and R. Schneible, *Principles of Waveform Diversity Design.* Raleigh, NC: SciTech Publishing, 2010.

[14] S. Pillai, K. Y. Li, I. Selesnick, and B. Himed, *Waveform Diversity: Theory Applications.* New York, NY, USA: McGraw-Hill, 2011.

[15] F. Gini, A. D. Maio, and L. K. Patton, "Waveform Design and Diversity for Advanced Radar Systems," *IET Press,* 2012, London, UK.

[16] S. D. Blunt and E. L. Mokole, "Overview of radar waveform diversity," *IEEE-Trans. Aerosp. Electron. Syst.,* vol.31, issue 11, Nov. 2016.

[17] "IEEE Standard Radar Definitions, IEEE standard 686-2008, May 2008.

[18] B. Friedlander, "On the relationship between mimo and simo radars," *IEEE Trans. Signal Process.,* vol.57, pp.394-398, Jan. 2009.

[19] J. Li and P. Stoica, "MIMO radar with colocated antennas: review of some recent work," *IEEE Signal Process. Mag.,* vol.24, pp.106-114, Sept. 2007.

[20] D. W. Bliss and K. W. Forsythe, "Multiple-input multiple-output (MIMO) radar and imaging: degrees of freedom and resolution," *in Proc. 37th IEEE Asilomar Conf. on Signals, Systems, and Computers, (Monterey,CA),* pp.54-59, Nov. 2003.

[21] Y. I. Abramovich and G. J. Frazer, "Bounds on the volume and height distributions for the MIMO radar ambiguity function," *IEEE Signal Process. Lett.,* vol.15, pp.505-508, 2005.

[22] P. Antonik, M. C. Wicks, H. D. Griffiths, and C. J. Baker, "Frequency diverse array radars," *in Proc. IEEE Radar Conf., Verona, NY, USA,* Apr. 2006, pp. 215-217.

[23] V. C. Vannicola, T. B. Hale, M. C. Wicks, and P. Antonik, "Ambiguity function analysis for the chirp diverse waveform (CDW)," *in Radar Conference, 2000. The Record of the IEEE 2000 International,* pp.666-671, 2000.

[24] S. B. Rasool and M. R. Bell, "Increasing delay-doppler resolution using chirp diversity and nonlinear processing," *IEEE Radar Conference, (Rome, Italy)*, 2008.

[25] J. Tsao and B. Steinberg, "Reduction of sidelobe and speckle artifacts in microwave imaging: the CLEAN technique," *IEEE Transactions on Antennas and Propagation*, vol. 36, 1988.

[26] A. Freedman, R. Bose, and B. Steinberg, "Techniques to improve the CLEAN deconvolution algorithm," *Franklin Institute*, vol. 332, p. 535–553, 1995.

[27] R. Bose, A. Freedman, and B. Steinberg, "Sequence CLEAN: a modified deconvolution technique for microwave images of contiguous targets," *IEEE Trans. Aerosp. Electron. Syst.*, vol. 38, p. 89–97, 2002.

[28] T. J. Cornwell, "*Hogbom's CLEAN algorithm. Impact on astronomy and beyond*". Astronomy Astrophysics, 2009.

[29] M. I. Skolnik, *Introduction to Radar Systems, 2nd ed.* McGraw-Hill, New York, 1980.

[30] M. A. Richards, *Fundamentals of Radar Signal Processing.* New York: McGraw-Hill, 2005.

[31] C. H. Wilcox, "The synthesis problem for radar ambiguity functions," *MRC Tech. Summary Rep. 157*, 1960.

[32] L.Auslander and R.Tolimieri, "Characterizing the radar ambiguity functions," *IEEE Transactions on Information Theory,* vol. 30, issue 6, Nov. 1984, pp. 832-836.

[33] L. Auslander and R. Tolimieri, "Radar ambiguity functions and group theory," *SIAMJ.Math.Anal.,* vol.16, pp.577-601, May 1985.

[34] R. M. Lemer, "Signals with uniform ambiguity functions," *IRE Nar. Conv Rec.,* pp.27-36, 1958.

[35] N. Levanon, *Radar Principles.* John Wiley & Sons, 1988.

[36] S. Haykin, *Radar Array Processing.* Springer, 1993.

[37] E. Fishler, A. Haimovich, R. Blum, D. Chizhik, L. Cimini, and R. Valenzuela, "MIMO radar: An idea whose time has come," *in Proc. IEEE Radar Conf.,* April 2004, pp. 71-78.

[38] J. B. Resnick, "High resolution waveforms suitable for a multiple target environment," Master's thesis, Massachusetts Inst. of Tech., Cambridge, MA., June 1962.

[39] J. P. Browning, D. R. Fuhrman, and M. Rangaswamy, "A Hybrid Mimo Phased-Array Concept for Arbitrary Spatial Beampattern Synthesis," *in Proc. IEEE DSP/SPE, (Marco Island, FL),* pp.446-450, Jan. 2009.

[40] W. Q. Wang, M. Dai, and Z. Zheng, "FDA Radar Ambiguity Function Characteristics Analysis and Optimization," *IEEETrans. Aerosp. Electron. Syst.,* vol.54, issue 3, June 2018.

[41] J. Högbom, "Aperture Synthesis with a Non-Regular Distribution of Interferometer Baselines," *in the Astronomy and Astrophysics Supplement,* vol. 15, p.417, 1974.

[42] P. Guillaume, *A Gauss-Newton-like optimization algorithm for "weighted " nonlinear least-squares problems.* IEEE Transactions on Signal Processing, 1996.

[43] Floudas, C. A., Pardalos, and P. (Eds.), *Encyclopedia of Optimization*, 2nd ed. Springer, 2009.

[44] L. L. Scharf, *Statistical Signal Processing: Detection, Estimation, and Time Series Analysis.* Pearson, 1991.

[45] J. Minkoff, *Signals, Noise, and Active Sensors: Radar, Sonar, Laser Radar.* Wiley, 1992.

[46] H. V. Poor, *An Introduction to Signal Detection and Estimation.* Springer, New York, NY, 1994.

[47] U. J. Schwarz, "Mathematical-statistical description of the iterative beam removing technique (method CLEAN)," *Astronomy and Astrophysics*, vol. 65, pp. 345–356, 1978.

[48] A. Segalovitz and B. R. Frieden, "A "CLEAN"-type deconvolution algorithm," *Astronomy and Astrophysics*, vol. 70, pp. 335–343, 1978.

[49] B. G. Clark, "An efficient implementation of the algorithm "CLEAN"," *Astronomy and Astrophysics*, vol. 89, no. 3, pp. 377–378, 1980.

[50] B. Hanson, K. Klink, K. Matsuura, S. M. Robeson, and C. J. Willmott, "Vector correlation: Review, exposition, and geographic application," *Ann. Assoc. Amer. Geographers*, vol. 82, no. 1, p. 103–116, 1992.

[51] P. J. Schreier, "A unifying discussion of correlation analysis for complex random vectors," *IEEE Transactions on Signal Processing*, vol. 56, pp. 1327–1336, 2008.

[52] P. J. Schreier and L. L. Scharf, *Statistical Signal Processing of Complex-Valued Data : The Theory of Improper and Noncircular Signals*. Cambridge University Press, 2010.

[53] R. A. Horn, *Matrix Analysis*. Cambridge University Press New York, NY, 2nd ed, 2013.

[54] A. Papoulis and S. Pillai, *Probability, Random Variables, and Stochastic Processes*. McGraw-Hill, Fourth Edition, 2002.

[55] M. K. Simon, *Probability Distributions Involving Gaussian Random Variables: A Handbook for Engineers, Scientists and Mathematicians*. Springer, 2002.

APPENDICES

VITA

VITA

Chia-Jung Chang received the B.S. degree in Communication Engineering from the National Central University, Taoyuan, Taiwan, in 2007 and the M.S. degree in Communication Engineering from the National Taiwan University, Taipei, Taiwan, in 2009. From 2010 to 2016 he was employed by National Chung-Shan Institute of Science and Technology, Taoyuan, Taiwan. His research interests are waveform and receiver design of radar systems, MIMO radar, detection and estimation, and performance analysis of radar systems.